A STUDY OF MICROSTRUCTURAL EVOLUTION DURING SINTERING USING TESSELLATION

by

Richard John McAfee, Jr.

BS, University of Pittsburgh, 1998

Submitted to the Graduate Faculty of

the School of Engineering in partial fulfillment

of the requirements for the degree of

Doctor of Philosophy

University of Pittsburgh

2004

UNIVERSITY OF PITTSBURGH

SCHOOL OF ENGINEERING

This dissertation was presented

by

Richard John McAfee, Jr.

It was defended on

April 6, 2004

and approved by

Anthony J. De Ardo, Professor, Materials Science and Engineering

Pradeep P. Phulé, Professor, Materials Science and Engineering

Jörg M. K. Wiezorek, Assistant Professor, Materials Science and Engineering

William S. Slaughter, Associate Professor, Mechanical Engineering

Ian Nettleship, Associate Professor, Materials Science and Engineering
Dissertation Director

A STUDY OF MICROSTRUCTURAL EVOLUTION DURING SINTERING USING TESSELLATION

Richard John McAfee, Jr., PhD

University of Pittsburgh, 2004

Understanding the correlation between microstructure, properties, and processing conditions will aid in producing new or improved products. Microstructural characteristics typically used in materials science (grain size, pore size, etc.) may not identify the complete processing, microstructure, and property relationships because the relevant characteristics of the microstructure may be observed only at a higher length scale. A meso-scale characterization of microstructure was invaluable in identifying the effect of flocculation during slip casting on the evolution of the relationships during the sintering of alumina at 1350°C. Boundary tessellation of features segments a materialographic section into regions with dimensions larger than the scale of the feature. These regions contain the feature and its immediate environment allowing the definition of microstructural parameters on a meso-scale. To develop the methods and interpretation of meso-scale parameters, alumina powder cast under two dispersion conditions, dispersed and flocculated, sintered at 1350ºC to minimize coarsening in the flocculated alumina during intermediate stage sintering, provides a materials system in which many of the variables associated with microstructure and processing are held constant for the two different 'materials' (dispersed and flocculated alumina) through a range of densities. The results of this work show that meso-scale characteristics of the microstructure obtained by boundary tessellation of pore sections were correlated with the observed higher densification rate for dispersed alumina at low densities (V_V < ~0.85) and the evolution to higher densities, while 'typical' microstructural parameters such as grain size, pore size, and surface area per unit volume did not correlate with the evolution of the densification rate. The presence of a rearrangement process at lower densities is proposed as the mechanism responsible for the differences in densification rate at relative densities below ~0.90. Although the methodology developed for this study was specific

to the sintering of alumina powder compacts formed by slip casting, the use of tessellation may be applied to other systems in which the spatial arrangement of ‘particles’ is of importance.

TABLE OF CONTENTS

LIST OF TABLES

LIST OF FIGURES

ACKNOWLEDGEMENTS

I would like to begin by thanking my advisor, Professor Ian Nettleship, for his guidance and support throughout my academic career at the University of Pittsburgh. I would also like to thank the members of my thesis committee for their technical and philosophical input at important stages of this work. The faculty, staff, and students of the Materials Science & Engineering and Mechanical Engineering Departments have also enriched my experience at the School of Engineering. Also, the pursuit of my education would have been much more difficult if were not for the encouragement and support of my family, especially my Dad. Finally, financial support from the National Science Foundation (CMS 9800430) is gratefully acknowledged.

1.0 INTRODUCTION

Components produced from powder materials can have significantly better properties than components produced using other materials processes by controlling grain growth and chemical or phase segregation during densification. The use of powder materials may also reduce production cost by producing near net shape components or components that could not otherwise be produced. Sintering is a thermally activated process by which loose inorganic powders or powder compacts are given desired properties. The densification and microstructural evolution of alumina (Al_2O_3) during sintering has been subjected to extensive investigation[1-5]. However, there are important issues that need to be resolved regarding the predictions of final properties, microstructure, and shape by densification models that restrict densification to an isotropic decrease in particle center to particle center spacing[6-9]. Results of these phenomenological models can be implemented in Finite Element simulations of the evolution of a component's shape during densification and its final properties[10-15]. The use of accurate computer modeling can significantly reduce the cost of component design over the experience based or trial and error methods of pre-densified component design. Empirically based design tools have been used to design pre-densified components for several years[16]. However, to validate these models it is necessary to have a basis of comparison.

This work is a study of the sintering of an alumina powder (Premalox, ALCOA), cast in dispersed and flocculated conditions, using a sintering temperature of 1350°C. It is known that flocculation of the particles during casting can increase coarsening at high temperatures (>1500°C) which reduces the driving force for densification[17]. Coarsening due to flocculation may be reduced at lower sintering temperatures (1340°C) [18]. By using a single powder cast under different dispersion conditions and avoiding significant coarsening through the intermediate stage of sintering, densification behavior and the characteristics of the microstructure related to

the rate of densification can be studied more directly. Results presented here demonstrate that current methods of evaluating the evolution of a microstructure (grain size, pore size, morphology, etc.) during densification may be inadequate to characterize differences in microstructure for different processing conditions such as the casting condition that may affect the properties of the material. Observations made of the microstructure of sintered alumina powders reveal the presence of clusters of particles. Tessellation of features on materialographic sections segments the microstructure in regions which include pore sections and a fraction of the solid area[19-23]. This defines a higher scale (mesoscale) at which the differences in processing conditions reveal themselves. Tessellation cell maps (two dimensional histograms) were developed to visualize the correlation between various feature or cell measurements and tessellation cell properties. The maps help to identify possible mechanisms of densification, the regimes over which they are active, and the portion of the microstructure that they are associated with. The results suggest that at least two mechanisms or processes are associated with densification. The first is referred to as contact flattening or neck growth which is characterized by the reduction in the distance between particle or grain centers. The second mechanism is a coordinated rearrangement of grains or particles (and pores). The rearrangement mechanism is only active for solid volume fractions below approximately 0.9.

2.0 BACKGROUND

Contained in this section is the necessary background information regarding the sintering of alumina and the methods of microstructural analysis used in this work.

2.1 SINTERING

2.1.1 Alumina Powder

The ceramic powder used in the sintering experiments is a high purity α-alumina, Premalox (Table 1), produced by ALCOA with a volumetric median particle size of 0.28 microns and geometric standard deviation of 1.49 (Figure 1) (measurement by sedimentation, Horiba CAPA 300). The particle size is well within a range in which agglomeration may occur due to van der Waals forces and forces of adhesion. The particle size distribution (Figure 2) is relatively narrow. Also, the as-received alumina powder has a non-spherical morphology.

Table 1: Composition of Premalox alpha-alumina powder from ALCOA. The stated median particle by volume is less than 0.20 microns with a specific surface area of 11.6 square meters per gram.

Premalox - Calcined Alumina	
Chemical Species	**Weight Percent of Total**
Al_2O_3 by Difference	99.8
Na_2O	0.06
SiO_2	0.02
Fe_2O_3	0.01
CaO	0.02
B_2O_3	0.001
MgO	0.05

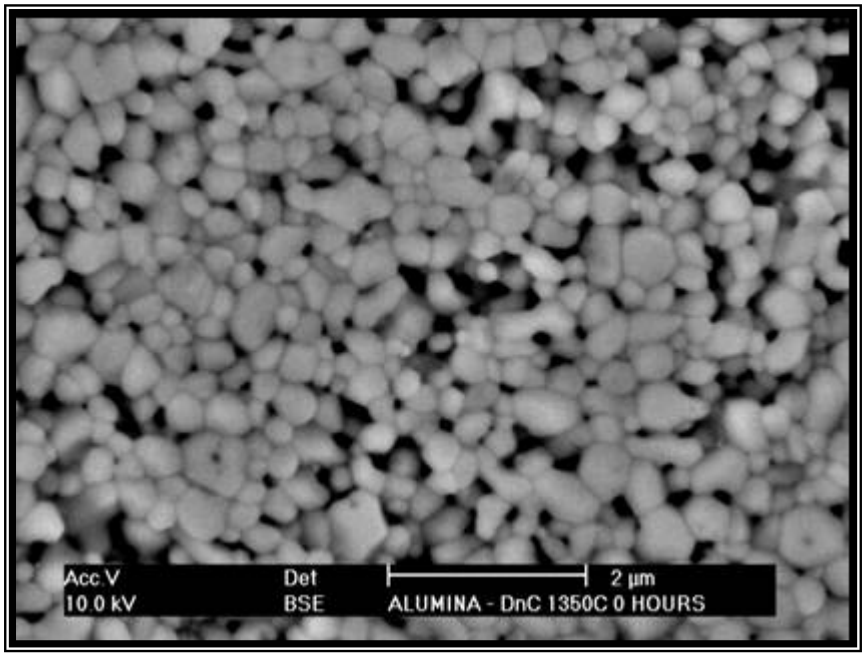

Figure 1: SEM micrograph of alumina sintered for 0.1 hours at 1350ºC. The particle size distribution has a median of 0.28 microns by volume and a lognormal standard deviation of 1.49.

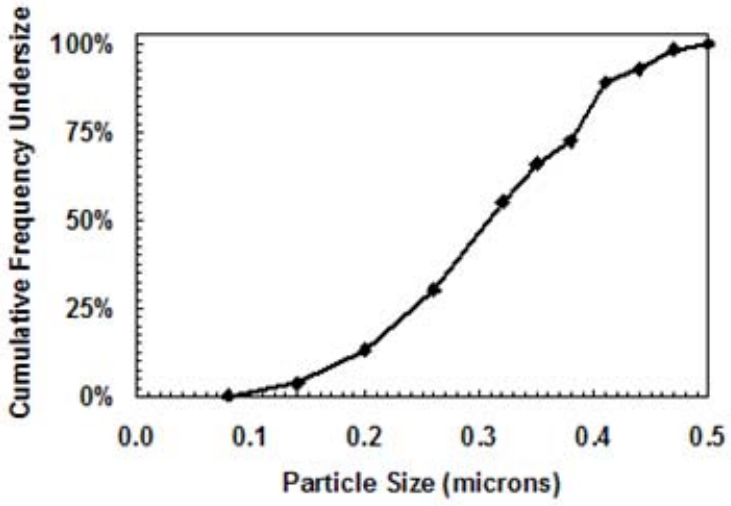

Figure 2: Particle size distribution cumulative frequency undersize by volume for dispersed alumina (Premalox) prior to casting. The powder has a relatively narrow size distribution lognormal standard deviation of 1.49.

2.1.2 Casting

The effect of particle size distribution on green density, densification kinetics, and final properties have been studied extensively[24-34]. Other terms for the green density are the initial packing ratio or solid volume fraction for a homogeneous material. It is well known that wider particle size distributions (particle sizes distributed over a wide range around the mean) generally provide a higher green density thereby reducing the total shrinkage of the final component[24,28-30]. The effect of particle size distributions has been studied through the use of tailored particle size distributions by the mixing of distributions with different modes and separation of particles from an initially larger particle size distribution. In essence, the higher green densities and packing fractions are achieved by small particles filling the interstices between large particles. If the fraction of large particles is too high not all of the interstices will be filled efficiently and if there are too few large particles the packing will be similar to that of a more narrow size distribution powder.

The green density is also controlled by the method of forming used to produce the green structure[17,35,36]. The powder compacts in this work were produced by slip casting. Slip casting is a process by which a shape is produced by casting an aqueous suspension of powder particles, a slurry, into a porous mold which is allowed to dry before firing. Ceramic particles in an aqueous suspension can have strong interactions between each other due to Van der Waals force and/or coulombic forces. These forces can be controlled by adjusting the pH of the aqueous suspension or through the use of a dispersant. The state of particles that are held together by interparticle forces is termed flocculation. In an aqueous suspension hydroxyl groups, for example may adsorb on to the surface of fine ceramic particles (in this research submicron sized alumina). The concentration of surface charge depends on the pH level of the suspension and a low surface potential may cause the particles to flocculate or aggregate forming large agglomerates. A pH level of 9 will cause the flocculation of alumina powder and a level of 4 will disperse the particles. In place of pH level adjustment to prevent flocculation a sparingly soluble polyelectrolyte dispersant may adsorb on to the particle surface to effectively shield particles from each other reducing the attractive forces between particles. Large aggregates of particles caused by flocculation will reduce the packing efficiency in castings and two distinct types of pores will be present, large pores between aggregates and small pores between particles within the aggregates[36].

2.1.3 Driving Force

The driving force for densification and coarsening during sintering is a gradient in chemical potential resulting from variations in surface curvature which results in the transport of matter by diffusional and evaporation-condensation mechanisms[1-5,37,38,39]The chemical potential decreases from the convex surfaces of particles to the concave regions between particles. This is typically illustrated by the use of a two-sphere model for the initial stage of sintering, Figure 3. Although the intermediate and final stage models use different geometries from the initial stage model, the mechanisms are the same and the driving force is the same. Instead of describing the driving force for diffusion in terms of the chemical potential, the governing equation for the difference in equilibrium concentration for a curved surface (c) relative to a flat surface (infinite curvature, c_0), the Gibbs-Thompson-Freundlich equation, Equation 1, is presented[2]

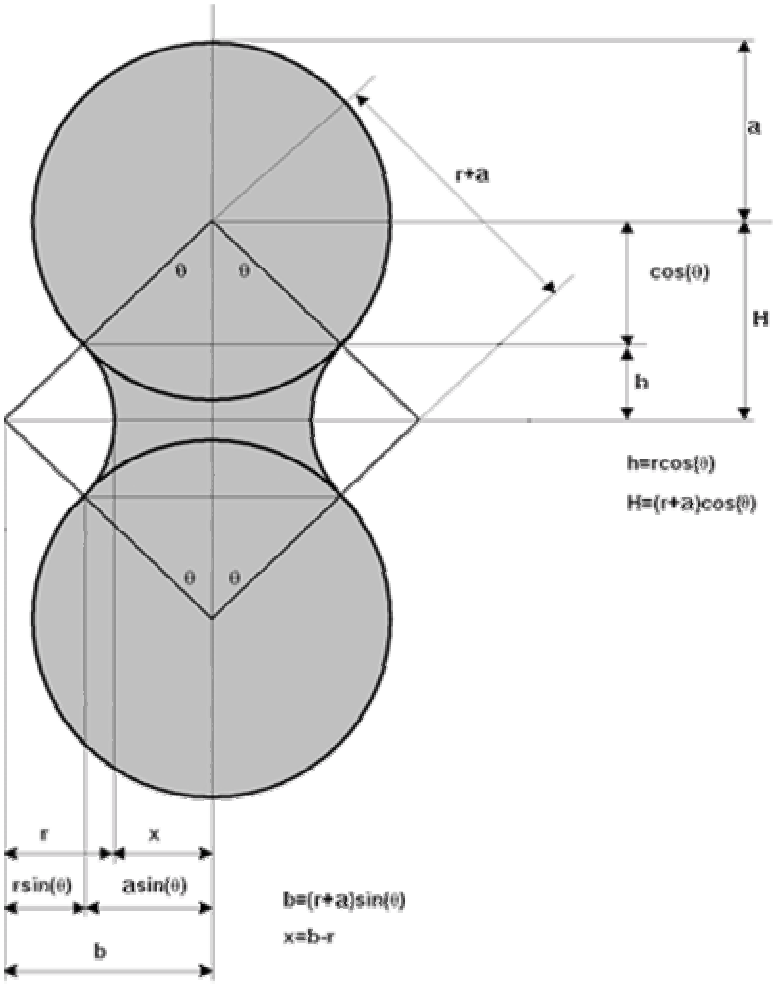

Figure 3: Illustration of the two sphere sintering model geometry. The neck radius is given by x and the particle radius is a.

$$\text{Equation 1: } c_0 - c = \frac{\gamma \bullet c_0 \bullet M}{R \bullet T}\left(\frac{1}{r_1} + \frac{1}{r_2}\right)$$

The principle radii of curvature for the curved surface are r_1 and r_2, M is the molar volume, γ is the energy per unit area of the surface, R is the gas constant, and T is the absolute temperature. The radii of curvature for a convex surface, the particle surface, will both be positive. However, in the concave neck region the radius in the plane of the contact area between the particles will be positive but the radius in the plane of the particle centers will be negative. The net difference between the vacancy concentrations will control vacancy diffusion and matter transport.

Densification, removal of matter between particles resulting in a reduction in the center to center distance between particles, may occur if the concentration of vacancies is higher in the neck region. However, coarsening and densification share a common driving force, the chemical potential or concentration gradient associated with surface curvature. The occurrence of densification and / or coarsening depends on the active diffusion mechanism or mechanisms. Volume or lattice diffusion from the contact region, and grain boundary (for particles with crystallographic misorientation) diffusion will transport atoms from between the particles but volume diffusion from the particle surface to the neck, surface diffusion and evaporation-condensation will not. If the particles are crystallographically misoriented the contact area between particles will be a grain boundary and neck growth may be halted by attaining equilibrium between the grain boundary and two particle–pore (solid-vapor) interfaces[40]

An equation describing the densification of the two sphere model as a function of time is given by Equation 2. The parameters h, one half the distance between particle centers, and a, the radius of the particle, relate the change in geometry to time, t using material parameters such as diffusion constants and surface free energies contained in the constants. Examples of the constants C, n, and m which are governed by the dominant diffusion mechanism are given in Table 2[2] Unfortunately, n and m have ranges of values that makes identification of the appropriate mechanism impossible simply by fitting the equation to experimental results. Other than viscous flow the mechanisms have overlapping ranges of values for n for each of the diffusional and evaporation-condensation mechanisms with similar overlapping ranges for m. Also, the parameters cannot account for simultaneous mechanisms.

$$\text{Equation 2: } \left(\frac{h}{a}\right)^{\frac{n}{2}} = \frac{C \bullet t}{2^n \bullet a^m}$$

Table 2: Exponents, n and m, and the constant, C, for the neck growth equation given by active transport mechanism. Determination of these parameters from experiment will be of little value due the ranges of values that may be obtained for different mechanisms. Except for viscous flow all n values range from 3 to 7 and all m values range from 2 to 4. A value of 4 for n only rules out viscous flow and a value of 3 for m only rules out viscous flow and grain boundary diffusion.

Transport Mechanism	n	m	C Parameters in addition to Specific Surface Area
Viscous Flow	2	1	Viscousity
Evaporation and Condensation	3 to 7	2 to 4	Vapor Pressure, Temperature $^{-1.5}$
Grain Boundary Diffusion	6	4	Grain boundary diffusion coefficient and thickness, Temperature $^{-1}$
Volume Diffusion: Grain Boundary to Surface	4 to 5	3	Volume diffusion coefficient, Temperature $^{-1}$
Volume Diffusion: From Surface	4	3	Volume diffusion coefficient, Temperature $^{-1}$
Surface Diffusion	3 to 7	2 to 4	Surface diffusion coefficient, Temperature $^{-1}$

In addition to the two equally sized sphere model, numerical simulations of two spheres of different sizes have been performed in an attempt to simulate the effects of a particle size distribution[41] However, the model is only successful in describing early stage sintering. Models using three or more spheres have also been developed but again the geometry is an oversimplification of the true geometry.

2.1.4 Densification

It is well known that the microstructure of the green body can have a significant effect on the densification behavior and microstructural evolution in ceramic materials. As previously stated the driving force for sintering is the reduction of free energy by reduction in the amount of surface area. The surface area per unit volume of a particle is inversely proportional to its size (diameter), smaller particles have larger amounts of surface area per unit solid volume and a greater potential for sintering. Several examples of the effect of particle size distribution on densification are found in the literature[24,25,26,42,43,44]. Some of the typical results for well dispersed or pressed powders include a higher green density for wider particle size distributions, reduced grain growth for narrower particle size distributions during the final stage of sintering, and relatively constant mean pore size through the intermediate stage of sintering. The relationship

between wider grain size distribution and higher green density does not always hold due to some inefficiency in the packing. The difference in the grain growth in the final stage is attributed to a delay in pinch off of the pore channels for narrow distributions of particle size. With a wider particle size distribution there will be regions of the microstructure where pore channels will close sooner. The driving force for grain growth, the reduction of free energy by the reduction of grain boundary area, will be higher in these regions. Although the mean pore size remains relatively constant, the distribution of pore size narrows with increasing solid volume fraction. Also, the mean pore radius for a narrow particle size distribution is larger than the mean pore radius for a wider distribution due to initial lower solid volume fractions[48-54].

Several studies have been performed to understand the effects flocculation on particle packing characteristics. Typically, flocculation of alumina powder during slip casting will decrease the green (initial) density of the compact[55-65]. Flocculation will also decrease densification kinetics and promote grain growth during sintering. Most experiments have been performed at temperatures of 1500ºC or higher. A study by Cameron and Raj[17], one of the few studies that included quantitative microstructural analysis of dispersed and flocculated alumina sintered at the same temperatures, examined the evolution of the grain size with density for dispersed and flocculated alumina at 1550ºC. It was found that during the intermediate stage of sintering ($\sim 0.8 < V_V < \sim 0.92$) there was pronounced grain growth in the flocculated alumina while grain size remained constant for dispersed alumina. Grain growth only occurs in the dispersed alumina after the porosity becomes discontinuous during final stage sintering ($V_V > \sim 0.92$). Cameron and Raj also demonstrated that the final grain size of the flocculated samples was inversely related to the green density. Higher green densities resulted in a smaller final grain size. The solid volume fraction for dispersed alumina was ~0.77 at the start of isothermal sintering while the flocculated had a solid volume fraction of ~0.68. Also, the densification rate for flocculated alumina through the intermediate stage of sintering was considerably lower than that of dispersed alumina. The flocculated alumina required approximately 80 minutes for the solid volume fraction to increase from 0.8 to 0.9 while the dispersed required less than 10 minutes. The reduced densification rate is normally attributed to a reduction in the driving force for densification due to grain growth as a result of the initial particle packing arrangement.

The study of the sintering of alumina prepared from dispersed and flocculated slips by Cameron and Raj was performed using the same temperature for dispersed and flocculated alumina. However, the pronounced grain growth during the intermediate stage does not allow the effect of flocculation to be studied in the absence of coarsening. The effect of flocculation on the microstructural evolution during sintering for alumina has also been studied by Sacks and Yeh[18]. Figure 4 and **Figure 5** show the effect of flocculation on the densification behavior of a high purity alumina powder with mean particle size of 0.87 microns and a lognormal standard deviation of 1.23 sintered at 1340ºC. Before 12 hours of time at temperature the densification rate is slightly higher in the dispersed alumina. After 12 hours the densification rate is significantly higher in the flocculated alumina.

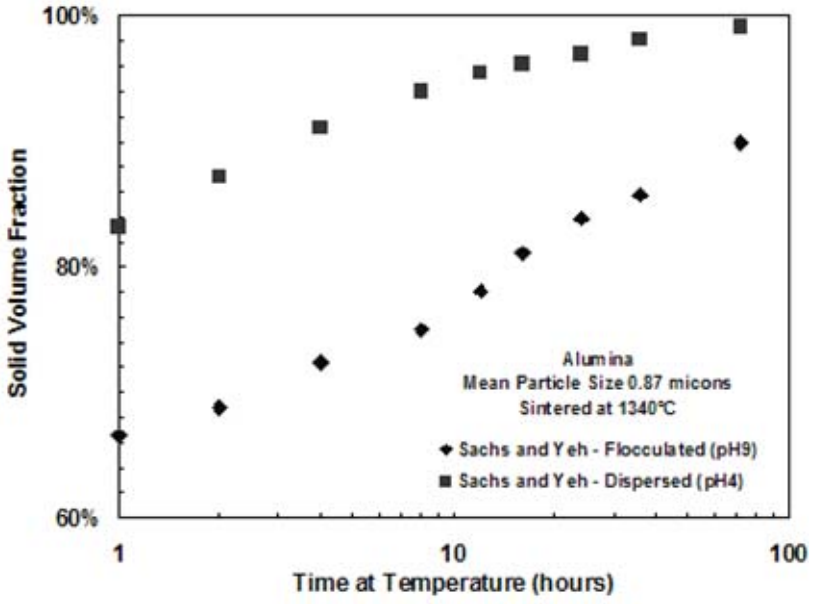

Figure 4: Densification of sintered alumina with a median particle size of 0.87 microns and a standard deviation of 1.23 [Sacks & Yeh].

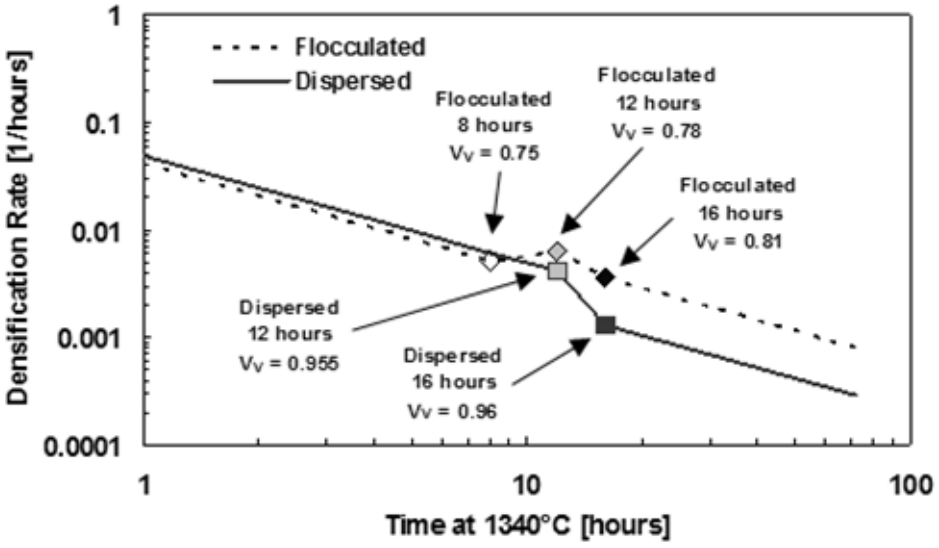

Figure 5: Densification rates for dispersed and flocculated alumina shown in Figure 4. Before 12 hours of time at temperature the densification rate is slightly higher in the dispersed alumina. After 12 hours the densification rate is significantly higher in the flocculated alumina.

Figure 6 shows the solid-vapor surface area per unit volume for the dispersed and flocculated alumina samples of Sacks & Yeh. There is a linear relationship between S_V^{SV} and V_V indicating a constant mean pore intercept length for each casting condition. The flocculated samples had a larger mean pore radius (0.4 microns) than the dispersed samples (0.2 microns) and mean pore size was constant through the range of solid volume fraction until the final stage of sintering. During final stage (V_V > ~0.9) the dispersed and flocculated alumina had similar mean pore intercept lengths. The increase in mean pore radius with flocculation is similar to the increase associated with narrowing the particle size distribution.

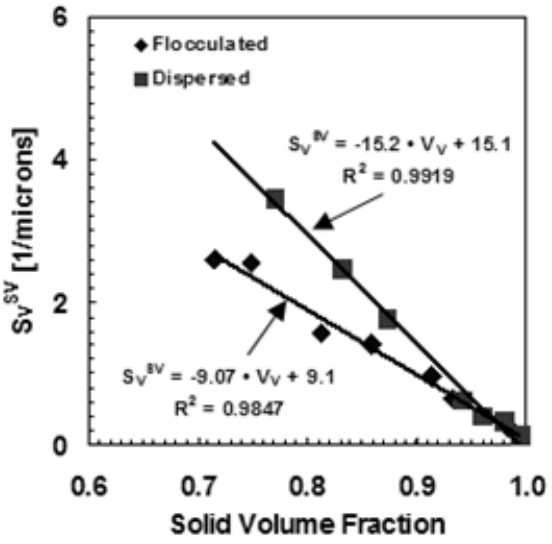

Figure 6: There is a linear relationship between S_V^{SV} and V_V for the dispersed and flocculated alumina for the same samples of Figure 4 [Sacks & Yeh]. The linear relationship indicates a constant mean pore intercept length.

The mean grain intercept length for dispersed alumina remained constant at solid volume fractions below 0.9 (**Figure 7**). There was only modest grain growth in flocculated alumina as well. However, unlike the effect of narrowing the size distribution, flocculation resulted in more grain growth in the final stage not less. This grain growth is likely due to the use of a higher sintering temperature (1450°C) to obtain densities in the same range as the dispersed alumina. Studying the effect of flocculation on densification behavior and microstructural evolution during the intermediate stage of sintering can therefore be studied in the absence of significant coarsening at sintering temperatures of approximately 1350°C for submicron alumina powder. The results of Cameron and Raj indicated that the green density also has a significant effect on grain growth. Since there was a relatively large differences in the dispersed and flocculated green densities in the work of Sacks and Yeh with only modest grain growth during the intermediate stage, a flocculated alumina with a higher green density may have even further reduced grain growth during the intermediate stage.

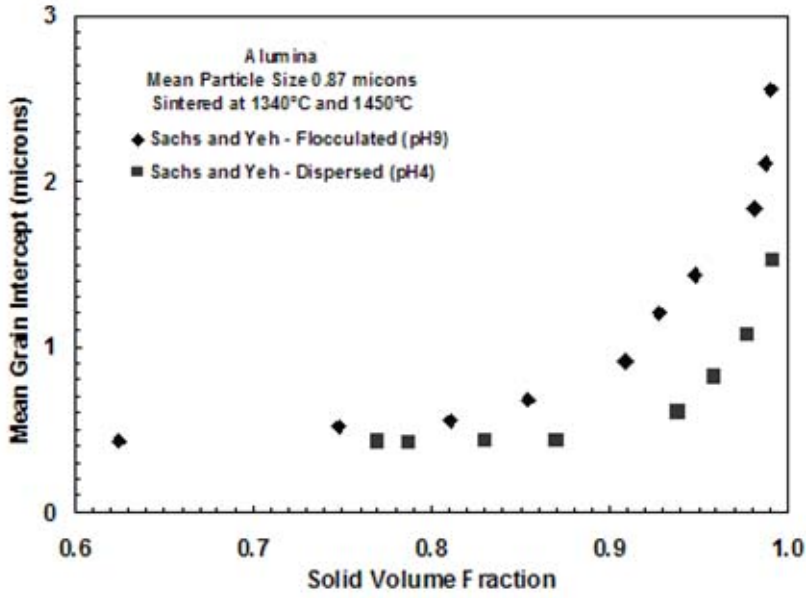

Figure 7: The evolution of the mean grain intercept for alumina sintered at 1340ºC with a median particle size of 0.87 microns and a standard deviation of 1.23 [Sacks & Yeh]. Grain growth is delayed in the dispersed samples to higher solid volume fractions.

2.1.5 Stages of Sintering

Due to the wide spread use of the sintering process there have been many books and other publications produced addressing almost all aspects of the process1-5. Sintering is a process by which loose inorganic powders or powder compacts formed by pressing are given desired properties. The sintering of ceramic materials has been practiced for millennia without fully understanding the process. The goal of this research is to develop a method of characterizing the microstructure of materials during densification to provide a better understanding of the effect of processing variables on the final microstructure and its evolution. Classically, in order to better understand the process it is divided in three stages, the initial, intermediate, and final stages[7,8,9]. The initial stage is characterized by the formation and growth of necks between particles without significant densification. Densification is defined as the isotropic center to center approach of particle centers. The formation of necks without densification is referred to as coarsening[66,67,68,69]. Typically, the majority of densification takes place during the intermediate stage of sintering. During this stage the pore structure is comprised of a network of interconnected channels throughout the material. As densification progresses the pore channels

pinch-off, the porosity becomes closed or discontinuous, this is the beginning of the final stage. Continued densification takes place in the final stage by the shrinkage of closed pores. The transition from the intermediate stage to the final stage typically takes place at a relative density or solid volume fraction of approximately 0.90.

2.1.6 Sintering Models

Microstructural evolution during sintering has been modeled for decades using simple geometries. The early phenomenological models for the intermediate stage of sintering include a simple cubic arrangement of equisized spheres and a body centered cubic arrangement of Kelvin tetrakaidecahedra (truncated octahedra) with cylindrical pore channels located on the 36 edges. The final stage has also been modeled using the body centered cubic arrangement of tetrakaidecahedra except that the pores are represented by spheres located on all 24 corners. Densification rates for these models are determined by assuming an active diffusion mechanism. The tetrakaidecahedron is chosen because it is topologically similar to observed microstructural averages of three grains per edge and four grains per corner[8,9]. Densification in these models is simulated by decreasing the distance between particle centers and maintaining flat contacts between particles. The ranges over which these models are valid depends on maintaining the geometry of the model. The maximum and minimum solid volume fractions are determined by the point at which pores or grains impinge upon each other. The range of solid volume fractions for the simple cubic model is from approximately 0.52, point contact between particles, to 0.82, contact between necks. The solid volume fraction range for the tetrakaidecahedra models range from minimum values determined by pore to pore contact to full density (solid volume fraction of one). The lower limits for the intermediate and final stage tetrakaidecahedra models are 0.79 and 0.72, respectively.

Common to all of these sintering models is that each model can be reduced to the evolution of a single representative particle and its attendant porosity. Other geometries can be found in the literature but they can also be reduced to the evolution of a single representative particle or cell[70-80]**.** Riedel et. al. have used quasi-equilibrium models of particle-pore interfaces in there models[81,82,83,84]. However, they still reduce the model to one representative particle. These models do not provide a means of imposing a distribution of particle sizes or pore sizes.

Also, the type of porosity is restricted to one location for each model. In real materials pores are located at four location types within a microstructure, corners, edges, faces, and the interior of the grains[85].

The sintering model geometries represent average grains and pores but do not represent real microstructures except for a few special cases in which equisized particles are used[86,87]. However, perfect packing is usually not achieved in these materials resulting in non-uniform densification. An in situ sintering experiment performed by Weiser and De Jonghe tracked the position of each particle and the local densities in a two-dimensional packing of monosized copper spheres[87]. Although the average local solid volume fraction increased from approximately 0.80 to 0.87 through a sintering time of 7.5 hours at a temperature of 1225K, local solid volume fractions both increased and decreased throughout the experiment. Unlike the phenomenological models, which only allow densification, there were regions of de-densification. It was concluded that differential densification, local densification or de-densification, was responsible for particle rearrangement. In addition to densification kinetics these models are applied to predictions of the effect of porosity on mechanical properties[88,89,90,91]. Although there seems to be some success at predicting average properties the models can not reflect changes in processing conditions that affect packing.

2.1.7 Sintering Diagrams

Ashby used the ordered arrangement of spheres and tetrakaidecahedra models to develop a set of sintering diagrams or maps[8,9]**.** The maps predict the dominant mechanisms of densification as a function of homologous temperature (the ratio of the sintering and melting point absolute temperatures) and either the ratio of the neck to particle radii ratio or the relative density. Several thermodynamic, kinetic, geometrical, mechanical property and microstructural parameters such as surface and grain boundary free energy, surface and grain boundary diffusion coefficients, effective surface and grain boundary thicknesses, shear modulus, and grain size are required to calculate the position of field boundaries for each diagram. Therefore, maps must be constructed for each set of parameters and each material. The large number of parameters required and the simple assumed geometries make accurate predictions based on these maps highly unlikely.

2.1.8 Computer Simulation

With the rapidly increasing speed of personal computers more and more simulations of the packing and densification of randomly arranged spheres or ellipsoids are being developed[92,93,94]**.** In some cases a distribution of particle sizes is used and is typically a lognormal distribution[95]. Similar to the representative particle models previously described densification is simulated by an isotropic reduction in particle center to particle center spacing with flat contacts between particles and the simulations do not allow rearrangement of particle positions. More advanced simulations are in the process of being developed using clusters of equisized spheres and size distributions of spheres or ellipsoids randomly distributed in space[95-100]. The evolution of the Dimensionless Microstructural Pathways will be examined in the preliminary work for the early models and compared with experiments.

2.2 IMAGE PROCESSING AND DATA ACQUISITION

2.2.1 Image Acquisition and Enhancement

Image processing procedures are required to obtain data from micrographs. There are many techniques that may be used to enhance an image so that quantitative microstructural data can be determined[101]**.** Furthermore, the appropriate magnification for each sample will depend on the intended use of the data[102]. To measure individual features they must be at least several pixels in size in the digitized micrograph. The sintered alumina samples having submicron sized particles and grains used in this research require the use of a scanning electron microscope to acquire micrographs with sufficient resolution and magnification for image analysis. Several publications covering the techniques of image processing are available. Therefore, only the techniques relevant to this research will be described as needed.

2.2.2 Binary Images

Two binary (black and white) images produced by image processing techniques and manual completion are used for each micrograph or montage. The first is an image that contains information about the pore distribution and structure for each sample. The pores will appear as black areas in a white matrix, Figure 8. The second image is the reconstructed grain boundary image, Figure 8 (bottom right) [103]. Generally, some manual completion of grain boundaries is necessary for each image. The grains will be black with white boundaries and pores. In order to separate particles or grains in an image it is necessary to reconstruct the boundaries with a line of finite thickness. A correction to measured parameters must be made after data acquisition to account for the boundary line thickness. For example, the equivalent circular diameter of a cross-section is typically calculated for each grain or particle, the equivalent diameter is increased by the thickness of the boundary line.

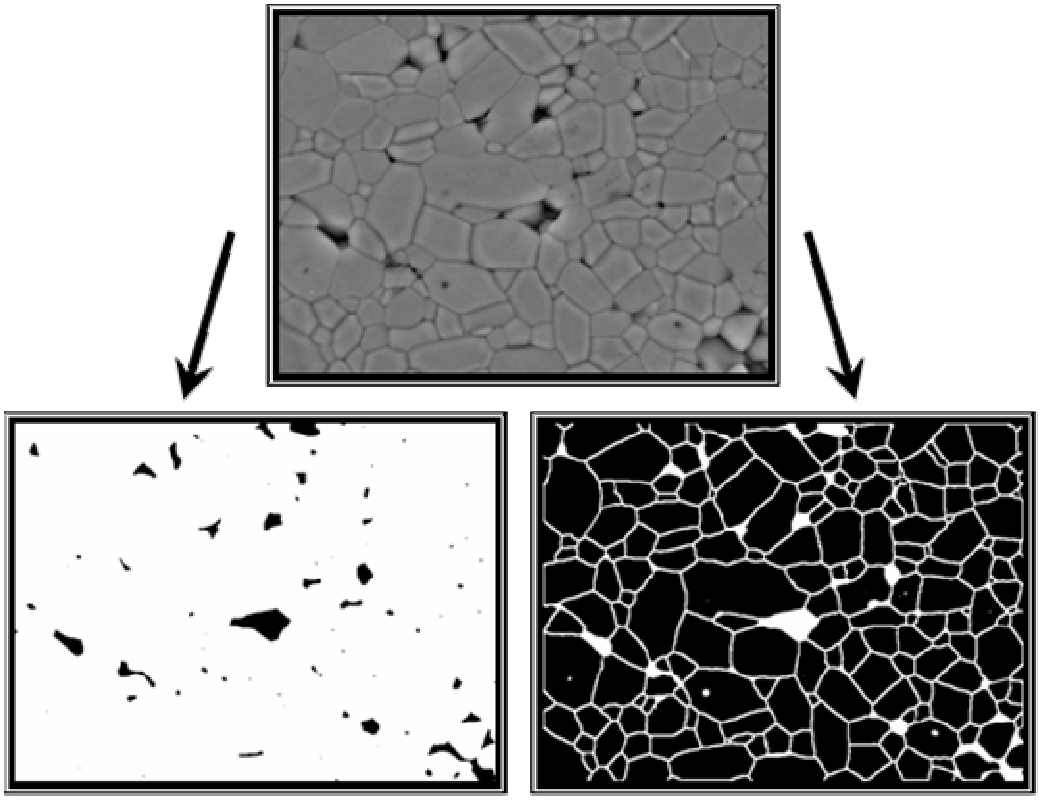

Figure 8: Example of the two binary images required to perform microstructural analysis of sintered samples. The top image is an original micrograph of sintered alumina. The left image is the pores image with black pores and a white matrix of alumina. The right image is the grain image with black grains and white grain boundaries and pores.

2.2.3 Feature and Field Measurements

Several parameters for each feature can be extracted from the binary images including area, perimeter length, position of the centroid relative to the image frame, major and minor axes lengths for an enclosing ellipse with its orientation, and various other measurements and combinations of measurements[104,105]. Also, the calculation of the stereological parameters such as area fraction and surface area per unit volume can be made on the binary images. These are referred to as field measurements because they characterize the entire image rather than individual features.

2.2.4 Edge Effects and Resolution

Throughout all of the images examined in this work, there is a significant effect of the image boundary on the tessellations near the boundary. In order to minimize this effect, appropriate magnifications must be chosen so that several cells will be contained in each image. Because the smallest pore sections comprise a very small fraction of the total porosity, lower magnifications that would not be appropriate to examine the overall area fraction of pores may be used. This in effect will provide a filtering of the pore section size to a minimum of 1 pixel in a digital image. The fraction of pore sections not imaged due the resolution of the digital image can be determined using the stereological measure of solid area fraction and the relative density measurement by the Archimedes method. In order to maintain the same resolution for each sample, the micrographs for each sample are collected at the same magnification (area per pixel).

2.3 STEREOLOGY

2.3.1 Microstructure Average Parameters

Quantitative Stereology provides methods of determining average properties of a three dimensional microstructure from two dimensional materialographic sections[106-110]. These well established techniques require no geometric assumptions for isotropic microstructures. Of importance to this research is the measurement of solid volume fraction, V_V, and surface area per unit volume, S_V. The solid volume fraction or relative density of a single phase material can be determined by three stereological methods, point counting, intercept lengths, and area measurement. The relationship, $V_V = P_P = L_L = A_A$, expresses the equality of the three methods. P_P is the number of points of a randomly placed test pattern of points that fall within the phase of interest divided by the total number of test points. L_L is the total intercepted length of test lines

divided by the total length of the test lines. The last, A_A, is the total area of cross-section of a phase divided by the total cross-sectional area. The Archimedes method is used to determine the relative density or solid volume fraction of material to verify the stereological estimation of solid volume fraction[111].

The surface area per unit volume of a sample can be calculated by two stereological methods. The first, $S_V = 2P_L$, requires only to count the number of times a test line crosses the boundaries (P) of the phase of interest and divide by the total length of test line. The second, $S_V = (4/\pi)L_A$, requires the measurement of the perimeter length of the phase of interest, L, and the total cross-section area, A. In materials with multiple phases there will be more than one boundary type possible[112-118]. In the case of a porous single phase material there will be solid-solid and solid-vapor boundaries. Solid-solid interfaces (particle or grain boundaries) are shared by two particles and one half of the shared surface will be associated with each. The solid-vapor interfaces (pore-particle boundaries) are free surfaces and the total area is not shared. The corresponding symbols for solid-solid and solid-vapor surface area per unit volume are S_V^{SS} and S_V^{SV}, respectively.

2.3.2 Feature Average Parameters

The relationships, $V_V = A_A$ and $S_V = 2P_L$, were chosen for this research because they are easily implemented using image analysis. The microstructural parameters, mean pore intercept length ($\bar{\lambda}^v$) and mean grain intercept length (assuming pores are located on grain boundaries, $\bar{\lambda}^s_g$), can be calculated directly from the solid volume fraction and the surface area per unit volume by Equation 3 and Equation 4. These parameters characterize feature averages of the microstructure.

$$\text{Equation 3: } \bar{\lambda}^v = \frac{4\bullet(1 - V_V)}{S_V^{SV}}$$

$$\text{Equation 4: } \bar{\lambda}^s_g = \frac{4\bullet V_V}{S_V^{SV} + 2\bullet S_V^{SS}}$$

The average microstructure parameters, V_V, S_V^{SS}, S_V^{SV}, $\bar{\lambda}^v$, and $\bar{\lambda}^s_g$, are applicable to isotropic microstructures without the need for any shape assumptions. These parameters are readily calculated using image analysis data and can be used to compare average values of very different materials and models. However, the generality of these measurements may render them inadequate as a basis of comparison of modeled and real microstructures.

2.4 DIMENSIONLESS MICROSTRUCTURAL PATHWAYS

2.4.1 Dimensionless Parameters

The average microstructure parameters, S_V^{SS}, S_V^{SV}, $\bar{\lambda}^v$, and $\bar{\lambda}^s_g$, all have units of length or inverse length. In order to compare the geometric models with experiment independent of scale, three dimensionless microstructural parameters, the solid-solid surface area to solid-vapor surface area ratio (Ψ) (Equation 5), the mean grain intercept length to mean pore intercept length ratio (Λ) (Equation 6) [119], and the mean pore spacing (Equation 7) to mean grain intercept length ratio (Σ) are calculated (Equation 8). The dimensionless ratios are plotted versus solid volume fraction for comparison of the evolution of the real and simulated microstructures independent of time and length scale.

$$\text{Equation 5: } \Psi = \frac{S_V^{SS}}{S_V^{SV}}$$

$$\text{Equation 6: } \Lambda = \frac{\bar{\lambda}^S_g}{\bar{\lambda}^V} = \frac{V_V \bullet S_V^{SV}}{(1 - V_V)\bullet(S_V^{SV} + 2\bullet S_V^{SS})}$$

$$\text{Equation 7: } \bar{\lambda}^S_p = \frac{4\bullet V_V}{S_V^{SV}}$$

$$\text{Equation 8: } \Sigma = \frac{\bar{\lambda}^{S}_{p}}{\bar{\lambda}^{S}_{g}} = \frac{S_V{}^{SV} + 2 \bullet S_V{}^{SS}}{S_V{}^{SV}}$$

2.4.2 Phenomenological Models

The Dimensionless Microstructural Pathway (DMP), surface area ratio versus solid volume fraction for the geometries of the phenomenological models of sintering are shown in Figure 9 with data from the previously described results of Sacks and Yeh. The pathway for the initial stage model is the simple cubic arrangement of spheres. The intermediate stage model is of Kelvin tetrakaidecahedra with cylindrical pore channels on particle edges. The final stage model is of the Kelvin tetrakaidecahedra with spherical pores located at particle corners[120,121]. The geometries of these models are depicted in Figure 10. The Sacks and Yeh data of surface area ratio for flocculated alumina appears to fit the simple cubic model until a solid volume fraction of 0.75 and the final stage model beginning at a solid volume fraction of 0.93. However, the data for the dispersed alumina only fits the simple cubic model until a solid volume fraction of 0.77 but does not fit any of the other models. While the models may fit some of the data some of the time the models do not fit all of the data all of the time. The DMPs are adequate for comparing model geometries but tend to be insensitive to differences in processing conditions until grain growth becomes significant at solid volume fractions of approximately 0.9.

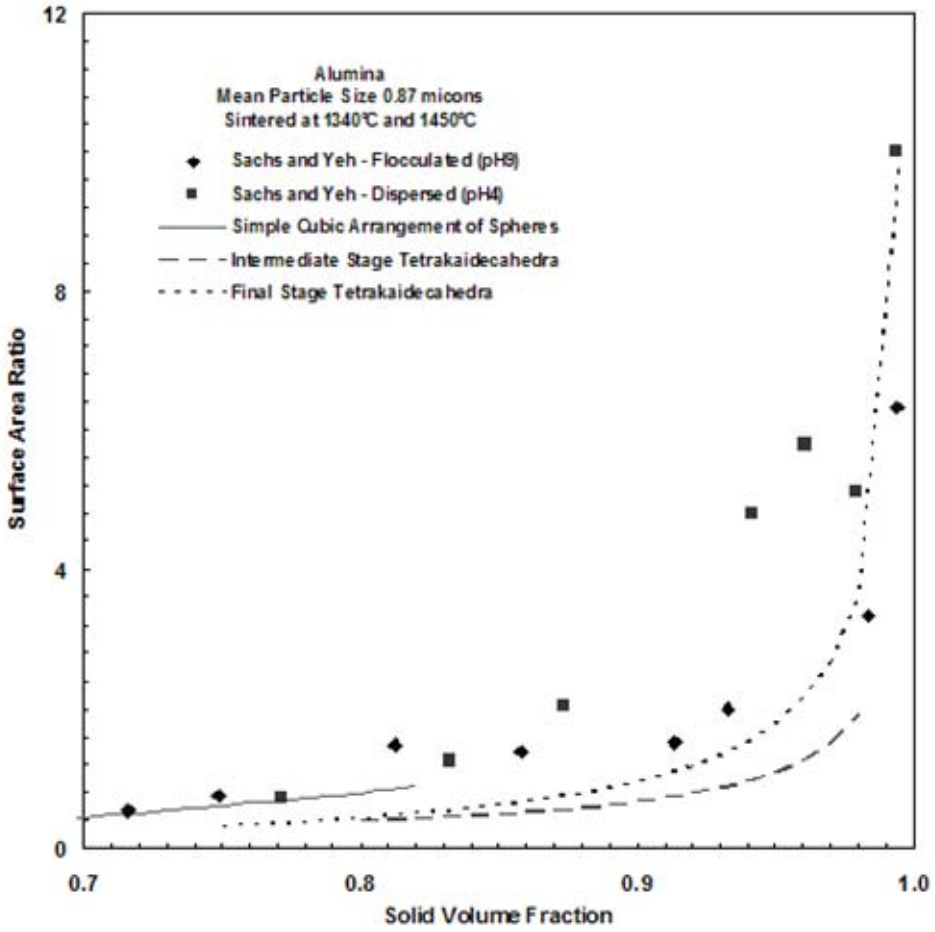

Figure 9: Evolution of the DMP, solid-solid to solid-vapor surface area ratio, Ψ, versus solid volume fraction for the alumina samples of Sacks and Yeh along with the predictions from the phenomenological sintering models. Although in general the fit is not good there are solid volume ranges over which the flocculated (pH9) samples agree with the model predictions. In the case of dispersed alumina (pH4) there is virtually no agreement with the model predictions.

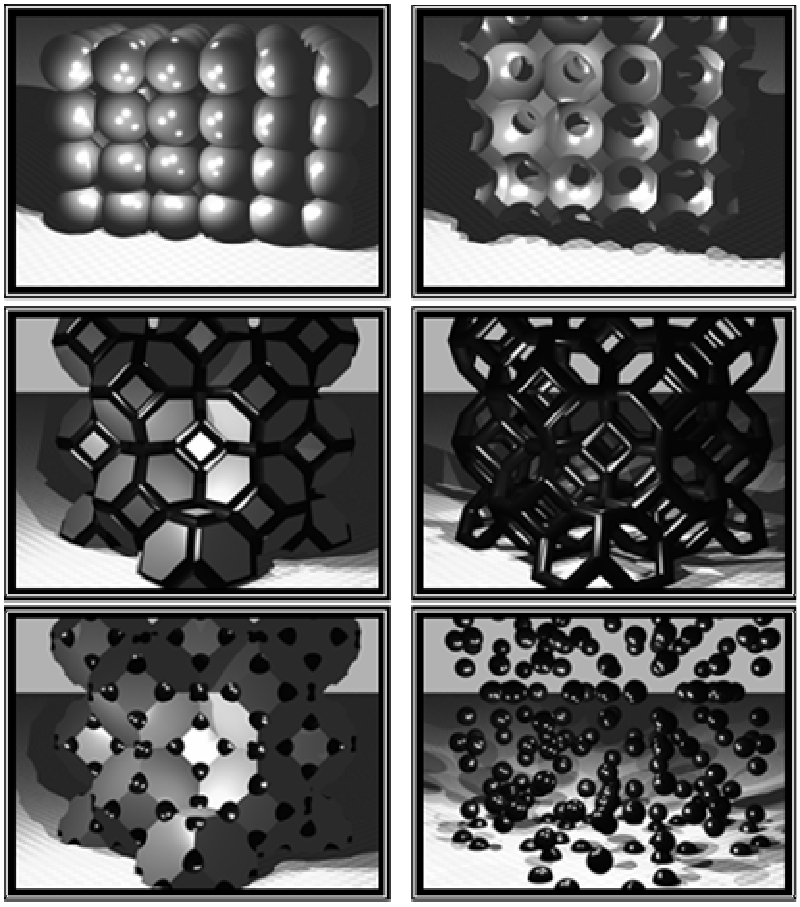

Figure 10: Illustrations of the phenomenological sintering model geometries. The images on the left are of the solid portion of the models. The images on the right are the attendant porosity for the corresponding model to the left. The top images illustrate the intermediate stage model using equisized spheres on a simple cubic lattice. The middle images show the intermediate stage model of Kelvin tetrakaidecahedra with cylindrical pore channels along particle edges. Lastly, the bottom images illustrate the Kelvin tetrakaidecahedra with spherical pores on particle corners for the final stage model.

2.5 GRAIN AND PARTICLE SIZE DISTRIBUTIONS

2.5.1 True Grain Size

The mean grain intercept length calculated using the stereological parameters of solid volume fraction and surface area per unit volume is one measure of the average particle size. However, evolutions of sintered microstructures are dependent on the distribution of particle size as well. Therefore, in addition to the dimensionless pathways, the evolution of the particle size distribution is characterized. Typically, the grain size is given as the size of cross-sections of grains rather than the 'True' grain size, the characteristic size in three dimensions. It is difficult to measure the three dimensional size of particles or grains of an opaque material. Some researchers have resorted to serial sectioning[122,123] or tomography methods[124]. But, their uses are limited due to the amount of time required to reconstruct the microstructure from sections and the thinness of sections required or the resolution of the technique. Serial sections would have to be considerably thinner than the size of the smallest grains. Serial sectioning would be possible but not practical for the alumina samples with submicron grain sizes at the time of this work.

2.5.2 Statistical Methods

Statistical methods devised by Saltykov and others of three dimensional grain or particle size determination from two dimensional sections have been used for several decades[125-130]. However, these techniques have not been widely used due to the occurrence of negative frequencies in the results and the lack of analytical expressions for the intersection probability functions for non-spherical particles. The probability of intersecting a particle at its center with a randomly oriented and positioned planar probe is extremely low. Therefore, it is necessary to determine, $P_{i,j}$, the probabilities of obtaining a section of size (D_{i-1} to D_i) from a particle with a

three dimensional size (D_j, $D_j \geq D_{i-1}$). This is illustrated in Figure 11 for spheres. Particles with size D_j greater equal to D_{i-1} can result in sections of size D_{i-1} to D_i if the plane intersects the particle. The number of cross-sections measured with size D_{i-1} to D_i will include sections from particles of size D_j equal to D_{i-1} or greater. The grain size determination methods can be expressed by the matrix relation, $N_A = P \cdot DN_V$, where N_A is the measured frequency distribution of the number of cross-sections per unit cross-section area, P is the probability matrix with elements (i,j) equal to $P_{i,j}$, and DN_V is the product of the diameter and frequency for each class of the three dimensional particle size distribution per unit volume. To estimate the three dimensional distribution, N_V, requires the solution of the matrix equation in which the probability matrix must be inverted. Therefore, these methods are termed as inverse or unfolding methods[104-110,125-130].

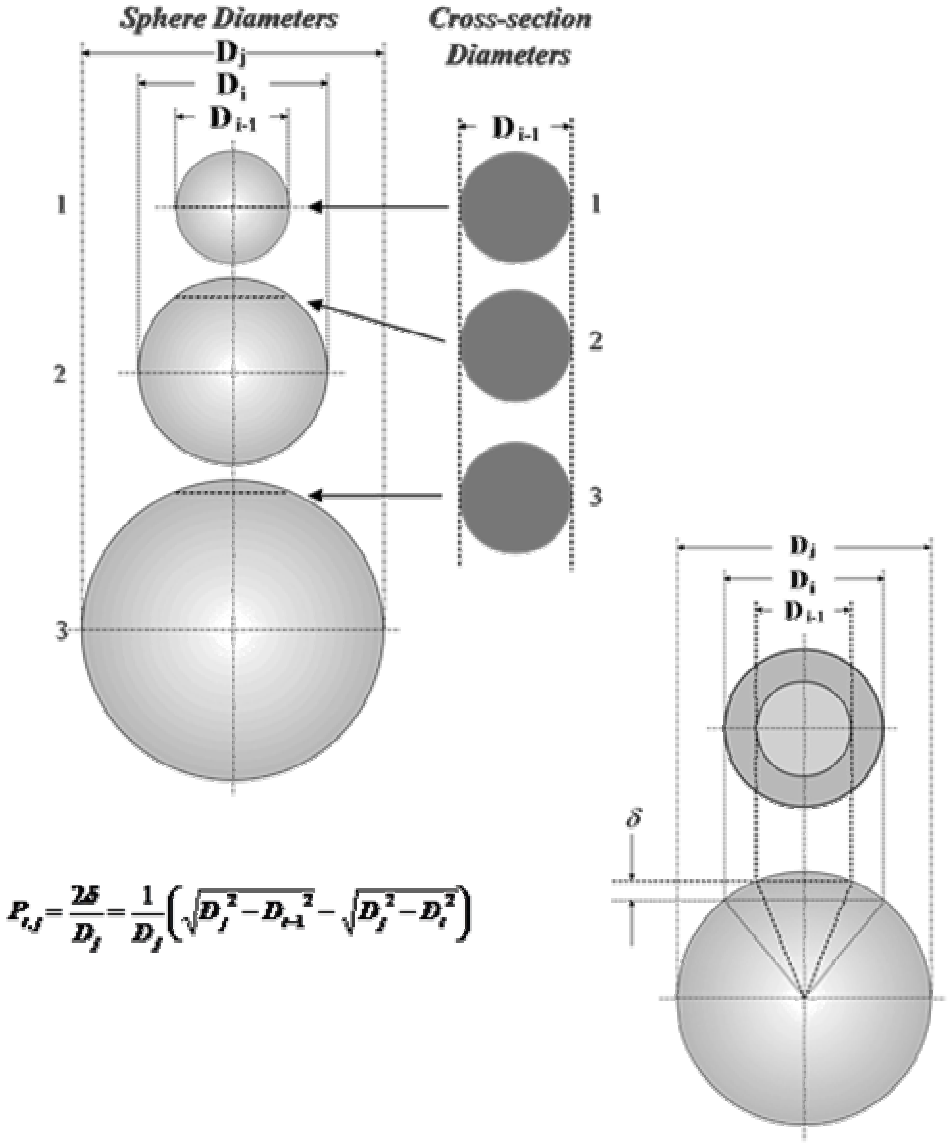

Figure 11: The illustrations above depict the result of sectioning a sphere with a plane that does not pass through the center of the sphere. Spheres of different sizes can yield the same cross-section area or diameter as illustrated in the left image. The probability given by the equation above is the probability of obtaining a cross-section of a diameter within the range, Di-1 to Di, from a sphere with diameter Dj. These probabilities are used to calculate three dimensional grain size distributions from the measurement of cross-section diameters.

2.5.3 Saltykov Methods

In the first half of the 20th century, when the unfolding methods were developed, computers were not available to perform the many calculations necessary to apply the statistical methods in a more flexible manor. The techniques advanced by Saltykov use spheres as the assumed shape and arbitrarily chosen class boundaries to minimize the number of required calculations[125-130]. The first method uses classes of equal increments in diameter and the second uses equal increments of cross-section area. By limiting the class boundaries it is possible to produce tables of values based on the probability of intersecting spheres with a randomly oriented plane to estimate the three dimensional distribution of grain size. These tables, derived using cross-section size normalized by the maximum measured cross-section size, had to be calculated only once and are actually the inverse of the probability matrix, P. The probability function $P_{i,j}$ for the equal diameter and equal area increment Saltykov methods are given by Equation 9 and Equation 10, respectively. Restricting the class boundaries allowed the methods to be more readily applied but, the problem of negative frequencies in the grain size distribution occurs frequently.

$$\text{Equation 9: } P_{ij} = \sqrt{j^2 - (i-1)^2} - \sqrt{j^2 - i^2}$$

$$\text{Equation 10: } P_{ij} = \sqrt{j - (i-1)} - \sqrt{j - i}$$

2.5.4 Fitting and Forward Methods

Others have devised techniques to circumvent the problem of negative frequencies by assuming a particle size distribution type such as lognormal, Weibull, or gamma distributions131. Although it has been found that some three dimensional particle size distributions follow these statistical distributions, not all will obey these statistics, classified ceramic powders for example[132,133,134]. A logical alternative to the inverse methods, developed by Schwartz, Wasén and Warren, and others, is to use a forward method[135-144]. In this case, a theoretical three dimensional particle size distribution is assumed and the distribution of cross-section size is calculated for an assumed shape. The theoretical distribution is adjusted class by class until reasonable agreement is reached between the calculated and experimental distributions of cross-sections. A χ^2 test is used to determine the best solution[145,146].

The forward and inverse methods can use probability functions for non-spherical shapes. However, except for a few cases analytical solutions are not available and computer simulations of the sectioning of particles based on geometrical probability theory must be used[147,148]. Simulations were used in the early 1980's to produce these probability distributions for convex polyhedra and a catalog was published by Wasén and Warren[149]. In the catalog, an example was given by applying the forward method with the probability distribution for truncated trigonal prisms to a cemented tungsten carbide. The number and width of class boundaries were again arbitrarily set in the forward method. Generally, if the inverse method results in negative frequencies, the class containing the smallest particle cross-sections for the distribution calculated using the forward method will not match the experimentally measured distribution. A schematic of forward and inverse grain size determination methods is given in Figure 12.

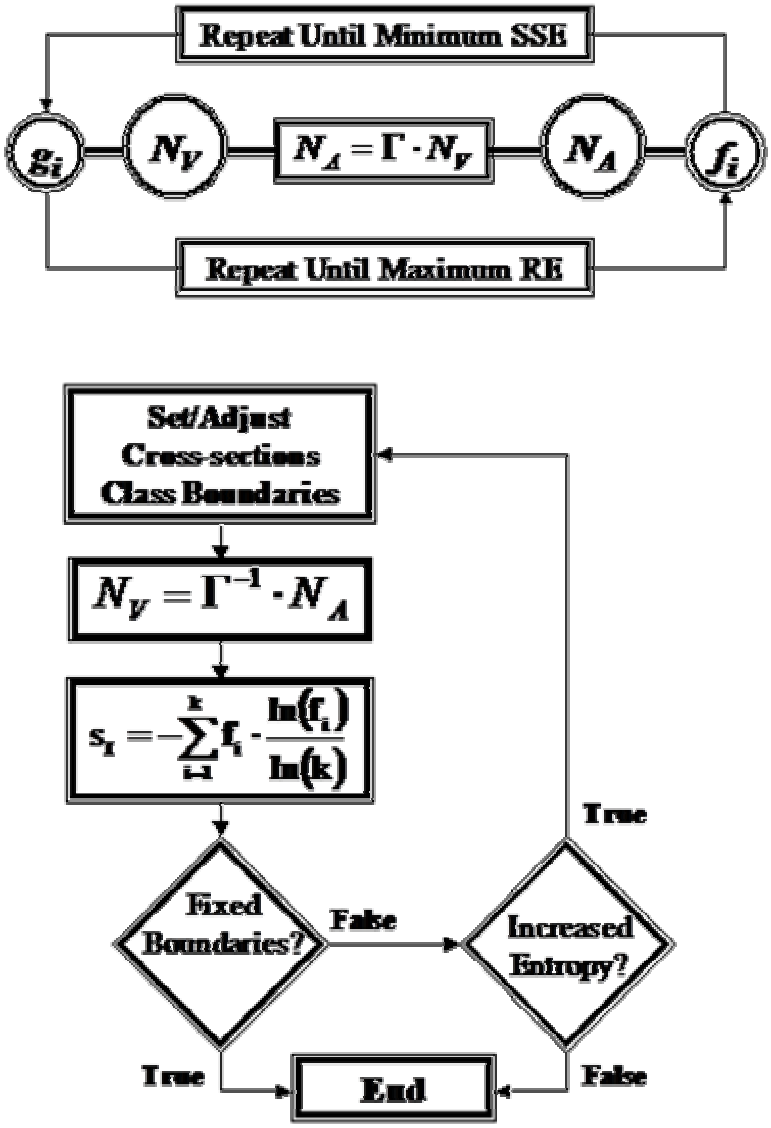

Figure 12: The flow charts above illustrate the methods of particle size determination that use geometric probabilities to estimate distributions from section information. The top loop of the top schematic represents the forward methods and the bottom loop represents the inverse methods. The bottom schematic shows the introduction of Relative Information Entropy into the inverse method. The cycle of adjusting distribution classes is repeated until no increase in entropy occurs.

The occurrence of negative frequencies with the inverse methods is usually blamed on an accumulation of error in the matrix inversion. This reasoning is also used to justify the difference between calculated and experimental distributions of cross-sections when applying the forward method. While there is an accumulation of error in the smaller classes, the primary reason for the occurrence of negative frequencies is due to the arbitrary choice of class boundaries. The next

logical step is to remove the restriction on class boundary widths. Unfortunately, a very large number of possible combinations of classes is possible for a given cross-section distribution. Some guideline as to how boundaries should be determined must be applied to obtain credible and reproducible results.

2.5.5 Grain Morphology

The grain size distribution obtained using the statistically based forward and inverse methods from grain section distributions can be very sensitive to the shape assumption. Wasén and Warren[149] gave an example of the distributions obtained using truncated trigonal prisms for cemented tungsten carbide. However, they only briefly mention the method of selecting the appropriate shape. The selection of the appropriate particle shape was based on the distribution in the shape factors of grain and simulated polyhedron cross-sections. The shape factor, Q, defined by Equation 11, where A is the area of the section and U is the perimeter length of the section, is always greater than zero and has a value of 1 for circular sections. All other shapes will have values less than one. The selection was based on a comparison of the moments of the distributions in Q for both experimental measurements and simulated section results.

$$\text{Equation 11: } Q = \frac{2\pi A}{U^2}$$

2.5.6 Distribution Parameters

Particle and grain size distributions commonly follow lognormal, Weibull, or gamma distribution statistics[150,151,152,153]. Each of these distribution types requires at least two parameters to characterize the distribution. Descriptions of these distributions can be found in probability and statistics text books. An example of the fitting of each of these distributions to one of the alumina samples is given in the results section. In this work it was found that lognormal statistics gave reasonably good fit to all but a few of the alumina distributions measured. The frequency distribution function for lognormal statistics is simply the normal distribution of the logarithm of the measurement parameter, Equation 12. The two parameters that describe the distribution are the geometric mean, μ, which also equals the median for lognormal distributions, and the

geometric standard deviation, σ. The mean and standard deviation can be determined for a lognormal distribution using a lognormal probability plot which plots cumulative frequency by increments of standard deviation versus the logarithm of size. A lognormal distribution will show a linear relationship on the plot and the mean and standard deviation are calculated using a least squares fit[147]. Also used to characterize distributions is the coefficient of variation, CV. For lognormal distributions the CV is a function of the standard deviation, Equation 13. Both the geometric standard deviation and the coefficient of variation are dimensionless parameters. The evolution of these parameters is also examined in this research.

$$\text{Equation 12: } f(x) = A \bullet \exp\left[\left(\frac{\ln(x) - \ln(\mu)}{\ln(\sigma)}\right)^2\right]$$

$$\text{Equation 13: } CV = \sqrt{\exp\left[\ln^2(\sigma)\right] - 1}$$

The distribution of particle size given in Figure 2 for alumina is weighted by particle volume[154]. The cumulative frequency undersize indicates the fraction of the total volume contributed by all particles with diameters less than the corresponding diameter to the cumulative frequency. The grain or particle size determination methods previously described use distributions by number of particles and not by volume of particles. The weighted and unweighted particle size distributions are significantly different because small particles have less volume than large particles. For example, 1000 spherical particles with diameters of 1 micron will have the same volume as 1 spherical particle with a diameter of 10 microns. The mean diameter for the volume weighted distribution will be considerably higher than the mean for the distribution by number. An advantage of using lognormal distributions is that the standard deviation and the coefficient of variation are the same for any weighting of the distribution.

The dimensionless parameters, standard deviation and coefficient of variation, can provide another means of comparing experimental results with models as another DMP. This will be of little use for models that do not allow distributions in grain or particle size. However, they can be used to compare simulations that use random arrangements of particle size distributions with experiment. An example of a simulation by Kumar Krishnan that uses a particle size distribution of spheres based on experimental results from the sintered alumina samples is presented in the results.

2.5.7 Information Entropy Based Method

A modified method of determining three dimensional size distribution, designed to eliminate the arbitrary selection of class boundaries, using class boundaries that maximize the relative information entropy of the frequency distributions is presented in the results. The method can be applied to either inverse or forward methods. Information entropy has been used in many fields including materials science to classify data to extract the most information possible[155-159]. The relative information entropy, calculated value divided by the maximum possible entropy, is a measure of the efficient use of information. An early application of information entropy was to communication theory by Shannon as a method to obtain reliable data from a noisy signal. Information entropy is commonly referred to as the Shannon entropy and is given by Equation 14 for discrete frequency distributions. Maximum Relative Information Entropy (REI), s_I = 100%, is attained by having equal frequencies, f_i, in each class i of the total number of classes, k. This is not likely to occur for grain size distributions obtained using statistical methods. However, as presented in the preliminary results, values in excess of 95% are possible for the sintered alumina samples. Application of this method is performed using a computer program that iteratively adjusts class boundaries until the maximum entropy for the distribution is achieved.

$$\text{Equation 14: } s_I = -\sum_{i=1}^{k} f_i \bullet \frac{\ln(f_i)}{\ln(k)}$$

2.6 TESSELLATION

2.6.1 Point Tessellation

The distribution of near neighbor distances is a subset of the radial distribution functions[160,161,162,163]. In some cases the first, second, and higher order near neighbors have been investigated. It has not been shown what order near neighbor is necessary for the determination of clustering. A method to eliminate the ambiguity of significant near neighbors is the use of Dirichlet tessellation[164-168]. The method of tessellation can be traced back to the time of Descartes, 1644. Descartes segmented the matter in the universe into regions using the sun and stars as tessellation nodes. Dirichlet or Voronoi tessellations uniquely segment an area containing a spatial distribution of points using boundaries that contain the regions in which all positions are closer to the point contained within that boundary than any other point. The complement to tessellation is Delaunay Triangulation. Lines connecting the points of adjacent cells forms the triangulation of a tessellation which is referred to as its dual. The voronoi cell boundaries contain all positions that should most strongly be influenced by the point in the cell. Once a cell structure has been identified various parameters and distributions of parameters can be determined including area, perimeter length, aspect ratio, coordination number or the number of sides, near neighbor distances, and nearest neighbor distance. A comparison of cell parameters with simulated tessellations of random distributions can identify the presence of clusters. Based on computer simulations, the cell area and aspect ratio have been identified as the strongest indicators of clustering. However, the ratio of the mean nearest neighbor distance to the mean for a random spatial distribution was also found to be an effective indicator of clustering[23,169]. Two examples of tessellation and triangulation for two simulated spatial distributions of second phase particles, clustered and well dispersed, are given in **Figure 13**. There is a wider distribution in cell sizes and near neighbor distances for the clustered arrangement.

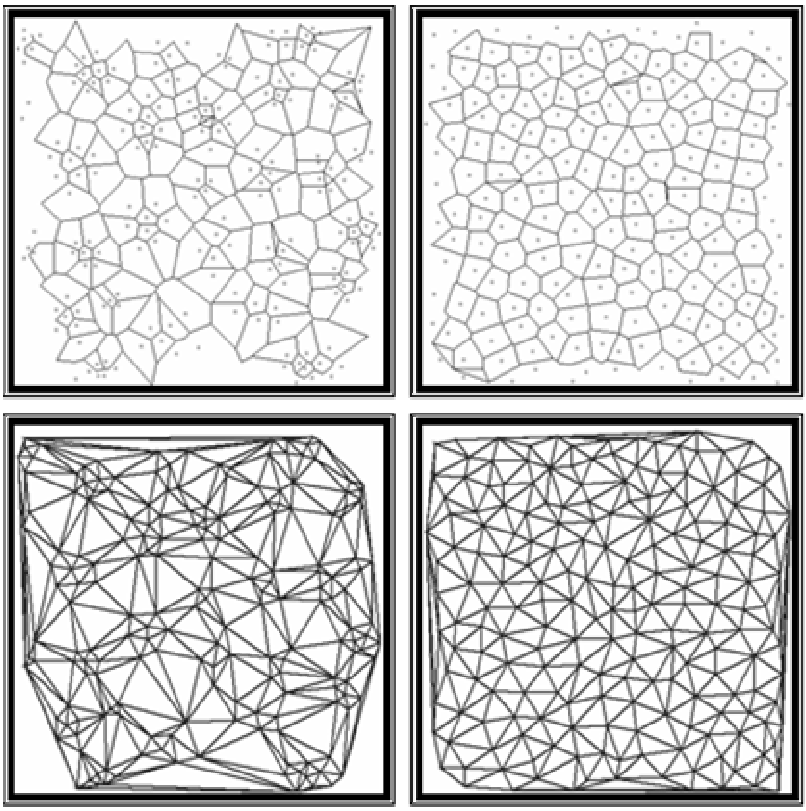

Figure 13: The images above demonstrate the methods of tessellation and triangulation. The point pattern on the left is clustered in comparison to the more uniform pattern on the right. The top images are the voronoi or Dirichlet tessellations. The bottom images are the duals of the tessellations, the Delaunay triangulations.

2.6.2 Boundary Tessellation

Tessellations are not restricted to segmenting a region based solely on particle centers as previously described. In addition to the point tessellations, tessellations can be weighted by the size or mass of the particle. A method of interest for microstructure evaluation is the tessellation from feature boundaries rather than feature centers. Boundary tessellations are similar to point tessellations in that all positions within a tessellation cell are closer to the feature contained within the cell than to any other feature within the region (micrograph). The difference between the point and boundary tessellations is that the size and morphology of the feature will affect the size and morphology of the tessellation cell.

In essence, the tessellation from the boundary is a radial dilation of the feature (**Figure 14**). The boundaries of all of the features are radially expanded until all of the section area is consumed. When points of the boundaries of neighboring features impinge upon one another the points become fixed (**Figure 15**).

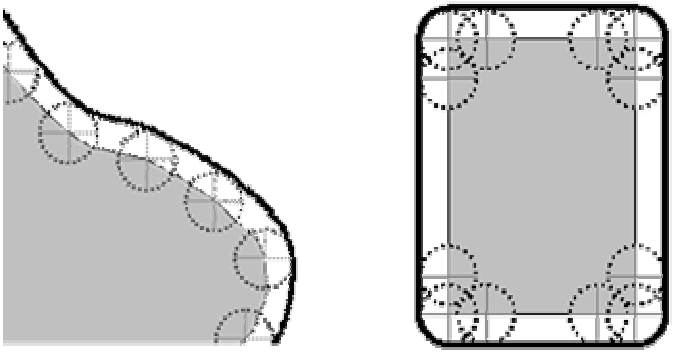

Figure 14: The image on the left illustrates the radial dilation from a 'rough' boundary while the image on the right represents the radial dilation from a rectangle. Not shown is the radial dilation of a circle, which is of course just a larger circle. The effect is the rounding off of sharp corners and perpendicular expansion of straight boundaries.

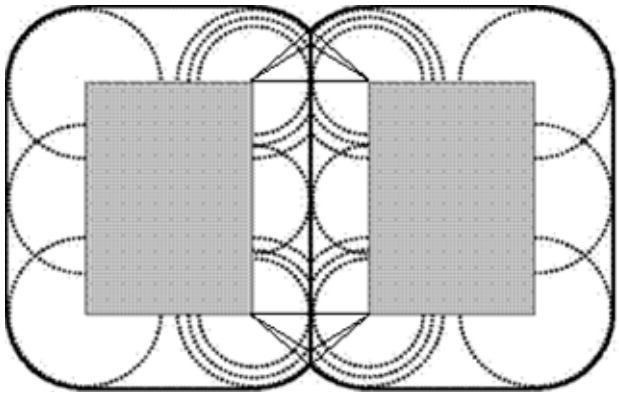

Figure 15: The expansion of boundaries stops when boundaries impinge upon the boundaries of neighboring features. Only the points of contact become fixed. Dilation continues until the entire section area is associated with tessellation cells.

The process of dilation of a pixilated image is slightly different. Instead of using a radial dilation, a template of pixel positions must be used. The shapes can include a square with odd numbers of pixels per side, a cross with odd numbers of pixels from top to bottom and left to right, or other symmetric templates. The template implemented in the tessellation software is referred to as an octagon (**Figure 16**). This more closely imitates the radial dilation than the other templates. An example of the dilation of a square is also given in **Figure 16**. The pixel in the center is the one being evaluated. The center pixel is replaced by the mode of the color or grayscale values of the surrounding pixels. For example if the majority of the neighboring pixels are black, the center pixel is replaced by a black pixel. In order to work properly, the replacement is placed within a 'new' image and the dilation continues on the original image. In cases where there are two or more color values equal to the mode, one of the values is selected by random number generation. In rare situations this can result in isolated pixels surrounded by pixels of another color. Results will show that the occurrence is very rare, one in several million pixels, and will not have a significant impact on the accuracy of the results.

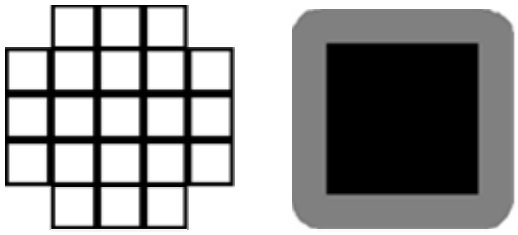

Figure 16: The illustration on the left is the octagonal template used during dilation to perform the tessellation operation. The pixel in the center will be determined by the neighboring pixels within the template area. The image to the right is a dilation of a square using the octagonal template. The corners round off as would be expected for a radial dilation.

2.6.3 Tessellation Cell Parameters (Immediate Environment)

Tessellation cells can be treated as features. Therefore, parameters typically associated with features such as grains or pores can be measured for cells as well as derived parameters such as shape factors. The parameters are then associated with the immediate environment of the feature. In addition to the typical feature measurements (area, perimeter length, Ferét dimension, etc.), boundary tessellation cells have two distinct features with measures of size, the size of the

feature contained within the cell and the size of the cell. A cell parameter derived from the two area measurements of the tessellation cell of a pore is the cell's Solid Area Fraction (SAF). This is the fraction of the cell area not associated with the pore and is given by Equation 15, where CA is the total Cell Area and PA is the Pore section Area (**Figure 17**). In the study of the two dimensional in situ sintering of copper spheres, Weiser, and De Jonghe referred to the cell solid area fraction of tessellation cells (of particles rather than pores) as the 'local solid volume fraction[87]. They found that local solid volume fractions could decrease as well as increase as the global solid volume fraction increases. A decrease in local solid volume fraction with an increase in the global solid volume fraction is referred to as de-densificaton.

$$\text{Equation 15: } SAF = \frac{CA - PA}{CA} \text{ ; } (0 < SAF < 1)$$

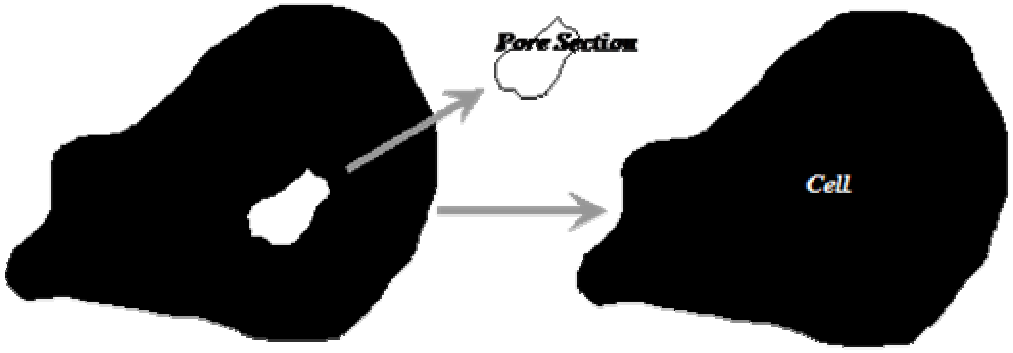

Figure 17: The area of a tessellation cell of a pore can be divided into different areas. The center image is solely of the pore section with its associated area, PA. The image to the right represents the total area of the cell, CA, which includes both the pore section area and the solid area associated with the cell.

The solid area fraction of a tessellation cell should not be confused with the solid area fraction (A_A) of a materialographic section. The solid area fraction of a materialographic section is equal to the solid volume fraction of the material (V_V) for a single phase material. Among other assumptions, this result requires that a statistically significant portion of the microstructure has been sampled. No equality of solid area and volume fractions is assumed in the case of tessellation cell SAF. The solid area fraction, A_A, can have only values greater than or equal to 0 and less than or equal to 1 ($0 \leq A_A \leq 1$). However, cell SAF values must be greater than 0 and

less than 1 ($0 < SAF < 1$). Tessellation cells must contain a pore of finite size. Therefore, PA is always less than CA and greater than zero.

Equation 15 indicates that as the size of the pore section increases relative to the total size of the cell, the cell SAF decreases. Therefore, cells containing relatively small pores will have high SAF values and cells containing relatively large pores will have low SAF values (**Figure 18**). The SAF of a cell is independent of the position of the pore within the cell. However, if there is more than one coordinated cell (neighboring cell with boundaries in contact) the SAF gives an indication of the relative spacing between features contained in coordinated cells due to the fact that the boundaries are equidistant from adjacent cell features.

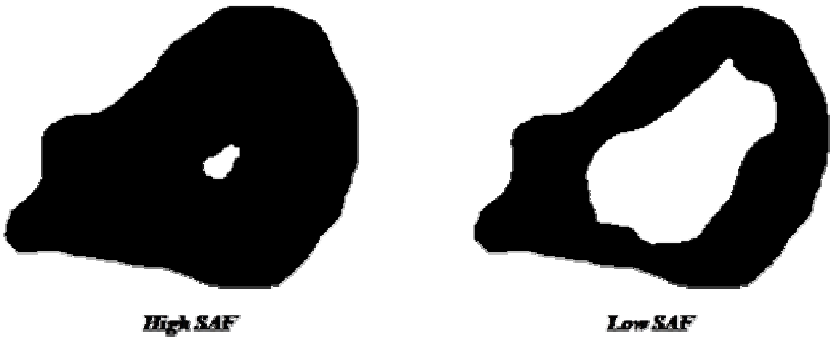

Figure 18 : The image on the left illustrates the tessellation cell of a small pore (relative to the cell size) having a high cell solid area fraction (SAF), CA >> PA. The image on the right illustrates a low SAF cell where PA ≈ CA (SAF ~ 0.5).

2.6.4 Nearest Neighbor Parameters (Immediate Environment)

The local environment of pore or feature sections can also be characterized using the tessellation method. The properties of neighboring tessellation cells can be used to obtain additional parameters for individual cells. These include the two-dimensional coordination of cells (CN), Local mean Pore Area (LPA), and the Local Solid Area Fraction (LSAF). The local mean pore area is given by Equation 16 and Equation 17, respectively, where n is the number of coordinated cells, $(PA)_i$ is the pore section area associated with each coordinated cell, and $(CA)_i$ is the area of each coordinated cell. Notice that these equations do not include the size of the cell of interest.

$$\text{Equation 16: } LPA = \frac{1}{n}\sum_{i=1}^{n}(PA)_i$$

$$\text{Equation 17: } LSAF = 1 - \frac{\sum_{i=1}^{n}(PA)_i}{\sum_{i=1}^{n}(CA)_i}$$

2.6.5 Statistics

The segmentation of the microstructure by tessellation completely subdivides the section into cells which can be described by various measures of size and derived parameters. These measurements and parameters constitute a set of data which can be analyzed in various ways. In addition to the commonly used characteristic parameters (averages, maximums, minimums, etc.), the distributions can be examined in detail. Distributions in the frequency of one parameter plotted with respect to another have been discussed in the section concerning grain / particle size. These distributions do not typically incorporate any correlation between parameters. It is usually necessary to use distribution in frequency plotted in terms of two or more parameters to understand the correlation between parameters.

A plot of frequency for two parameters results in either a three-dimensional plot or a contour plot. The plot is in effect a two dimensional histogram. As an example, the histogram for the size of a pore section and the dimensionless shape factor, Q, for a dispersed alumina sample held at 1350°C for 0.2 hours is given in **Figure 19**. The pore size (area) is divided into 20 bins or classes of equal increments in the log(PA) from 0.01 to 10 square micrometers and the Pore Q is divided into 20 bins or classes of equal increments in Q from 0 to 1. The height of each column is proportional to the number fraction of pores that have both a size and Q that fall into the range of the bin. The highest peak in **Figure 19** is associated with pores within a size range of 0.020 to 0.027 square microns and Q within a range of 0.60 to 0.65 ($0.020\ \mu m^2 < PA \leq 0.027\ \mu m^2$ and $0.60 < Q \leq 0.65$). The bin contains 2.7% of all pores measured.

The difficulty with the three-dimensional histogram is that you can not observe every portion of the plot at the same time. A contour plot is the solution. **Figure 20** is the contour plot associated with **Figure 19**. Again the size and shape factor are divided into 20 bins each. The grayscale value of the bin is proportional to the relative frequency associated with that bin. The darkest bin is the bin containing the largest fraction of pores. The white area has either no pores or very few pores associated with it. The contour plot can also use color to indicate frequency instead of grayscale value. In this work the color scale runs from gray to blue to green to red for increasing fraction or frequency.

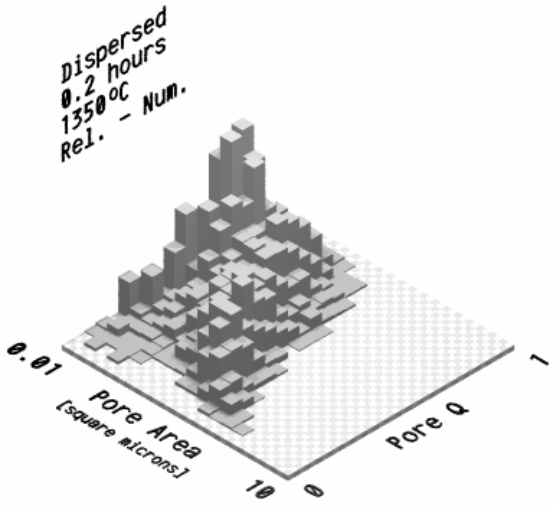

Figure 19: Three-dimensional histogram of the relative frequency of pores by size and shape factor (Q) for dispersed alumina sintered at 1350°C for 0.2 hours.

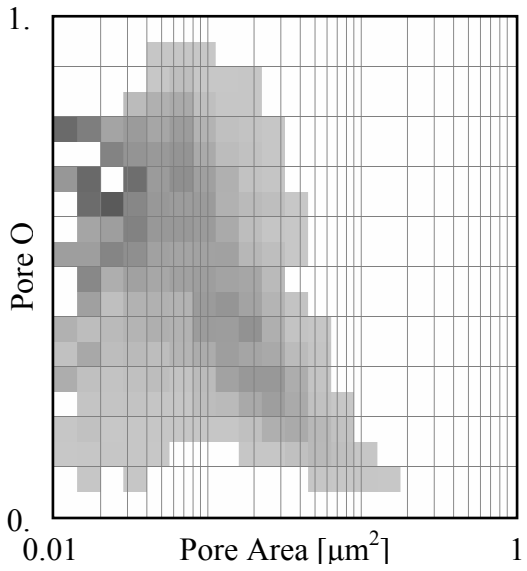

Figure 20: Two-dimensional contour for the same data used in Figure 19. In this case the grayscale value of the bin is related to the relative frequency for the bin.

2.7 SUMMARY

Sintering and Hot Isostatic Pressing are technically important processes for the production of components made from powder materials. The following is a summary of some of the important points discussed in the background section of this report regarding this study:

- The underlying driving force for the densification of materials by these processes is the reduction in free energy by the reduction of surface area.
- Densification is defined as the isotropic reduction in the center to center spacing of individual particles or grains. Only mechanisms that remove matter from the boundary between particles result in densification.
- Analysis of the Sacks and Yeh[18] data from the sintering of alumina powder at 1340°C indicates that densification rates and microstructural average properties are influenced by flocculation during the casting process.

- The mean pore intercept ratio remains constant through the intermediate stage of sintering for alumina sintered at 1340°C.
- Grain coarsening is avoided through the intermediate stage of sintering at 1340°C in flocculated alumina.
- The phenomenological modeling of sintering has been used for several decades. The simple assumed geometries using a single representative particle and its attendant porosity, do not allow the simulation of real microstructural characteristics such as grain size distribution, pore size distribution, variation of pore or grain geometries with changing solid volume fraction, rearrangement, or clustering of pores or particles.
- Dimensionless Microstructural Pathways can be used to compare simulated microstructures and experimentally observed microstructures independent of scale and time. These parameters are based on microstructural averages to characterize the evolution of the relationship between pores and grains or particles with solid volume fraction.
- An Information Entropy based method of three dimensional size distribution provides a reliable means of characterizing the grain or particle size evolution during densification for comparison with computer simulations.
- Tessellation methods are used to evaluate the immediate and local environments of second phase particles.

3.0 HYPOTHESIS

It is proposed that there is a higher hidden scale, a meso-scale, on which the microstructural features relevant to sintering and creep behavior of porous materials are observable. **This scale is associated with the local packing of powder particles and will be sensitive to processing variables**. Observations of the evolution of the microstructures of porous materials derived from powders reveals the presence of an aggregated or clustered structure. However, the evolution of porous microstructures are generally characterized by average parameters, combinations of average parameters, or more rarely size distributions of particles, grains, or pores. Microstructural analyses designed to quantify these parameters are carried out at magnifications necessary to accurately measure the parameter of interest (number of intercepts, grain cross-section area, etc.). This focused approach is thought to obscure the relevant microstructural features of clusters of grains or particles. It is hypothesized that during densification these hidden features, clusters of grains or particles, appear to grow at the expense of lower density regions of the microstructure.

The clusters of grains or particles may have much higher solid volume fractions within their boundaries than the microstructural average resulting in local microstructural arrangements that require coordinated rearrangement to achieve further densification. This coordinated rearrangement will be inhibited at higher solid volume fractions. Thus, the preponderance of deformation of compacts will be restricted to lower solid volume fractions. The identification of the cluster structure of the primary phase of a microstructure may be difficult. In the case of a porous material, the primary phase is the solid volume and the porosity is the minor phase. Since the boundaries of the pore structure are defined by the solid-vapor interface, the rearrangement of the clusters of particles or grains will have a direct effect on the structure of the porosity.

Therefore, the alternative to identifying the cluster of grains or particles is to identify regions of porosity associated with the coordinated rearrangement of clusters.

The evolution of the cluster structure may influence the densification and creep behavior as well as the final microstructure of a porous material. The relationship of a quantitative description of this evolution with processing variables may provide insight into the influence of this structure on densification behavior, and final microstructure thereby, providing a means of microstructural design to obtain desirable properties such as improved creep resistance. Information concerning the hidden scale could also be used in phenomenological models of sintering used to predict the evolution of properties of porous materials. Current models use simulated microstructures of dense random packing of spheres or ordered arrays of spheres or polyhedra to reduce the representative element to one grain and its attendant porosity. Inherent in these models is the assumption that densification occurs only by a process involving contact flattening. Except for specially prepared materials these models bear little or no resemblance to experimentally observed microstructures. Microstructural models that better represent experimental microstructures must be developed. To evaluate or aid in the design of these new models the evolution of the average parameters, size distributions, and cluster structure of simulated and experimental microstructures must be explored. Validated models can be used to create new representative volume elements (RVE) for use in finite element method simulations of components to predict local evolutions of the microstructure and properties.

4.0 OBJECTIVES

The objective of this research is to develop a quantitative method of mesoscale microstructural characterization of porous materials derived from powders which is directly sensitive to powder processing variables and will also provide a basis of comparing simulated and experimental microstructures. In particular, the mesoscale characteristics of the microstructure of slipcast alumina in dispersed and flocculated conditions, sintered at 1350°C, are studied to determine the effect of flocculation on the evolution of the microstructure and densification behavior of alumina in the absence of significant coarsening. The method of characterization will involve the use of Dirichlet tessellation as a means of segmenting materialographic sections of the microstructure into regions associated with individual features of the microstructure. Distributions and the correlations between feature (pores or grains) parameters (size, shape, etc.) and tessellation cell properties (size, shape, solid volume fraction, etc.) will be explored to develop a mesoscale description of densification.

5.0 EXPERIMENTAL APPROACH

This section contains details concerning the experimental procedures and software development performed in this work.

5.1 ALUMINA SINTERING EXPERIMENTS

A set of alumina (α-Al_2O_3: Premalox, ALCOA) samples sintered at 1350ºC were prepared by slip casting in a well dispersed or flocculated condition. The details of the processing steps are listed below:

1) Suspensions of alumina (Premalox) powder in de-ionized water were prepared by mixing alumina into the water while being stirred by a magnetic stirrer.
2) An ultrasonic processor (Sonicator XL Ultrasonic Processor, Heat Systems, Inc.) was used to break down soft agglomerates.
3) Flocculation and dispersion: either a or b but not both were used on each slip.
    a. Flocculation was enhanced by adjusting the pH of the suspension to pH9 by adding ammonium hydroxide while magnetically stirring. Each suspension was pored into a 1000ml Nalgene bottle and rolled for 24 hours.
    b. Dispersion was enhanced by the addition of a polyelectrolyte (Darvan C, Vanderbilt: 1.7ml per 50g alumina) while magnetically stirring. Each suspension

was pored into a 1000ml Nalgene bottle and rolled for 24 hours. The ultrasonic processor was again used to break-up agglomerates.

4) Particle size analysis of the slip was performed using a CAPA-300 Centrifugal Automatic Particle Size Analyzer (Horiba Ltd.).

5) The suspensions were heated and stirred until the solid volume fraction of the slip (volume of alumina / total volume) was about 0.3.

6) The slip was poured into plaster-of-paris molds and allowed to air dry forming disk shaped casts.

7) The green casts were heat treated in an alumina crucible using a Lindberg Model 51314 box furnace at a temperature of 1350ºC for 0.1 hours. A heating ramp rate of 5ºC per minute and a maximum cooling rate of 10ºC per minute were used.

8) The disks were sectioned in roughly cubical shaped pieces using a Buehler Isocut Plus precision saw with a diamond wafering blade and water cooled.

9) The sections of the disks were subjected to additional heat treatments. Individual samples were held at 1350ºC for each of the following times: 0.1, 0.2, 0.6, 1.1, 5.1, 10.1, 15.1, 30.1, and 60.1 hours. A heating ramp rate of 5ºC per minute and a maximum cooling rate of 10ºC per minute were used.

10) Each sample was sectioned again into two approximately equally sized pieces.

11) The samples were vacuum impregnated with an epoxy (Epo-Thin, Buehler Ltd.) to prevent pull-out during materialographic preparation.

12) The face of the section that was in the interior of the sample after step 6 were prepared for materialographic analysis using standard grinding and polishing methods on a Buehler Ecomet 4 Grinder-Polisher with Automet 2 Power Head with Metadi II Diamond Polishing Compound (Buehler Ltd.: 45, 15, 6, and 1μm).

13) The polished samples were thermally etched. They were held at 1325ºC for 0.3 hours using the same ramp rates as steps 4 and 6 to provide grain boundary relief.

5.2 MICROSCOPY

The majority of this work involves the microstructural analysis of materialographic sections of alumina. The following steps were used to obtain the necessary micrographs and subsequent digital images:

1) The etched samples were coated with palladium (approximately 5nm thick) by sputtering to prevent charging during electron imaging in a scanning electron microscope.

2) A series of SEM micrographs for microstructural analysis were obtained using the back-scattered electron imaging mode of a Philips XL30 FEG SEM at an acceleration voltage of 15kV and magnifications appropriate to the type of analysis (grain size, pore size, tessellation) to be performed. Magnifications were selected to provide a balance between the number of features in an image and the minimum measurable size.

    a. Magnifications used for pore and grain size analysis were 10,000x, 15,000x and 20,000x with a digital image size of 712 (width) by 484 (height) pixels.

    b. Magnifications used for tessellation were 2,500x with a digital image size of 1424 (width) by 968 (height) pixels or 5,000x with a digital image size of 712 (width) by 484 (height) pixels.

3) Digital image processing was performed using either ScionImage (Scion Corp.: NIH Image, National Institute of Health) or software written specifically for this work. (User experience and patience can be important factors in obtaining reliable results.)

    a. Several image processing steps were used to prepare images for grain size analysis. A macro was written for ScionImage to identify grain boundaries using a combination of smoothing, thresholding, background subtraction, and image math operations. The technique requires the user to visually inspect and manually correct the images after running the macro to complete or add missing boundaries and remove incorrectly identified boundaries. During this process it is also necessary to identify grains that are below the plane of polish (located in a pore that was sectioned) and remove them from the image. The grain boundary image

must be compared with the original image to verify that the boundaries have been satisfactorily identified.

b. The processed images with completed grain boundaries also include pore sections, including those located on grain boundaries. The grain boundary images are processed using dilation, erosion, opening, and closing operations to remove the boundaries without removing the pore sections. The pore section image must be compared with the original image to verify that the pore sections have been satisfactorily identified.

c. The digital micrographs acquired for tessellation were saved at the magnifications and image sizes described in 2)b. The combinations provide the same area per pixel (0.00135μm^2 per pixel) but, allow larger areas to be imaged when pore section spacing increases relative to image size at higher densities. The images necessary for tessellation were processed primarily with the Tessellator program developed for this work. Additional processing was performed using ScionImage when practical. The primary image processing steps used in creating the pore section images were the application of a median filter and thresholding. Tessellation and analysis were performed using the Tessellator program.

5.3 AVERAGE MICROSTRUCTURAL PARAMETERS

5.3.1 Solid Volume Fraction Measurements

The solid volume fraction for each of the samples investigated was determined using two methods. The first is the Archimedes method in which the mass of each sample is measured while the sample is dry, immersed in water, and saturated with water. The solid volume fraction is simply the solid volume (dry mass / theoretical material density) divided by the volume of water displaced by the sample ((saturated mass – immersed mass) / theoretical density of water). The second measurement uses the result from Stereology that the solid volume fraction is equal to the area fraction of solid on a materialographic section. Area fractions were measured using digital micrographs processed using ScionImage to create binary (black and white) images of the pore sections only as described in section 5.2 . The values obtained by the Archimedes method are used to verify that a statistically significant number of micrographs are used for further analysis.

5.3.2 Densification Rate Calculation

A property of interest in this research is the densification rate of the material during sintering. In many cases a logarithmic function adequately fits the densification data, density versus time, Equation 18, to the relative density versus time plot. The relative density or equivalently the solid volume fraction is represented by ρ, 'a' is the rate constant, 't' is time in hours, and ρ_1 is the relative density at time equal to 1 hour. The densification rate is obtained by taking the derivative of Equation 18 with respect to time resulting in Equation 19. The densification rate is proportional to 'a' and inversely proportional to time. The densification rate can also be put in terms of the relative density by solving Equation 18 for 't' and substitution into

Equation 19 resulting in Equation 20. The densification rate is still proportional to 'a'. However, the rate is also proportional to the exponential of $\rho_1 - \rho$ divided by 'a'.

Equation 18: $\rho = a \bullet \ln(t) + \rho_1$

Equation 19: $\frac{d\rho}{dt} = \frac{a}{t}$

Equation 20: $\frac{d\rho}{dt} = a \bullet \exp\left(\frac{\rho_1 - \rho}{a}\right)$

5.3.3 Surface Area per Unit Volume Measurement

Surface area per unit volume measurements were performed using the Stereology method of counting intersection points of parallel test lines. The surface area per unit volume is equal to two times the number of points of intersection with the pore-grain (solid-vapor interface) boundaries and/or the grain-grain boundaries (solid-solid interface) divided by the total length of test line. Solid-vapor interfaces are considered to be one surface while solid-solid interfaces are one surface shared by two grains. The values of surface area per unit volume were also used to calculate the dimensionless ratios of surface area (Ψ), intercept length (Λ), and pore spacing-grain intercept (Σ) to compare with the microstructural pathways previously examined.

5.4 GRAIN-SCALE MICROSTRUCTURAL PARAMETERS

5.4.1 Grain / Particle Size Distribution Analysis

The grain or particle size distribution of each sample was determined using the information entropy based method of particle size unfolding on the grain section area data obtained from the processed grain boundary images. The unfolding method is a modified form of

the inverse methods advanced by Saltykov without the arbitrary restrictions on size class boundaries. The class boundaries are determined by maximizing the relative information entropy, which determines the most efficient use of available information. Maximum entropy occurs when an event, the size of a particle, has equal probability of being in any class. This allows the particle size distribution to dictate the proper boundaries rather than an arbitrary selection for calculation convenience. The cross-section area distribution is measured using binary images of grain boundary reconstructions. A large number of cross-sections were measured for each sample. The minimum number of grain sections used in an analysis was about 1000.

5.4.2 Simulation

The analysis of grain size distributions from planar materialographic sections requires some assumptions. The morphology of the grain or particle can have a dramatic impact on the resulting 'true' grain size distribution. In the case of spherical particles, there exists analytical solutions for the distributions of particle section parameters such as the diameter of the circular section. However, typical grains are not spherical. To obtain distributions of section parameters for various grain morphologies, a computer simulation of the random sectioning of user or randomly generated convex particles was developed. The simulation of the sectioning of particles was performed using a Monte Carlo simulation. Convex polyhedra are either user defined or randomly generated. The polyhedron is rotated about the origin in the 3-D simulation space by selecting two angles and one cosine by random number generation. Once a new orientation is selected, the position of a sectioning plane in the 'z' direction of the simulation space is selected using random numbers. The intersection of the sectioning plane and the polydron's faces are determined using analytic geometry. The section is constructed from the intersections (lines) and all specified geometric parameters are calculated. The process is repeated until the user set number of sections has been analyzed.

Prior to execution of the simulation, the number of classes or bins for the resulting distributions must be specified. Distributions based on the set number of classes are outputs from the program rather than a complete list of all sectionings. In many cases the number of sections taken was 1,000,000. Saving the results of each sectioning would result in very large data files.

The distribution results of previous studies found in the literature for various particle morphologies were compared for verification. The grain size analysis was performed using various convex polyhedra as the assumed morphology. In addition to spheres the polyhedra used for the analysis included: cubes, truncated cubes, hexagonal prisms, truncated tetrahedra, and tetrakaidecahedra (truncated octahedra). An analysis of the effect of shape assumption on the resulting grain size distributions is examined in relationship to the parameters of the distributions.

5.5 TESSELLATION AND IMAGE ANALYSIS

Commercially and freely available software was not capable or too costly to perform the tessellation procedures necessary for the processing of SEM micrographs used in this research. Therefore, an image processing program was developed for this work to carry out the various non-standard methods used for this research. In some cases the original images were 'pre-processed' using other software such as ScionImage. The tessellation program was developed to be a supplement to existing software and not a replacement. The tessellation of the pores is accomplished by first color-coding each pore by its number which is assigned by the top-leftmost pixel associated with the pore in the digital micrograph. The color-coded pores are then dilated until all pixels in the image are associated with one of the pore tessellation cells. All cells that intersect the edge of the image are discarded for the analysis. Additionally, a guard frame can be employed to reduce the error associated with excluding larger cell sections. For example, cells that do not have their top-leftmost pixel contained within the guard frame region can be discarded. Thousands of pore sections were measured and tessellated for each of the casting conditions and times at temperature to obtain reliable statistics.

6.0 RESULTS

Several microstructural parameters were examined during this research to characterize the evolution of the microstructure of porous materials processed under different casting conditions during densification. The analysis began with densification kinetics, density with time and densification rate with time. The densification rate was then plotted as a function of density instead of time. This is appropriate for this study because it was determined that the solid-vapor interface (free surface) per unit volume was equal for dispersed and flocculated alumina at similar densities. The driving force for densification is typically associated the reduction in free energy associated with the reduction in surface area. Microstructural parameters were then compared at similar densities to determine if the effect of casting condition, dispersed or flocculated, on the densification behavior could be explained by changes in the microstructure. Stereological parameters are microstructural averages and were found to be incapable of identifying differences between the dispersed and flocculated microstructures throughout the range of densification. Therefore, the next step was to examine the evolution of distributions of feature parameters such as the evolution of the grain size distribution. The distributions were similar at similar densities due to the lack of coarsening at the low sintering temperature. The only distribution that revealed a difference between the dispersed and flocculated alumina microstructures at similar densities was the distribution in pore section area. However, this alone could not explain the differences in densification behavior due to the fact that the difference between the distributions was the smallest at the density at which the difference between densification rates was the highest.

A large number of distributions in microstructure feature parameters and tessellated microstructure feature parameters were develop and examined. These parameters include shape factors, area measurements, and derived parameters. An example of a derived parameter is the

cell solid area fraction. Also, parameters that characterize the immediate and local environments of the pore sections were developed and analyzed. Immediate environment is defined as the region contained within the boundaries of a pore's tessellation cell. Immediate environment parameters include the cell area, cell shape factor and the cell solid area fraction. Local environment is defined as the region associated with nearest neighbor cells. Local environment parameters include the cell 2-D coordination number, the local mean pore section area, and the local mean solid area fraction. In many cases the distributions in these parameters were similar at similar densities. However, in many cases the cell maps were able to identify differences in the microstructures by the correlation between parameters.

Throughout the result section, the terms low, intermediate and high solid volume fraction refer to 0.82, 0.90 and 0.96 solid volume fractions, respectively. The terms density, relative density, and solid volume fraction may be used interchangeably throughout this document because in the case of single-phase isotropic materials such as the alumina studied in this research relative density and solid volume fraction are equal and the density is always proportional to the relative density.

6.1 STEREOLOGICAL MEASUREMENTS AND DIMENSIONLESS PARAMETERS

6.1.1 Densification

The time evolution of the solid volume fraction or relative density of alumina sintered at 1350ºC is shown in **Figure 21**. Two casting conditions were used to prepare the samples for firing. The first condition was dispersed in which a polyelectrolyte (Darvan C, Vanderbilt) was used to prevent agglomeration of the particles in suspension before casting. The second condition was flocculation, the pH level of the deionized water used in casting was adjusted to pH9 using ammonium hydroxide to promote the formation of agglomerates. There is a significant difference between the initial solid volume fractions of the two conditions, 0.82 for dispersed and

0.75 for flocculated. However, both attain an apparent final solid volume fraction of 0.96 at approximately 15 hours of time at temperature (**Figure 21**). The densification rate in the intermediate stage was calculated by fitting a logarithmic function, Equation 18, to the relative density versus time plot. The fit parameter, 'a' equals 0.0285 and 0.0386 for dispersed and flocculated alumina, respectively. The fit parameter, the relative density at 1 hour, ρ_1, equals 0.890 and 0.842 for dispersed and flocculated alumina, respectively (**Figure 21**).

The densification rate is proportional to 'a' and inversely proportional to time (Equation 19). Therefore, at a given time within the range over which Equation 18 is valid; the densification rate for the flocculated alumina is approximately 25% higher than the rate for dispersed alumina. The densification rate in terms of the relative density is given by Equation 20. The densification rate is still proportional to 'a'. However, the rate is also proportional to the exponential of $\rho_1 - \rho$ divided by 'a'. Therefore, for solid volume fractions within the valid range of Equation 18; the densification rate of the dispersed alumina is greater than that of flocculated Al_2O_3 at 1350ºC (Figure 22). The difference in densification rates combined with the use of similar processing conditions suggests an influence of the dispersion condition on the densification behavior of Premalox powder.

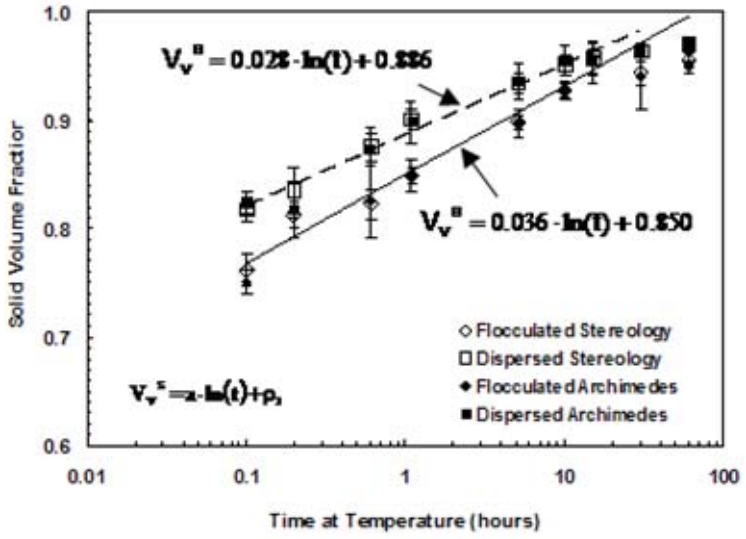

Figure 21: Although the initial densities are significantly different, dispersed and flocculated reach the final density at approximately the same sintering time. The densification curve during the intermediate stage of sintering was fitted to the logarithmic function where ρ is relative density or solid volume, ρ_1 is the solid volume fraction at time equal to 1 hour, t is time in hours, and a is the rate constant.

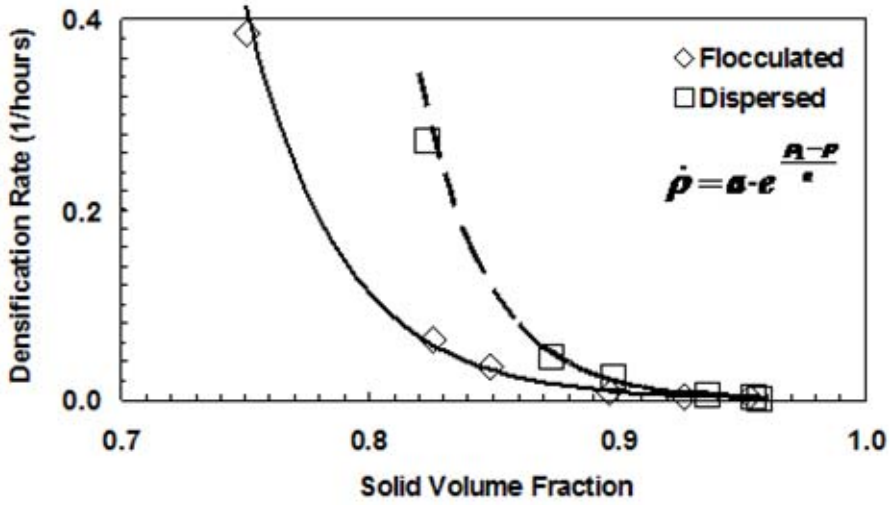

Figure 22: Although the densification rate is higher for the flocculated alumina at any time during the intermediate stage of sintering, the densification rate is higher in dispersed alumina at any density within the range of the intermediate stage of sintering.

6.1.2 Surface Area per Unit Volume and Dimensionless Ratios

Several microstructural measurements were performed to determine if the microstructural evolution of Al_2O_3 sintered at 1350°C is affected by the casting conditions. The stereological measurement of the solid-solid (grain to grain or particle to particle interfaces) surface area to volume ratio and solid-vapor (grain to pore or particle to pore interfaces) surface area to volume ratio were made using standard methods of point counting. The evolution of the surface area per unit volume is shown in **Figure 23**. At most solid volume fractions the values for dispersed and flocculated alumina are similar. There is a linearly decrease in the solid-vapor surface area per unit volume for both dispersed and flocculated alumina with increasing solid volume fraction. This relationship is seen for a wide variety of ceramics and powder metals[50]. The solid-solid surface area per unit volume remains relatively constant until a solid volume fraction of approximately 0.95 but, then decreases rapidly.

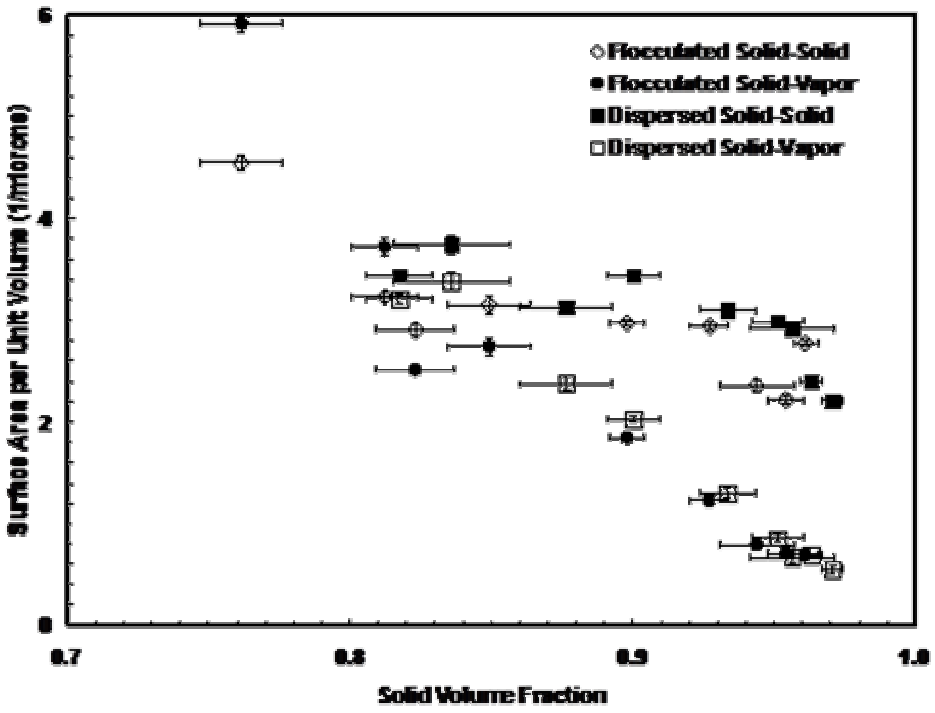

Figure 23: The dispersed and flocculated evolutions of the surface area per unit volume for solid-solid and solid-vapor interfaces with solid volume fraction are similar.

The surface area per unit volume measurements and the measure of the solid volume fraction were used to calculate the dimensionless microstructure parameters, solid-solid surface area to solid-vapor surface area ratio and the mean grain intercept to mean pore intercept ratio. The surface area ratio for Premalox sintered at 1350ºC is plotted along with data for Premalox sintered at 1375ºC[170], Nanophase[171] alumina sintered at 1375ºC, HIPed alloy 625[170], and two of the phenomenological sintering model results[120,121] in **Figure 24**. The simple cubic model is shown through its maximum valid solid volume fraction, the solid volume fraction at which contact areas intersect, and the final stage model is shown through its entire range of applicability, the solid volume fraction at which pores contact each other to full density (approaches infinity at full density). Except for the early stages of sintering the surface area ratio for the sintered ceramics is considerably higher than the model predictions and the values for the HIPed nickel–based alloy 625 are lower than the prediction. This shows that these pathways are insensitive to differences in processing conditions and a universal pathway is not suitable for showing the effects of processing conditions on the evolution of the microstructure.

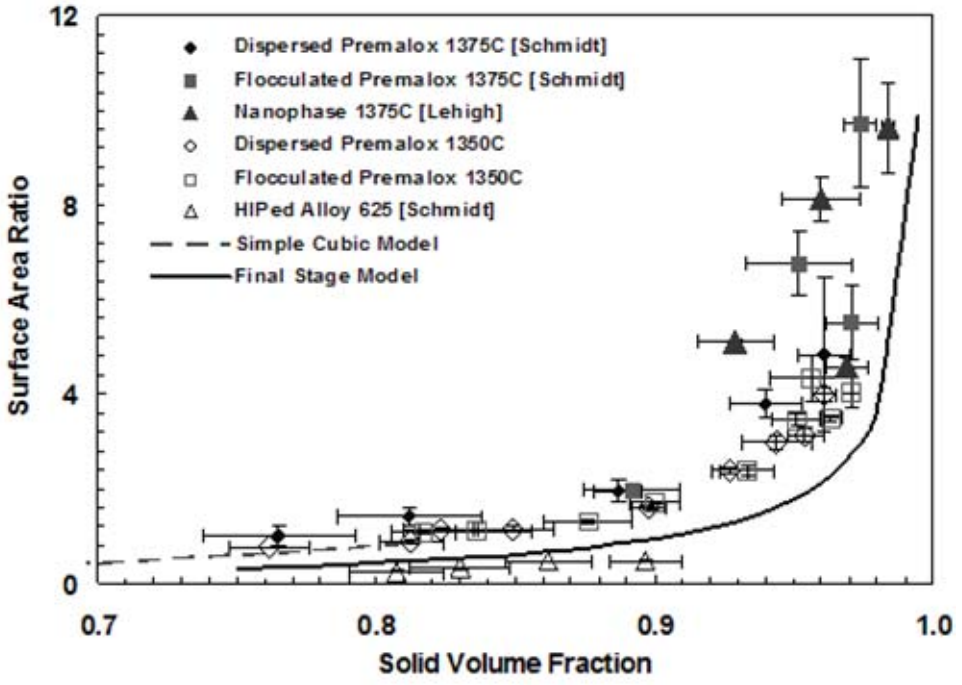

Figure 24: Surface area ratio versus solid volume fraction for various materials and processing conditions along with two model predictions.

Experimental values of the mean pore intercept length calculated from the solid-vapor surface area per unit volume and the solid volume fraction (**Figure 25**) for the sintered Premalox samples are relatively constant (~ 0.2μm) throughout the solid volume fraction range. However, the phenomenological models of sintering assume that the geometry of the sintering models remains constant through their valid densification ranges. Therefore, contrary to experiment the mean pore intercept for the sintering models will decrease with increasing solid volume fraction. The relatively constant mean pore size and the increasing values of the intercept ratio with increasing solid volume fraction indicates that the change in solid volume fraction must be accompanied by a change in the pore geometry, an increase in pore spacing (**Figure 26**), or a combination of both. The increase in the intercept ratio for the sintering models with increasing solid volume fraction is due to the assumption of constant grain size throughout the valid solid volume fraction range. This also is contrary to experimentally observed results.

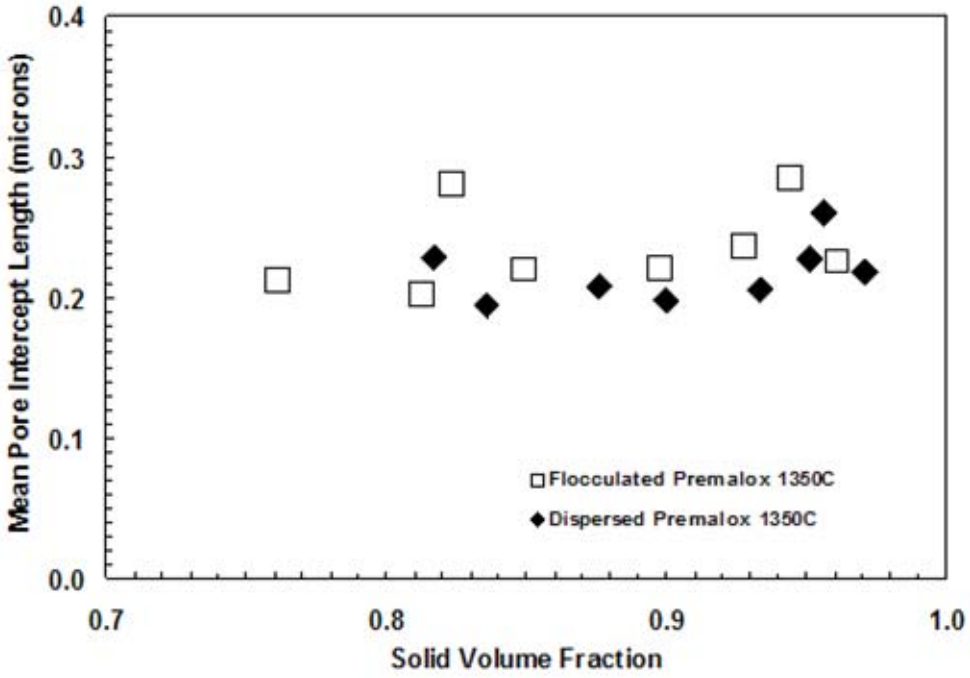

Figure 25: Mean pore intercept length for alumina sintered at 1350ºC. The mean remains approximately constant throughout the density range.

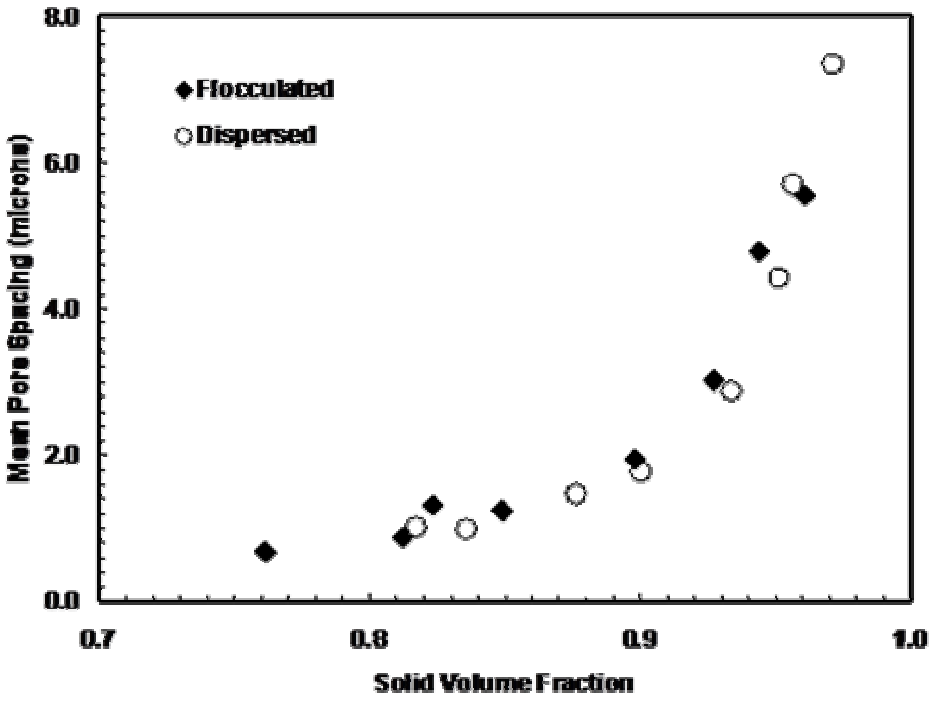

Figure 26: The dispersed and flocculated evolutions of mean pore spacing with solid volume fraction are virtually identical.

Another parameter calculated from the surface area per unit volume and the solid volume fraction data is the mean grain intercept. The results are presented in **Figure 27**. The dispersed and flocculated alumina evolutions with solid volume fraction are similar. The mean grain intercept length increased from about 0.2μm to 0.8μm as the solid volume fraction increases from 0.75 to 0.96.

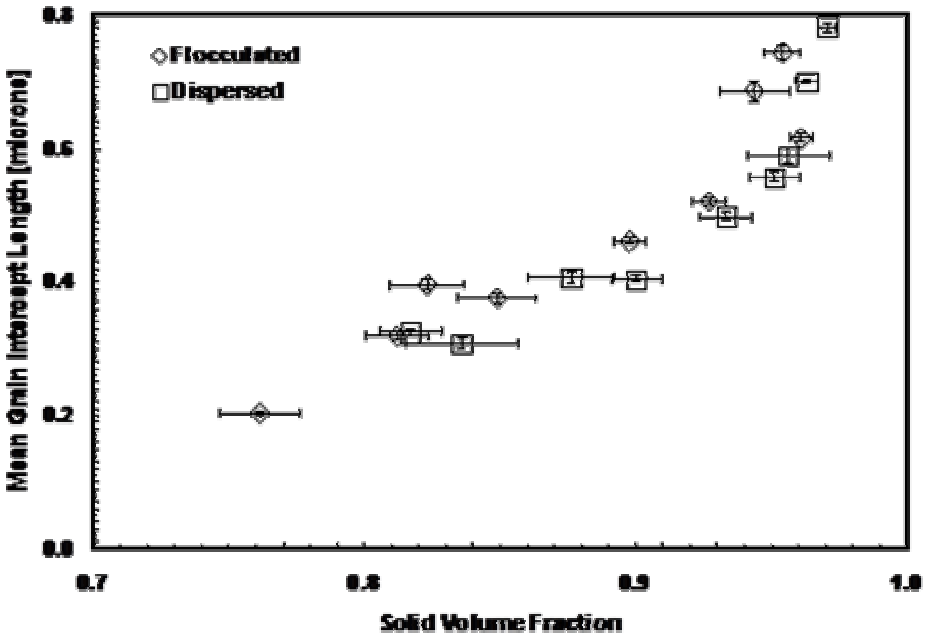

Figure 27: The dispersed and flocculated alumina evolutions with solid volume fraction of mean grain intercept follow similar paths.

The mean grain to mean pore intercept ratio given in **Figure 28** shows an overestimation of the models beyond a volume fraction of 0.8. The results of both the surface area ratio and the intercept ratio indicate that the pores are too large relative to the grains in the models or that the grains are too small relative to the pores. Smaller grains of the same shape have a larger surface area per unit volume due to the inverse relationship between the surface to volume ratio and the 'size' of a grain.

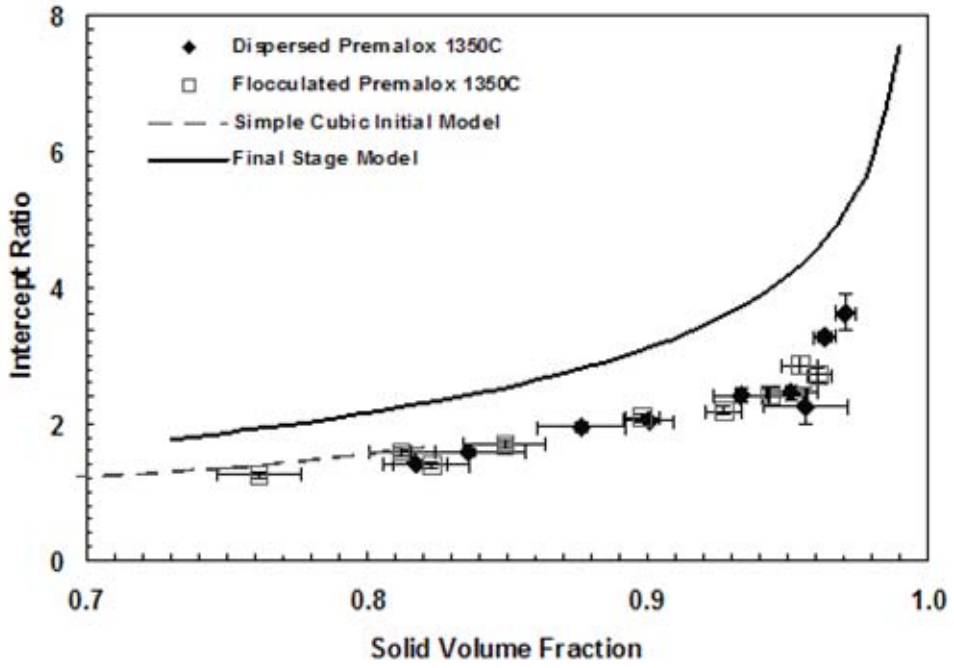

Figure 28: Grain – pore intercept ratio versus solid volume fraction for alumina sintered at 1350ºC with model predictions.

Another dimensionless parameter based on stereological data examined is the mean pore spacing to mean grain intercept length ratio. Trends in the evolution of this parameter with density may indicate the degree to which pore spacing is controlled by grain growth or alternatively the degree to which grain growth is controlled by pore spacing. The results shown in Figure 29 suggest that the mean pore spacing is not controlled by grain growth alone. Pore removal may also be occurring. However, it does not rule out the possibility of the control of grain growth by pore spacing.

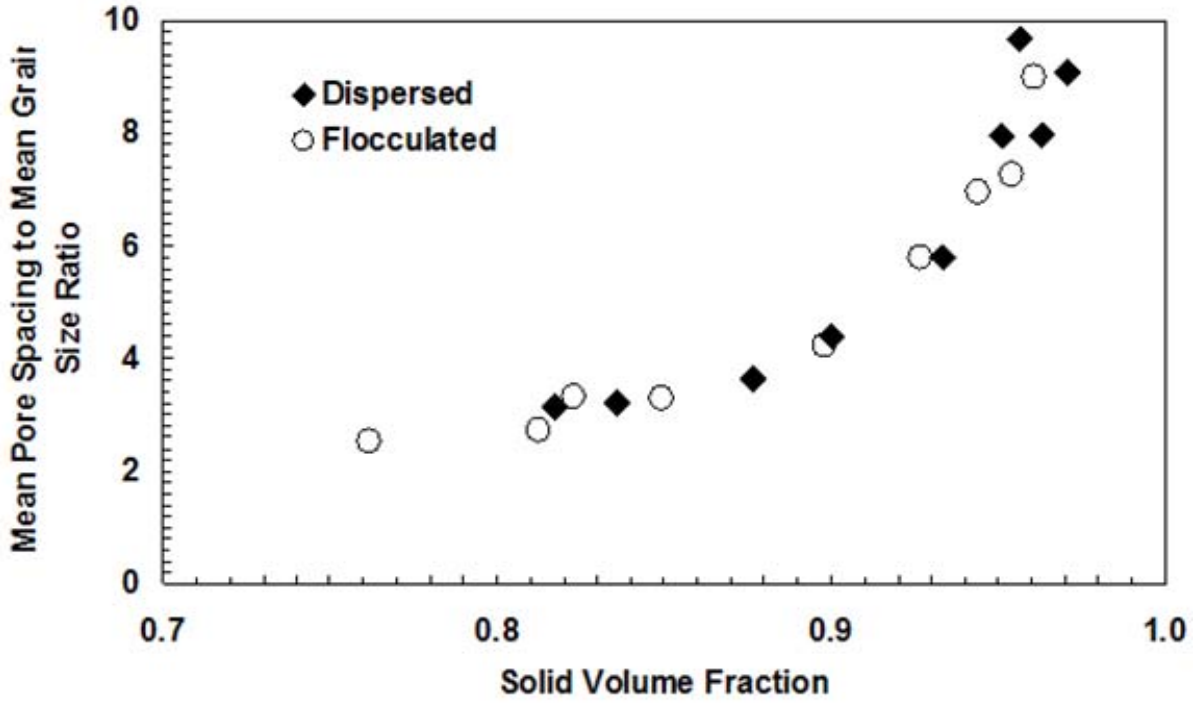

Figure 29: The dimensionless microstructural pathway, mean pore spacing to mean grain intercept ratio suggests that pore spacing may only be partly attributed to grain growth.

6.1.3 Comparison of Densification Simulation with Experiment

One of the goals of this research is to provide a basis for comparing simulated microstructures with experimental microstructures. The packing of particles has been simulated by many researchers in materials science and other fields. **Figure 30** is an illustration of one such simulation[172]. The illustration of the arrangement of particles in the left portion of **Figure 30** is of the initial particle packing. The initial size distribution of the 1000 particles was constructed to be lognormal with a standard deviation of 1.25 or a coefficient of variation of 0.225 based on experimental results of this study. Densification was simulated by increasing the radius of all particles by a given fraction per step. Densification is attained by contact flattening only. The size of each particle is scaled to maintain a constant total solid volume. In effect the particle centers are drawn closer together and the material from the regions of sphere overlap is redistributed to the surface of the particles. The arrangement on the right side of **Figure 30** is the same packing after an increase in radii of 61% to simulate densification. **Figure 31** shows a

section through the packings at a height half way between the top and bottom of the packings. Although the particles in the simulation were randomly positioned and selected at random from a lognormal distribution there appears to be some clustering of particles. Unfortunately, there is an insufficient number of particles to quantify the clustering. Theoretical descriptions of clustering will probably require thousands of grains.

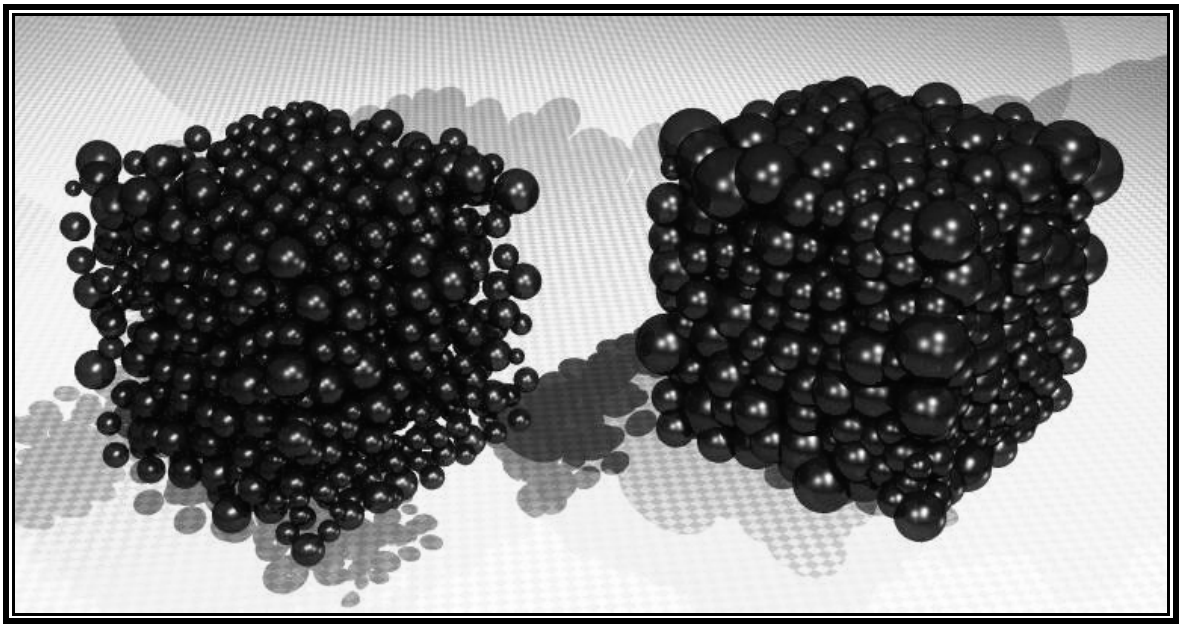

Figure 30: Illustration of the lognormal distribution simulation by Kumar Krishnan. On the left is the original packing arrangement. On the right is the same packing arrangement after a relative increase in particle radius of 61%.

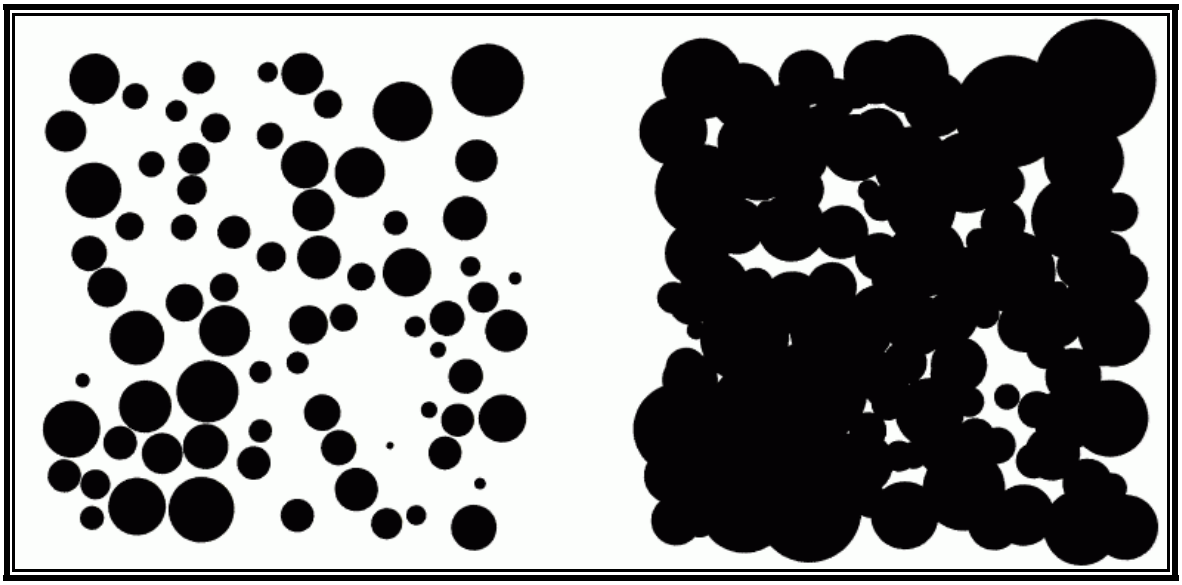

Figure 31: Sections through the arrangements of Figure 30 at half the height of the compact. Particle centers are fixed throughout the simulation. There is an apparent clustering of particles in the sections.

The dimensionless microstructure parameters, solid volume fraction, surface area ratio, and intercept ratio were calculated for each step of the simulation. The results are plotted in **Figure 32** and **Figure 33** with the alumina samples sintered at 1350ºC experimental data and the geometric model predictions. Also included are results of another simulation by Krishnan using a uniform distribution of particle size[172]. There is excellent agreement between the simulations and the alumina results despite the obvious difference in particle morphologies (spheres vs. equiaxed grains) and the lack of particle rearrangement in the simulation.

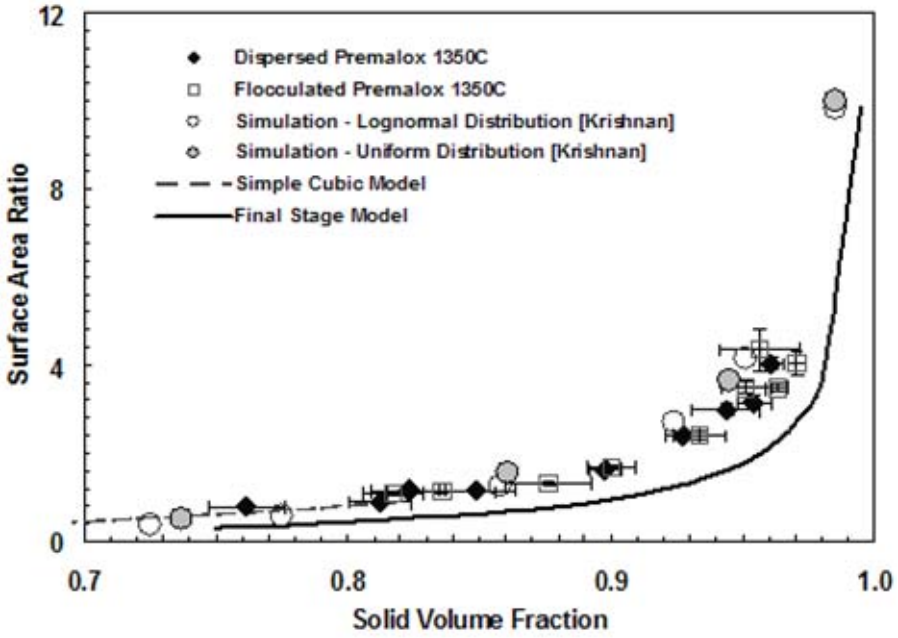

Figure 32: Comparison of the dimensionless surface area ratio for alumina (Premalox) sintered at 1350ºC with simulations of two different distributions of randomly packed spheres shows excellent agreement with the alumina results.

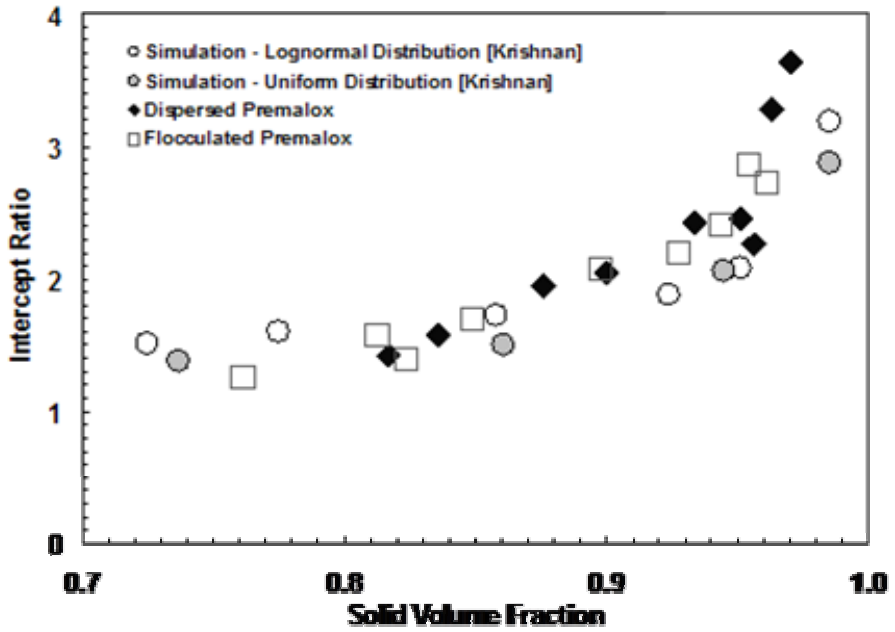

Figure 33: The dimensionless intercept ratio also shows excellent agreement with the results of the random arrangement of spheres simulations with both lognormal and uniform particle size distributions.

6.2 GRAIN SIZE EVOLUTION

6.2.1 Grain Size Distributions

If average microstructural parameters or their ratios are insufficient to characterize differences in the microstructure of sintered materials under different processing conditions the next logical step is to determine distributions of microstructure parameters. **Figure 34** shows the 'true' (three dimensional) grain size distribution for dispersed Al_2O_3 sintered at 1350ºC for 5.1 hours using an inverse method with a sphere as the assumed shape. In many cases the method results in negative frequencies if too many classes (bins) are used. In **Figure 34** only seven classes with the method using classes restricted to equal increments in grain diameter and only

three classes for the case of equal increments of area were possible before encountering negative frequencies. There is an accumulation of error in the smaller unfolded classes due to the inversion of the probability matrix. However, the main cause of the negative frequencies is the arbitrary restriction of class boundaries.

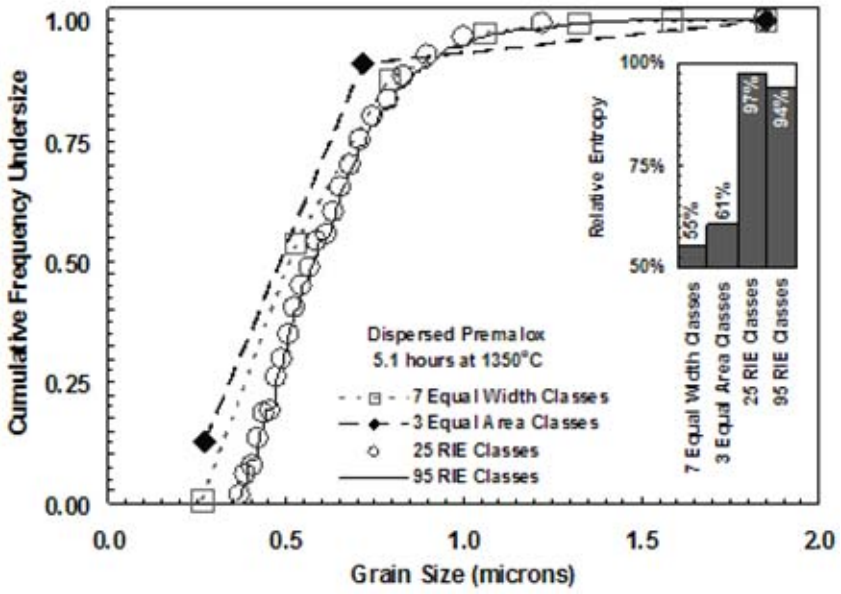

Figure 34: Grain size cumulative frequency undersize by number for alumina sintered at 1350ºC for 5.1 hours. Only 7 classes were possible using Saltykov equal area classes and only 3 for the equal area classes before negative frequencies occurred. The inset shows the relative information entropy for each result.

A modified form of the inverse method was developed in which class boundaries were not restricted by arbitrary rules. Instead, class boundaries are determined by the size distribution. Boundaries are positioned in a manner that maximizes the relative information entropy, RIE, of the distribution. In the 5.1 hour dispersed alumina example as many as 95 classes were possible without encountering a negative frequency. Approximately 1400 cross-section areas were measured from SEM micrographs using ScionImage for this sample. The average number of sections measured for all samples was more than 1000 per sample. The average number of grains per class in the example of **Figure 34** using 95 classes is only 15. A few grains in the wrong class could have a significant effect on the neighboring classes and the overall distribution. A distribution using 25 RIE based classes is also shown in **Figure 34**. With an average number of

grains per class of 56 the distribution using 25 classes is less susceptible to error than the distribution with 95 classes. Also, the RIE for 25 classes was slightly higher (97%) than that for 95 classes (94%). The relative information entropy values for the Saltykov methods were considerably lower with 55% for the seven class distribution and 61% for the three class distribution. This indicates that the available information is not being used effectively in the Saltykov methods.

6.2.2 Distribution Parameters

In order to characterize and compare the evolution of the grain size distributions it is necessary to use distribution parameters. **Figure 35** shows the fitting of three distribution types, lognormal, Weibull, and gamma, to the RIE based grain size distribution for the dispersed Premalox sample fired for 5.1 hours at 1350ºC. Standard techniques of chi-squared and Pearson correlation coefficients were used to determine the best fit. In most cases the lognormal distribution was the best or second best fitting distribution. Therefore, the lognormal mean (median) and the coefficient of variation were used to characterize the evolution of the distributions.

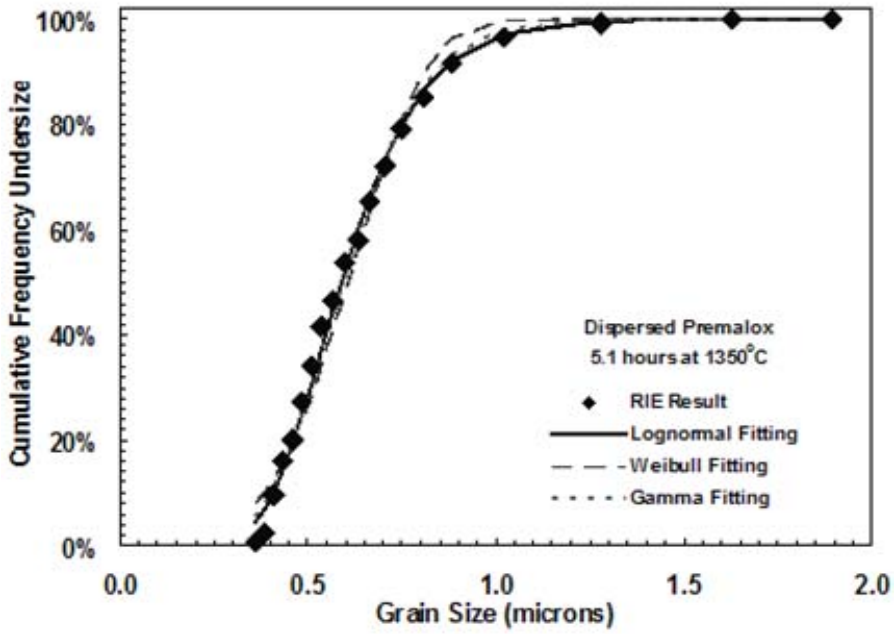

Figure 35: Lognormal, Weibull, Gamma distribution fits to the above grain size distribution. In this case best fits are the Lognormal and Gamma distributions.

6.2.3 Shape Assumption

The average microstructural parameters of surface area per unit volume and mean intercept lengths are not shape dependent. However, the unfolding method results depend on the assumed shape of the grain or particle. Probability distributions for cross-section areas were obtained using a computer simulation developed during this study and designed to randomly section individual polyhedra. The distributions obtained from the computer simulation were compared with results found in the literature from other simulations and analytical solutions as a method of verifying the software. Results for several convex polyhedra were compared with those of Wasén and Warren[137,138,149]. The results were found to be in good agreement with distributions of 50 classes. Wasén and Warren performed only 10,000 sectioning operations to obtain their results due to limited computing capability. Distributions used in this work were generated using a minimum of 1,000,000 sectioning operations.

The unfolded grain size distributions obtained by using spheres, truncated cubes, hexagonal prisms with an aspect ratio of 0.5, cubes, tetrakaidecahedra, and truncated tetrahedra for the dispersed Premalox sample fired for 60.1 hours at 1350ºC are given in **Figure 36**. There is a noticeable difference between the resulting distributions. The distribution using spheres is shifted to smaller grain sizes compared with the polyhedra. As expected the tetrakaidecahedra result is closest to the spheres result because the fraction of solid volume associated with a circumscribed sphere is higher for this shape. The RIE values for each distribution are given in **Figure 37**. The RIE values for the more equiaxed shapes, spheres, tetrakaidecahedra, and truncated tetrahedra are higher than the others. This is expected because the grain sections in the materialographic sections appear to be relatively equiaxed.

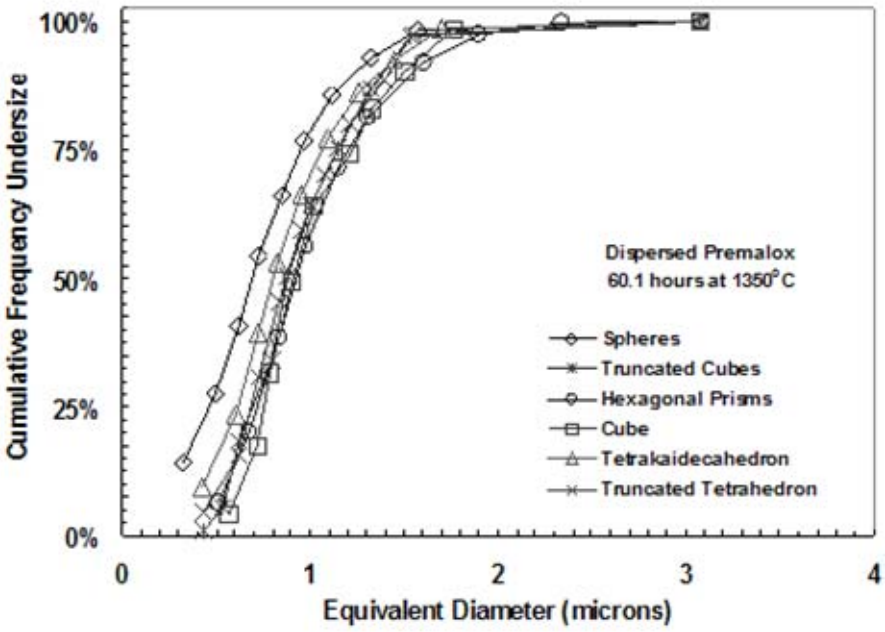

Figure 36: Grain size distribution for alumina sintered for 60.1 hours at 1350ºC using different assumed shape and the corresponding entropy values. The difference in probability distributions for cross-section areas results in differences in the unfolded distribution of grain size.

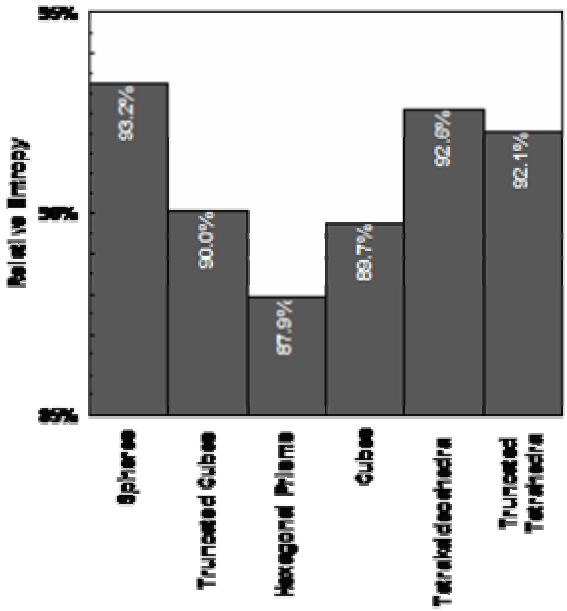

Figure 37: The relative information entropies are given for the distributions in Figure 36. The more equiaxed shapes have higher entropy values.

The parameters of the distributions obtained using various shapes are given in **Figure 38** and **Figure 39** for the dispersed Premalox samples sintered for 0.1 hours, 5.1 hours, and 60.1 hours at 1350°C. Although there can be significant differences in the magnitudes of the parameters for different shapes the relative changes in parameters shows little dependence on shape. While there may be some argument as to the appropriate shape for the grains the relative evolution of the parameters is insensitive to the shape assumption.

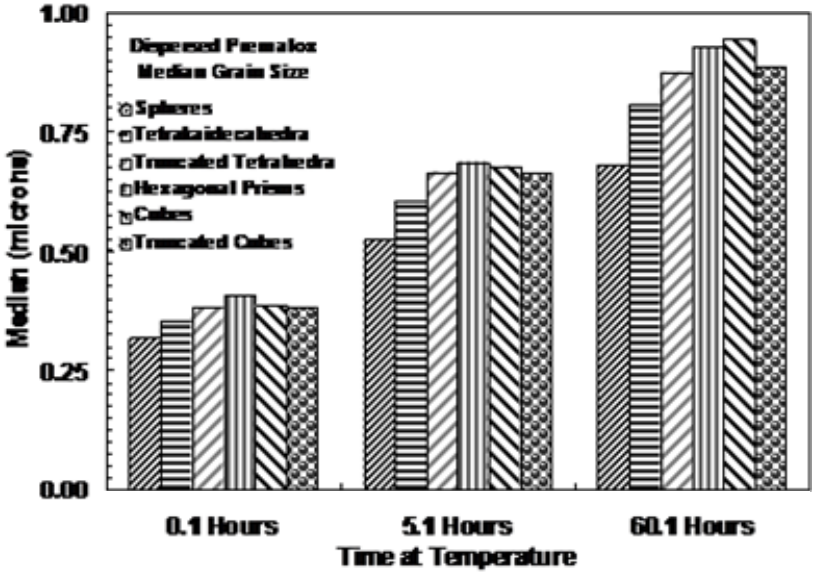

Figure 38: The median grain size for dispersed alumina shows a systematic variation with different assumed shapes. The distribution using spheres always has the lowest value. The tetrakaidecahedra values are the closest to the spheres. The remaining shapes have approximately the same values as each other.

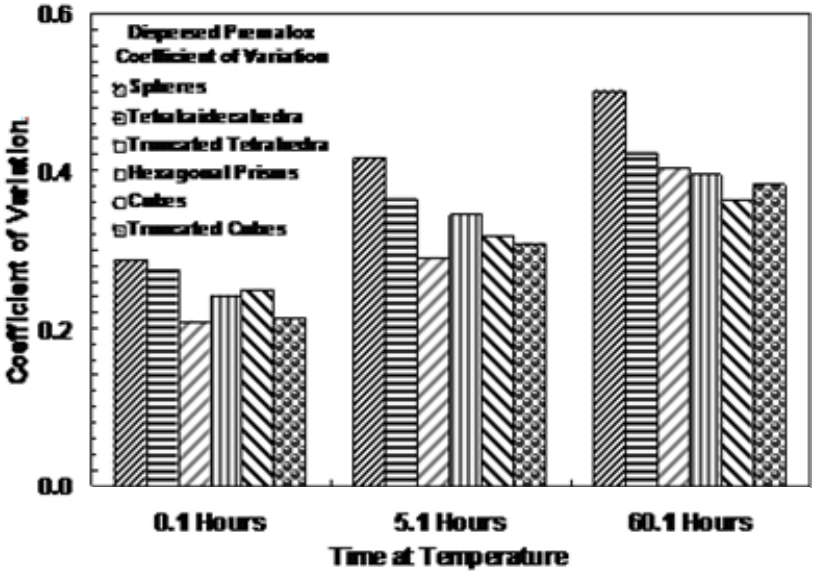

Figure 39: Although the truncated cube is the most appropriate shape, there is a systematic difference between the coefficients of variation between the shapes. The choice of shape has little impact on the determination of the evolution of the grain size distribution.

The median and coefficient of variation for all alumina samples sintered at 1350ºC are given in **Figure 40** and **Figure 41**. Just as the average parameters and their dimensionless ratios are insensitive to the casting condition so are the distribution parameters. A single path could be used to approximate the evolutionary paths of both the flocculated and dispersed conditions in the median versus solid volume fraction plot (**Figure 40**). The median grain size is approximately 0.35μm at low solid volume fractions and increases to approximately 0.75μm at high solid volume fractions. If the scatter in the data near 0.95 solid volume fraction is ignored in **Figure 41** a single path can also be used for the evolution of the coefficient of variation. Like the increase in median grain size, the coefficient of variation only increases by a factor of two from low to high solid volume fractions (~0.25 → ~0.5). The broadening of the distribution in grain size is not consistent with the definition of normal grain growth usually used in sintering models. The grain growth does not fit the usual definition of abnormal grain growth as well. While the distribution does broaden, large tabular grains usually associated with abnormal grain growth are rarely seen in these microstructures. Also, significant grain growth and the increase in the width of the distribution of grain size does not begin until the solid volume fraction is greater than 0.9.

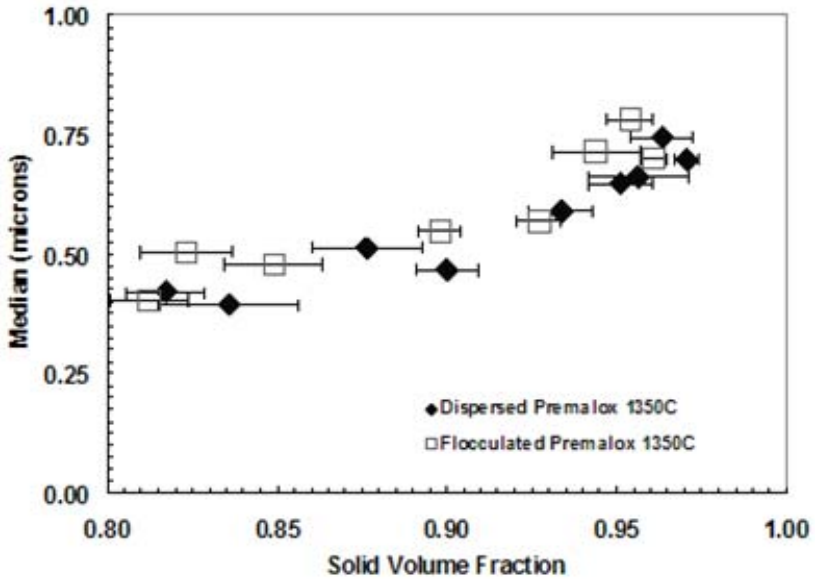

Figure 40: Flocculation has little effect on the evolution of the median grain size. Flocculated and dispersed alumina follow the same general trend. There is little change in the median until approximately 0.95 solid volume fraction. Archimedes measurements indicate that the pores are closed at this solid volume fraction.

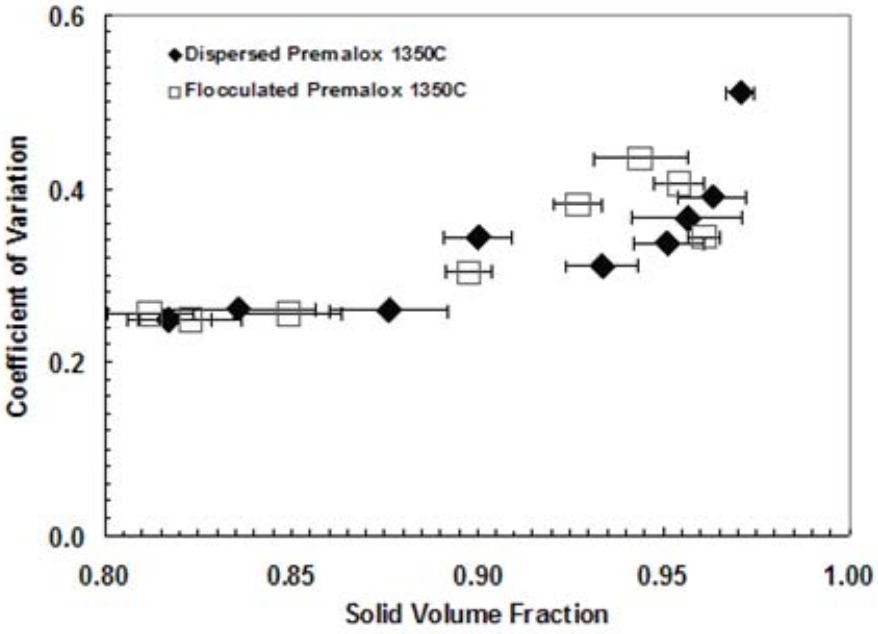

Figure 41: There is some difference between the coefficients of variation for flocculated and dispersed alumina in the range of 0.90 to 0.95 solid volume fraction. However, their values are comparable outside of this range. The effect of flocculation is minimal on the evolution of the distribution parameters.

The evolutionary paths of the average microstructural parameters, their ratios, and the distribution parameters as a function of solid volume fraction are relatively insensitive to casting conditions. If the difference in densification rates for flocculated and dispersed alumina sintered at 1350ºC at a given solid volume fraction is governed by characteristics of the microstructure, some other microstructure parameter must be developed. Examination of micrographs for dispersed (0.6 hours, **Figure 42**) and flocculated (1.1 hours, **Figure 43**) alumina sintered at 1350ºC with approximately the same solid volume fraction, 0.87 and 0.85, respectively clearly shows that while both samples have approximately the same surface area ratios, intercept ratios, and distribution parameters there is a noticeable difference in the microstructure at a scale higher than the length scale of the grains or pores.

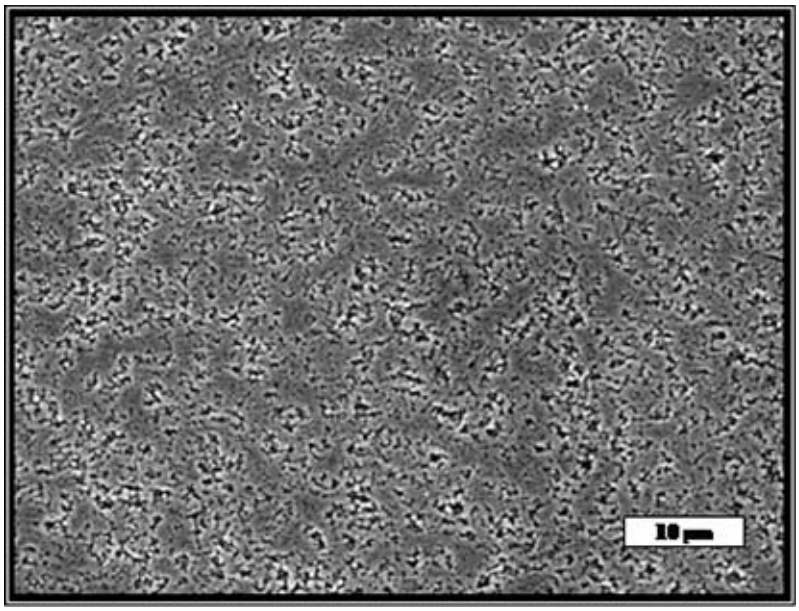

Figure 42: SEM micrograph of dispersed alumina sintered for 0.6 hours at 1350ºC with a solid volume fraction of 0.87.

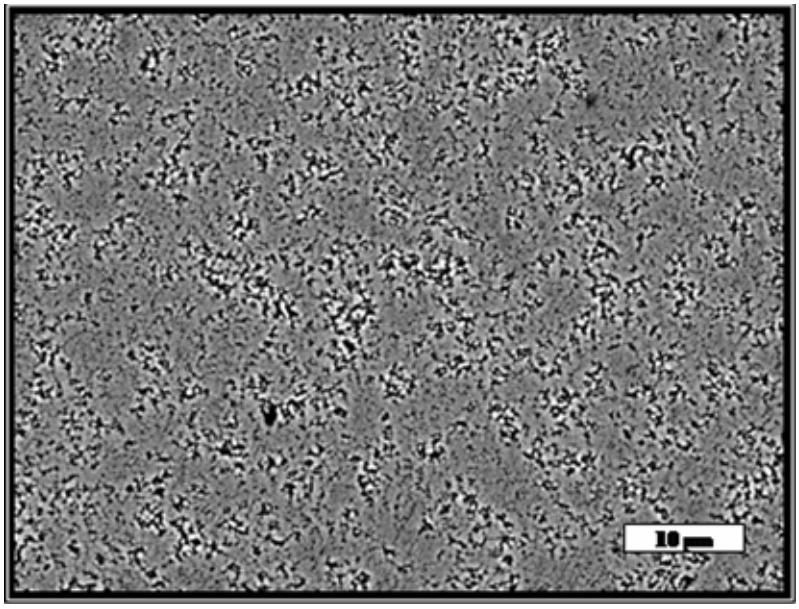

Figure 43: SEM micrograph of flocculated alumina sintered for 1.1 hours at 1350ºC. Although the solid volume fraction, 0.85, is approximately the same as the dispersed sample in Figure 42, there is a significant difference in the apparent size of the clusters.

6.3 SECTION SIZE EVOLUTIONS

6.3.1 Grain Section Size Distributions

The evolution of the grain size distribution was characterized for the dispersed and flocculated alumina through the entire density range of the experiments. It was shown in the results for estimation of the 'true' grain size distribution that there was no significant difference due to casting condition at a specified density. Since, the pore section area and cell area are also studied in this work and the correlation between grain size and morphology is also examined, it is necessary to examine the distributions in grain section area. **Figure 44** shows the grain section area distributions at low, intermediate and high densities for both dispersed and flocculated alumina. There is an evolution in the grain size with density (**Figure 45**). As density increases the distributions in grain size move to larger values as was shown by the evolution of the 'true' grain size distributions. The 'true' grain size distributions results were given in equivalent diameters. The grain section results are given in areas. Therefore, the increase by a factor of two in the 'true' distribution parameters corresponds to an increase by a factor of four in the section area distribution parameters. The distributions at a solid volume fraction of 0.82 for dispersed and flocculated alumina show a small difference in the position of the peaks (**Figure 46**). The flocculated grain section areas are slightly larger than those for the dispersed alumina. However, at a solid volume fractions of 0.90 and above, the distributions are very similar.

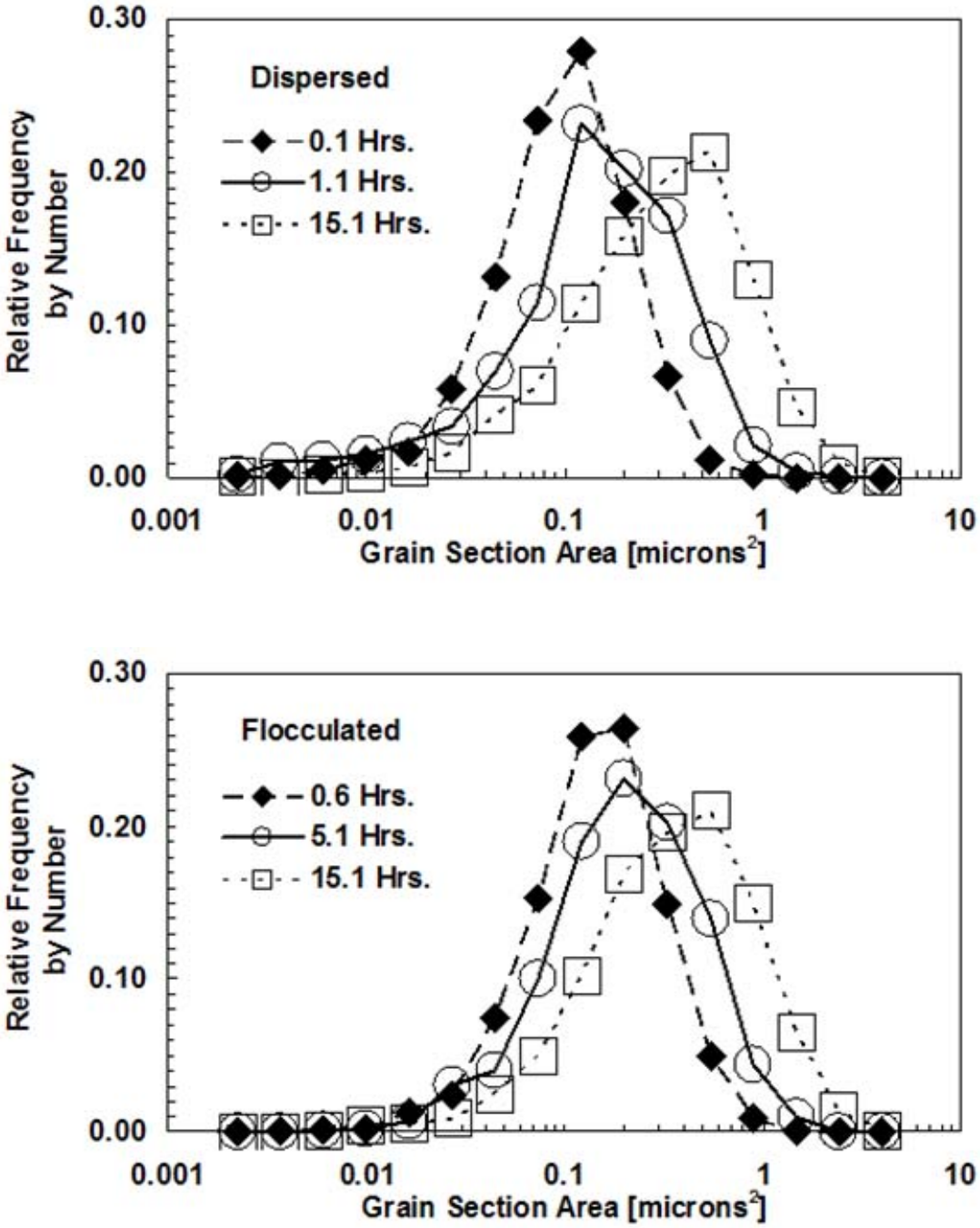

Figure 44: The grain section areas distributions for both dispersed and flocculated alumina evolve with densification. The distributions broaden and the mean values increase with increasing density.

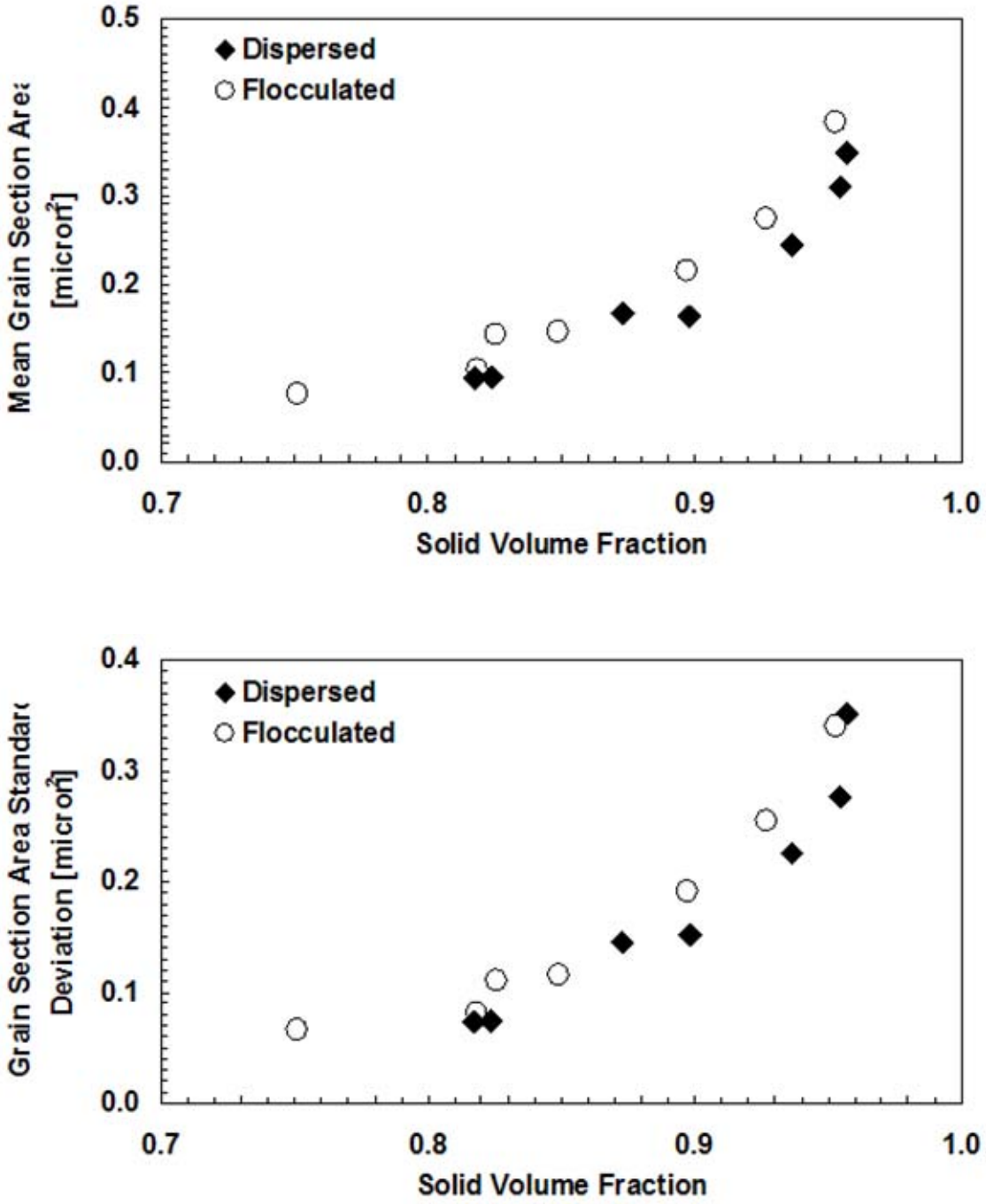

Figure 45: Evolution of the grain section area distribution parameters, mean and standard deviation, for dispersed and flocculated alumina with solid volume fraction. The distributions follow nearly identical paths.

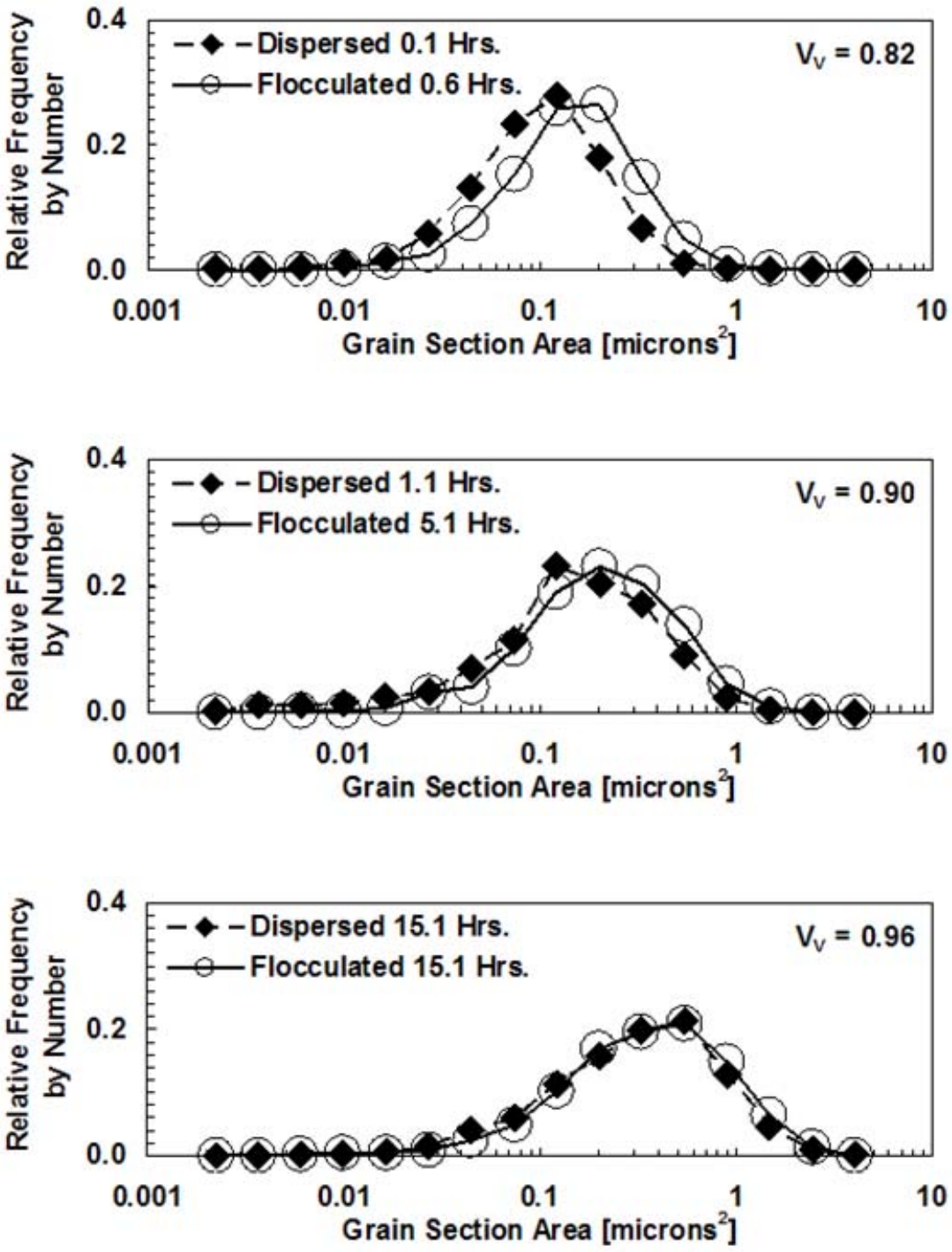

Figure 46: Although there is a relatively small difference between the dispersed and flocculated grain section distributions at a solid volume fraction of 0.82, the difference diminishes with increasing density.

6.3.2 Pore Section Size Distributions

The degree of dispersion during slip-casting is known to have an effect on the initial solid volume fraction of a casting. The more flocculated a slip is, the lower the green density will be. The initial arrangement of particles will affect the densification kinetics of the cast with time. The densification rate of the flocculated samples was greater than that of the dispersed samples at any time during the intermediate stage of sintering. However, at a given density during the intermediate stage of sintering, the densification rate was higher for the dispersed samples than for the flocculated samples.

Differences in the packing behavior due to casting conditions may have an effect on the distributions in pore section area in the green body and during subsequent densification. **Figure 47** shows the evolution of the commonly used relative frequency of pore section areas by number for dispersed and flocculated alumina at low, intermediate and high densities. There is an evolution in the distributions of pore section area but interpretation of the relative frequency may not be very intuitive. Absolute frequency by number clearly shows how the pore population is changing. N_A may be reduced by elimination of pores within the same area and/or by an increase in pore spacing due to coarsening. As density increases, N_A, the total number of pore sections per unit area decreases (**Figure 48**). The evolution of the pores section area distributions is shown in **Figure 49** by number per unit area and in **Figure 50** by the area fraction of the sample section. These are absolute frequencies rather than the relative frequency given in **Figure 47**. It better illustrates the changes in the pore population. It is apparent that the evolutions for dispersed and flocculated alumina are different. The pore population for dispersed alumina tends to ’collapse’ downward, the peak remains in about the same position, while the flocculated distributions tend to ‘collapse’ to smaller section areas, the peak shifts to smaller section sizes.

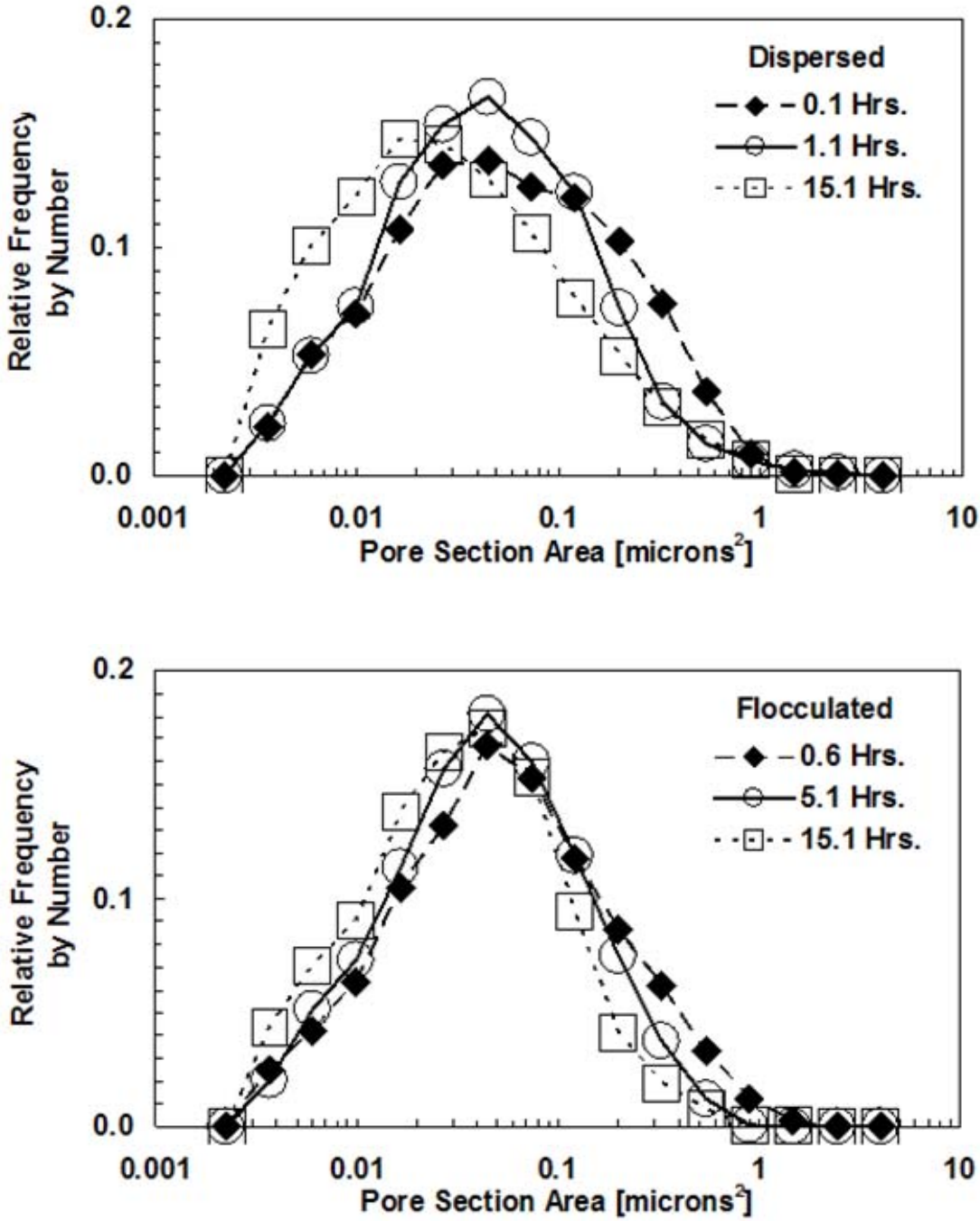

Figure 47: The pore section area distributions by number frequency for dispersed and flocculated alumina show some evolution with density. There is a trend in the movement of pore section area to smaller values as density increases. However, in the dispersed case many of the larger pore sections remain to high solid volume fractions.

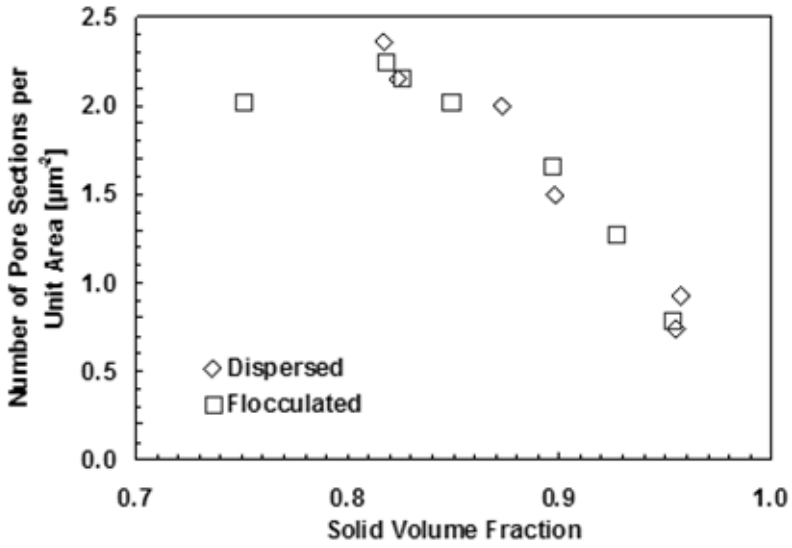

Figure 48: Number of pore sections per unit area for dispersed and flocculated alumina at each solid volume fraction. As with many other parameters, dispersed and flocculated have similar values at each density. In the case of flocculated alumina initially there is a small increase in N_A. There is approximately a linear decrease in N_A with increasing solid volume fraction through the intermediate stage of sintering.

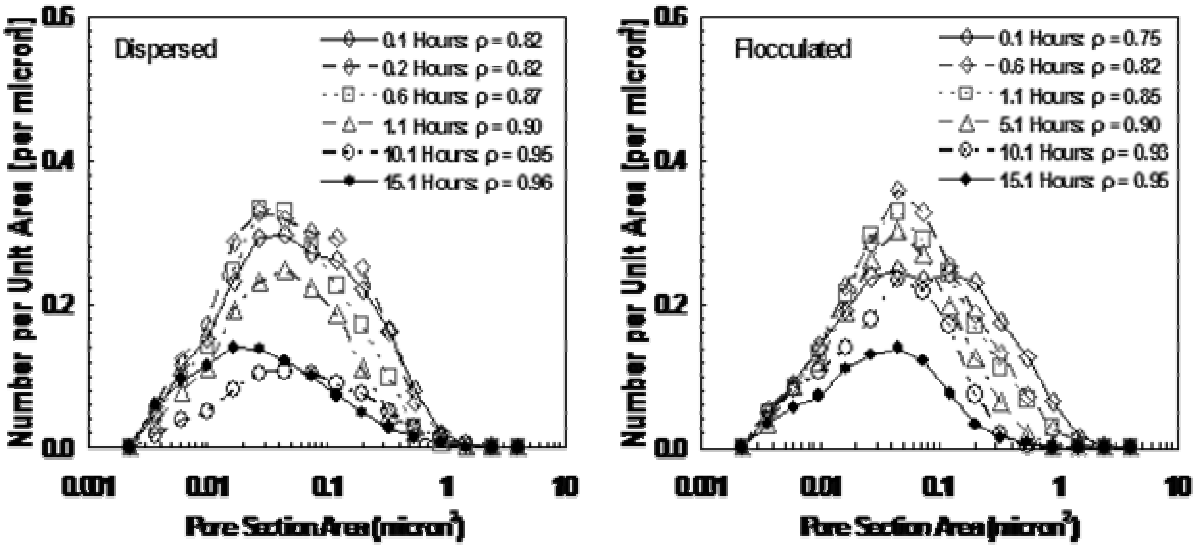

Figure 49: Pore section area distributions in number per unit area demonstrate the differences in the evolutions for dispersed and flocculated alumina in a more intuitive manor than relative frequency.

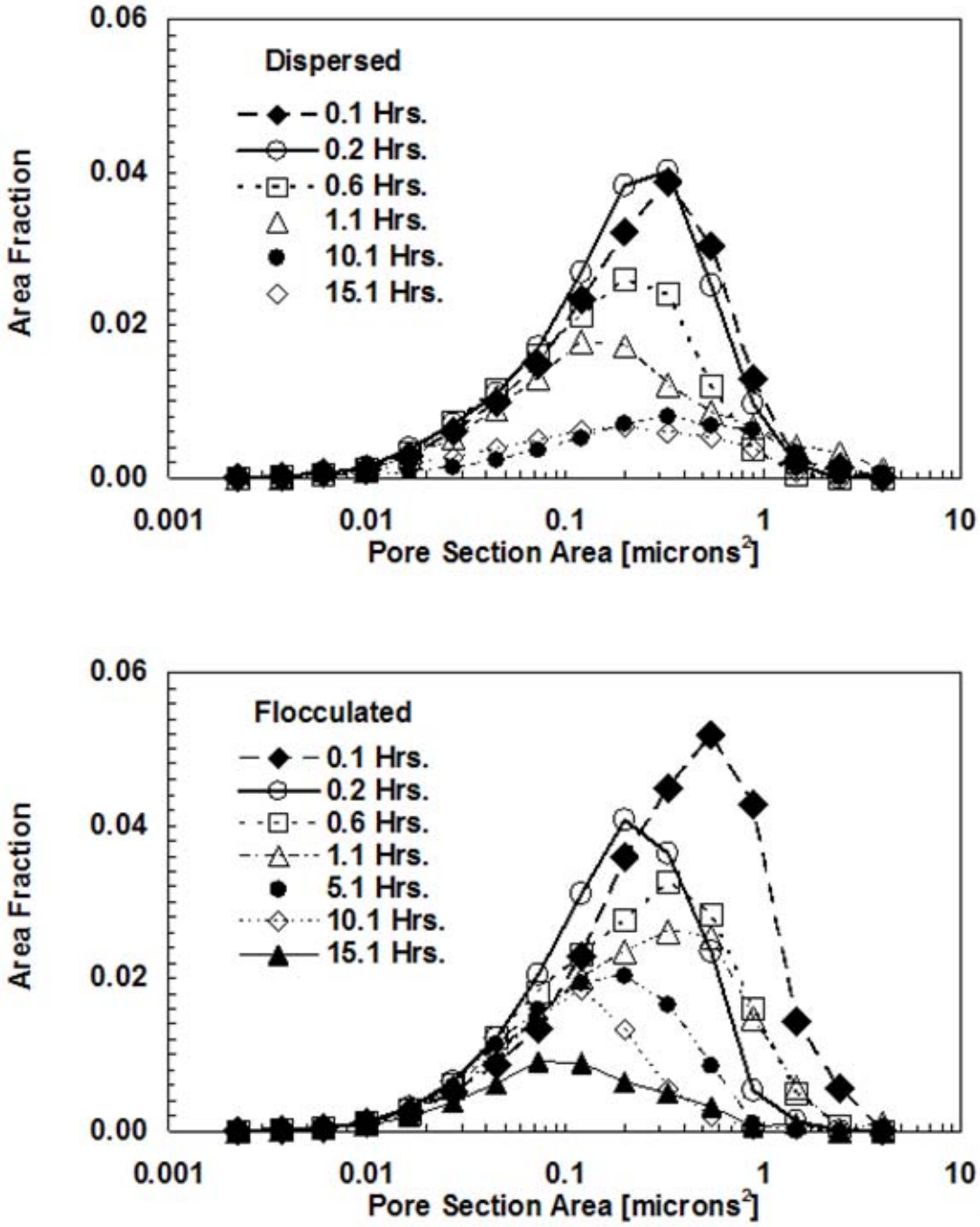

Figure 50: The pore section area distribution by area fraction of the sample section shows the evolution of the pore size distribution more clearly than the relative distributions by number. It is apparent that the area associated with the pore sections having areas larger than the mode of the distribution remain to the later stages of sintering in the dispersed case while those pore sections are removed in the flocculated case.

Figure 51 shows the evolution of the pore populations for dispersed and flocculated alumina at low, intermediate and high solid volume fractions. The trends are clear. Larger pore sections in the dispersed samples persist to higher densities. The differences in the pore section distributions may be responsible for the different densification rates at different solid volume fractions for dispersed and flocculated alumina. However, comparisons between dispersed and flocculated samples at the three densities (**Figure 52**) reveals that although the distributions are significantly different at higher solid volume fractions, the distributions at the lower solid volume fraction are very similar. The distribution parameters are plotted in **Figure 53** confirming that the distributions are similar at low solid volume fraction but evolve differently.

The densification rates for dispersed and flocculated alumina during the intermediate stage of sintering show the largest difference at the lowest common solid volume fraction. The difference decreases until final stage sintering begins. If the difference in densification rates is solely attributed to the difference in the pore section area distributions, the difference in the pore section area distributions would be the most pronounced at the lower solid volume fraction.

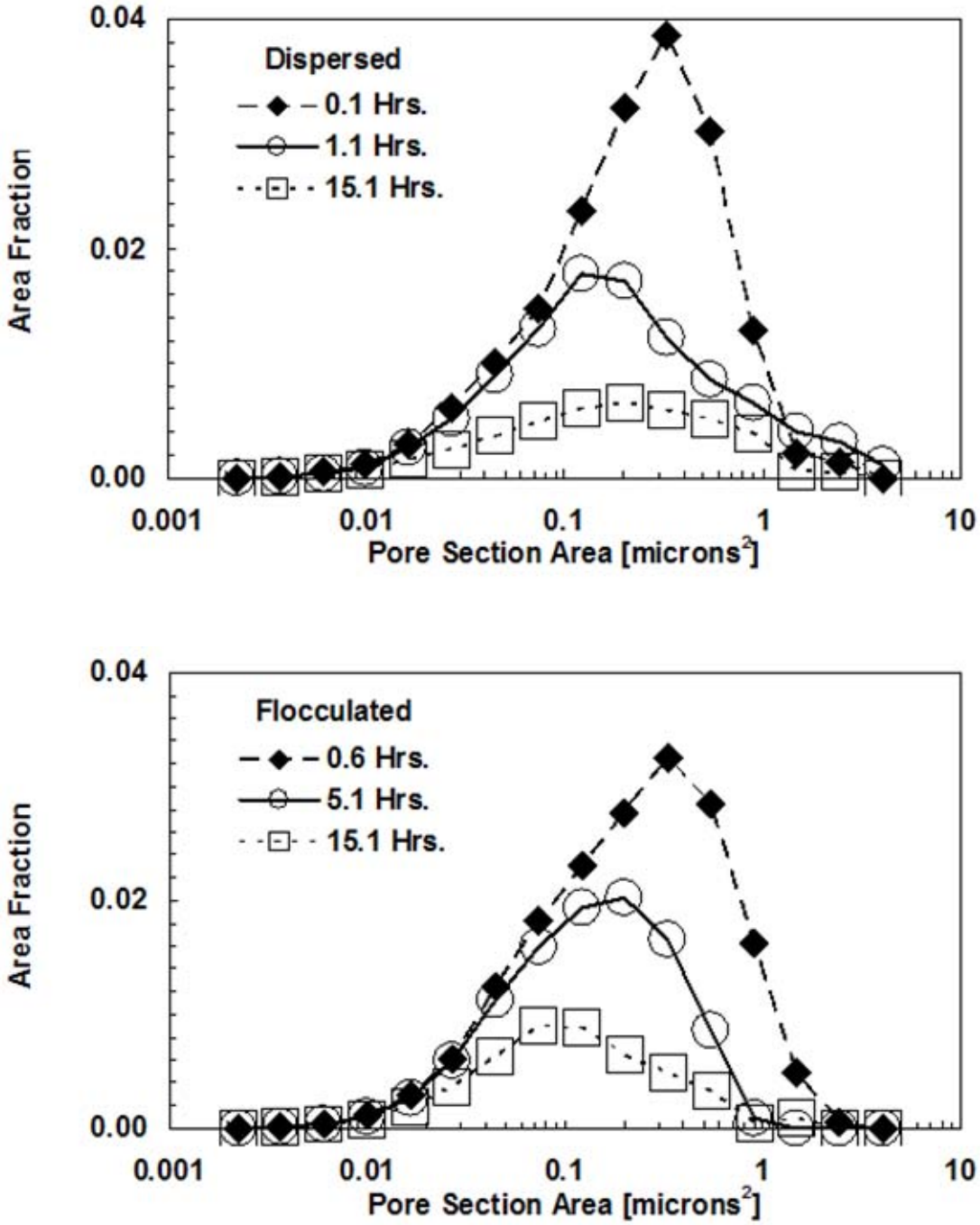

Figure 51: The above figures show the pore section area distributions by sample area fraction for the low, intermediate and high densities for the dispersed (top) and flocculated (bottom) alumina. The same trends are observed as in Figure 50.

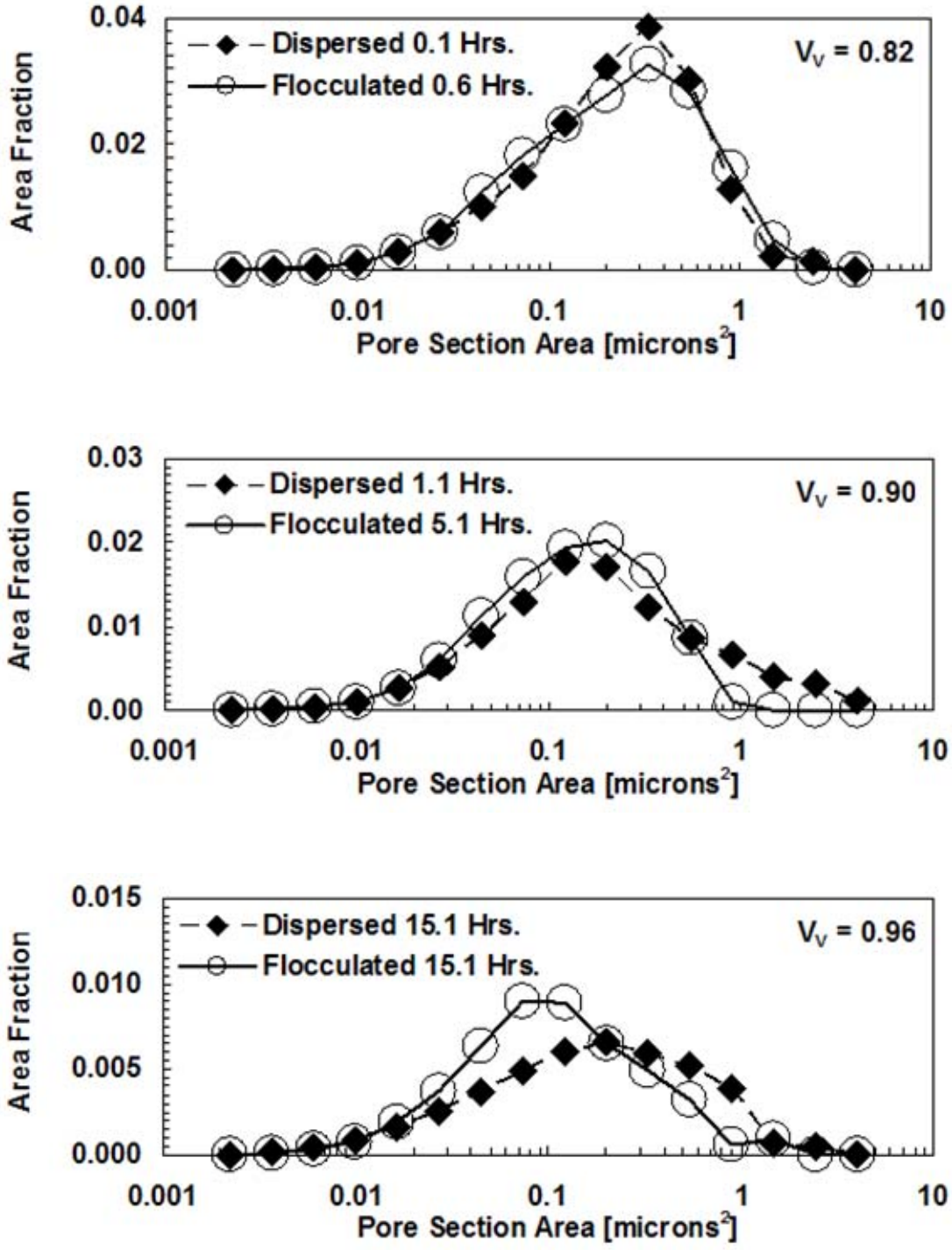

Figure 52: A comparison of the pore section area distributions for dispersed and flocculated alumina at a solid volume fraction of 0.82 shows little difference between the samples. It is clear that the distributions evolve differently with increasing density. The distributions show significant differences at 0.90 and 0.96 solid volume fractions.

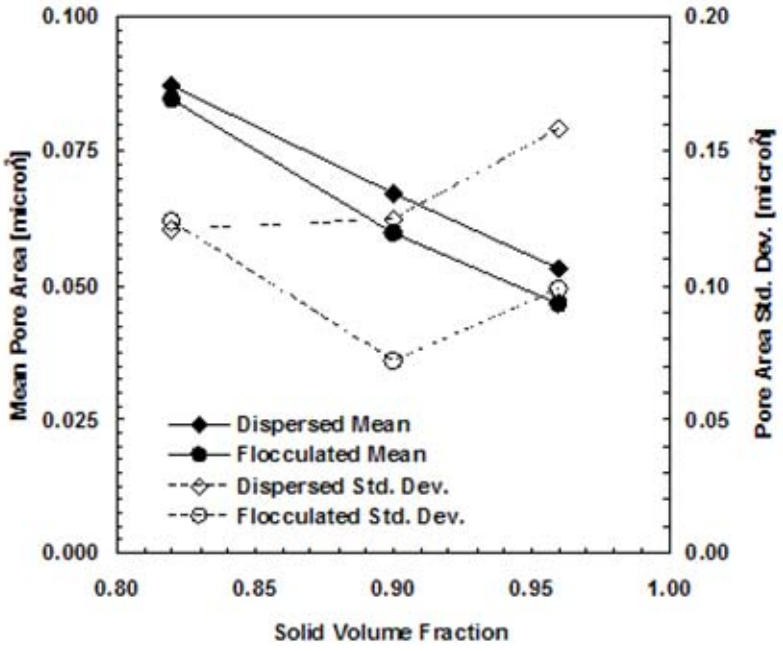

Figure 53: The pore section area distribution parameters (mean and standard deviation) for dispersed and flocculated alumina confirm the observation that the distributions are similar at low solid volume fraction but diverge as density increases.

6.4 FEATURE MORPHOLOGY

6.4.1 Grain Cross-section Morphology

The effect of morphology was investigated using the dimensionless shape factor Q. Valid values for Q are greater than 0 and less than or equal to 1. Q equal to 1 is a special case, circular sections. The lower the value of Q the less circular the section is. As would be expected for more equiaxed sections of grains, there is a distribution in Q dominated by intermediate Q values. There is little evolution of the grain section morphology with changes in density as illustrated by distributions given in Figure 54. However, as density increases the peaks shift to lower values of Q. This indicates that the shapes of the grain sections are becoming less equiaxed with increasing density. The change is not extreme, as would be indicative of 'abnormal grain growth' characterized by the presence of tabular grains[1]. Additionally, the plots shown in Figure 55 show that there is little difference between the Q distributions for dispersed and flocculated alumina at similar densities. Also, the cell maps of grain section area and Q relative frequency distributions by number shown in **Figure 56** are similar at each solid volume fraction. Grain section morphology is unlikely to be responsible for the different evolutionary paths of dispersed and flocculated alumina.

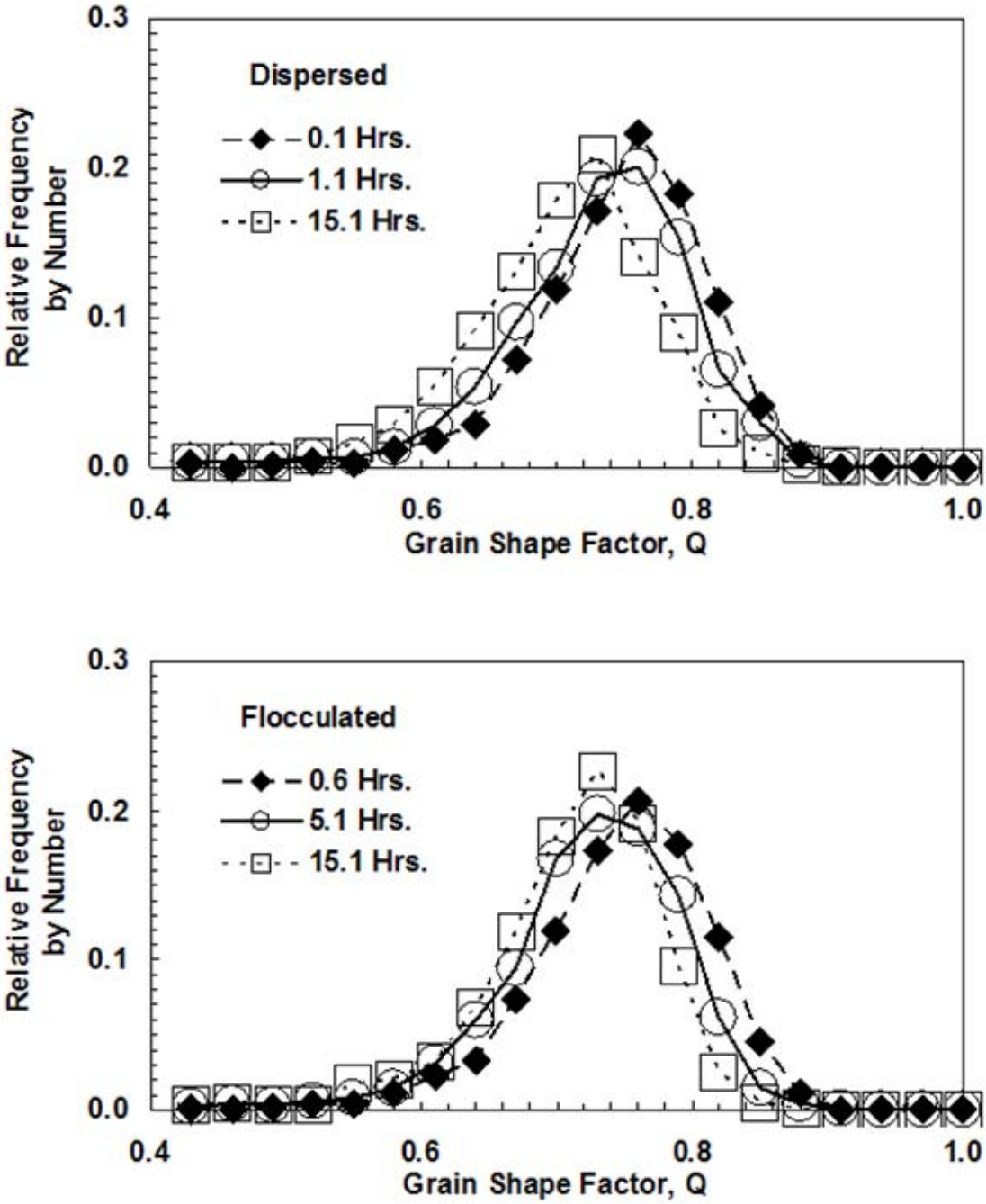

Figure 54: The shape factor distributions for grain sections for dispersed (top) and flocculated (bottom) alumina exhibit an evolution with density. Only the distributions at low, intermediate and high solid volume fractions are shown for clarity. As the density increases the mode of the distributions moves to lower values of Q. This indicates that the grains have become somewhat less equiaxed at higher densities.

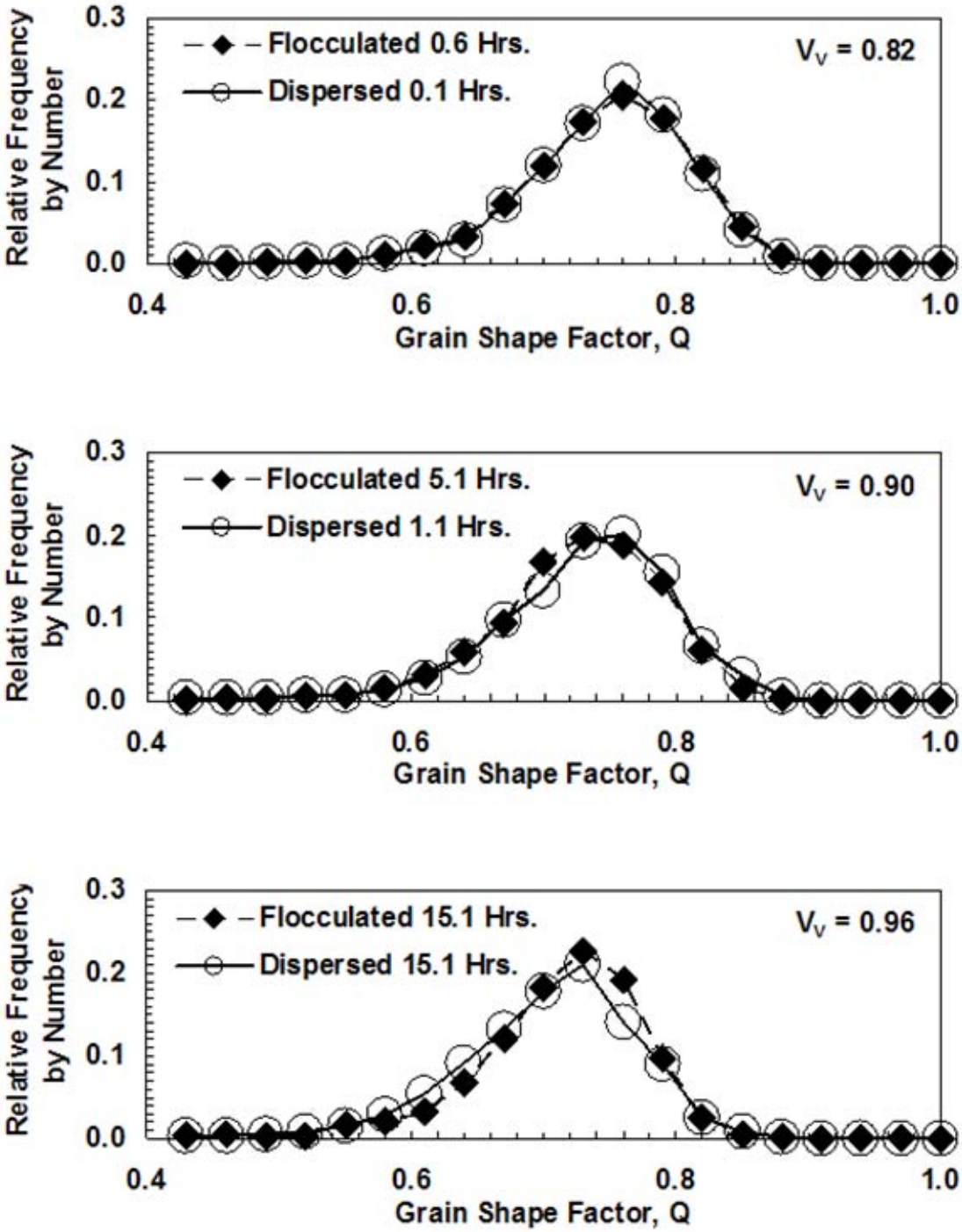

Figure 55: While the shape factor distributions for both dispersed and flocculated alumina evolve with density as seen in Figure 54, the flocculated and dispersed distributions are almost identical when compared at similar densities.

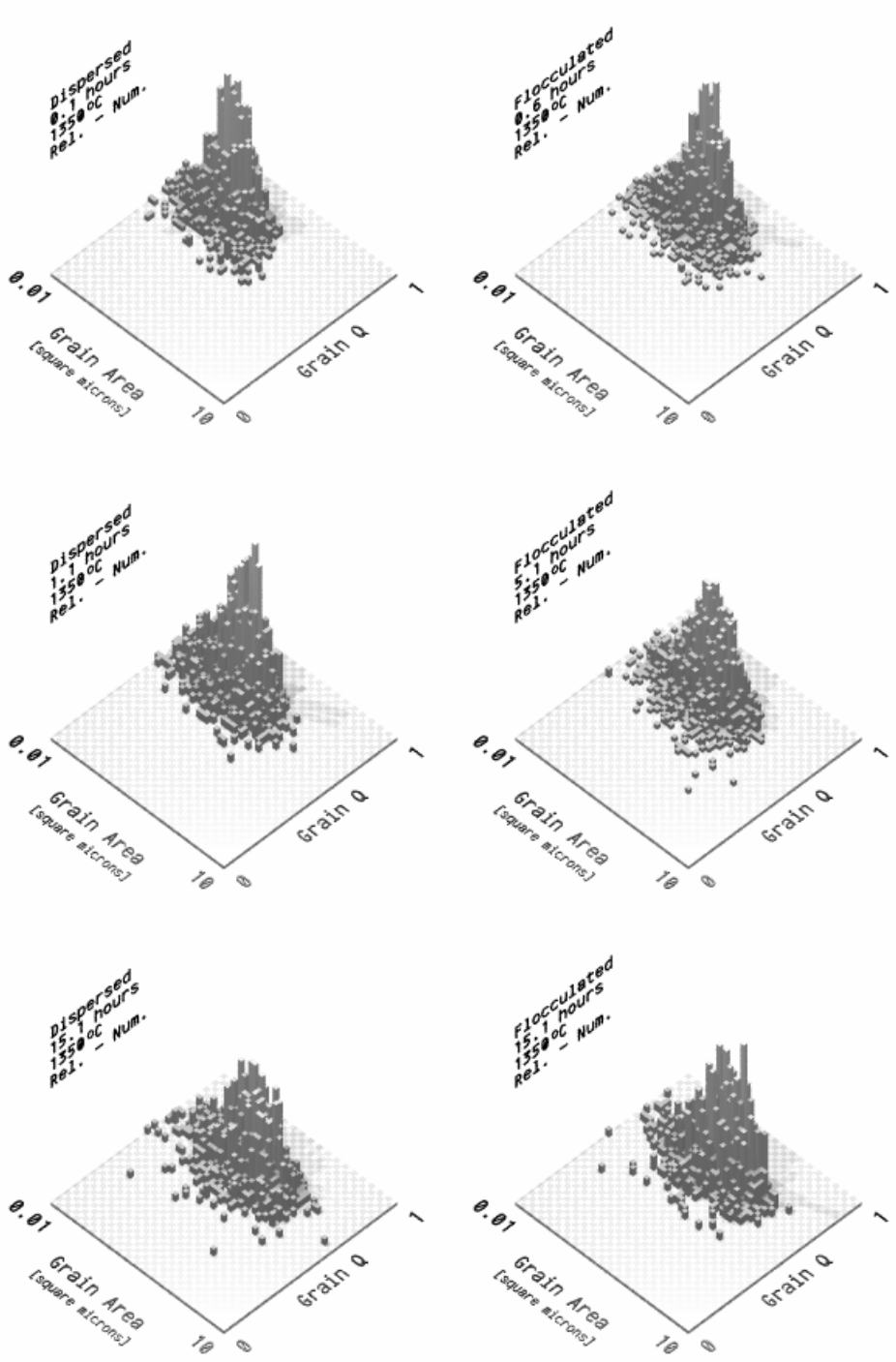

Figure 56: There are no significant differences between the dispersed and flocculated alumina relative frequency distributions in grain section Q with grain section area at any of the solid volume fractions.

6.4.2 Pore Section Morphology

The shape factor distributions for the pore sections are given in Figure 57 for dispersed and flocculated alumina. In this case, there is a very wide distribution in the shape factors for both casting conditions. The lower values of Q are associated with elongated pore sections with a mixture of convex and concave boundaries. The boundaries of the pore sections are defined by the free surfaces of grains. Since the grains are relatively equiaxed and many pore sections are coordinated with multiple grains, it should be expected that many pore sections would not be equiaxed. Interestingly, the distribution of shape factors for pore sections remains relatively unchanged during the densification process. This may indicate that pore sections retain their shape as their size either increases or decreases during the densification process or, a proportional amount of each shape are removed as densification proceeds. Again, as in the case of grain section morphology, the dispersed and flocculated shape factor distributions are similar (Figure 58) at each solid volume fraction.

Since the distributions in the pore section shape factor distributions for dispersed and flocculated alumina are similar at each solid volume fraction, the correlation between pore section shape and area should be investigated using cell maps. The cell maps of pore section area and Q are shown in **Figure 59**. Accounting for the narrowing and shifting of the flocculated pore section distribution to smaller section sizes, the dispersed and flocculated distributions at low and intermediate solid volume fractions are similar (times less than 15 hours).

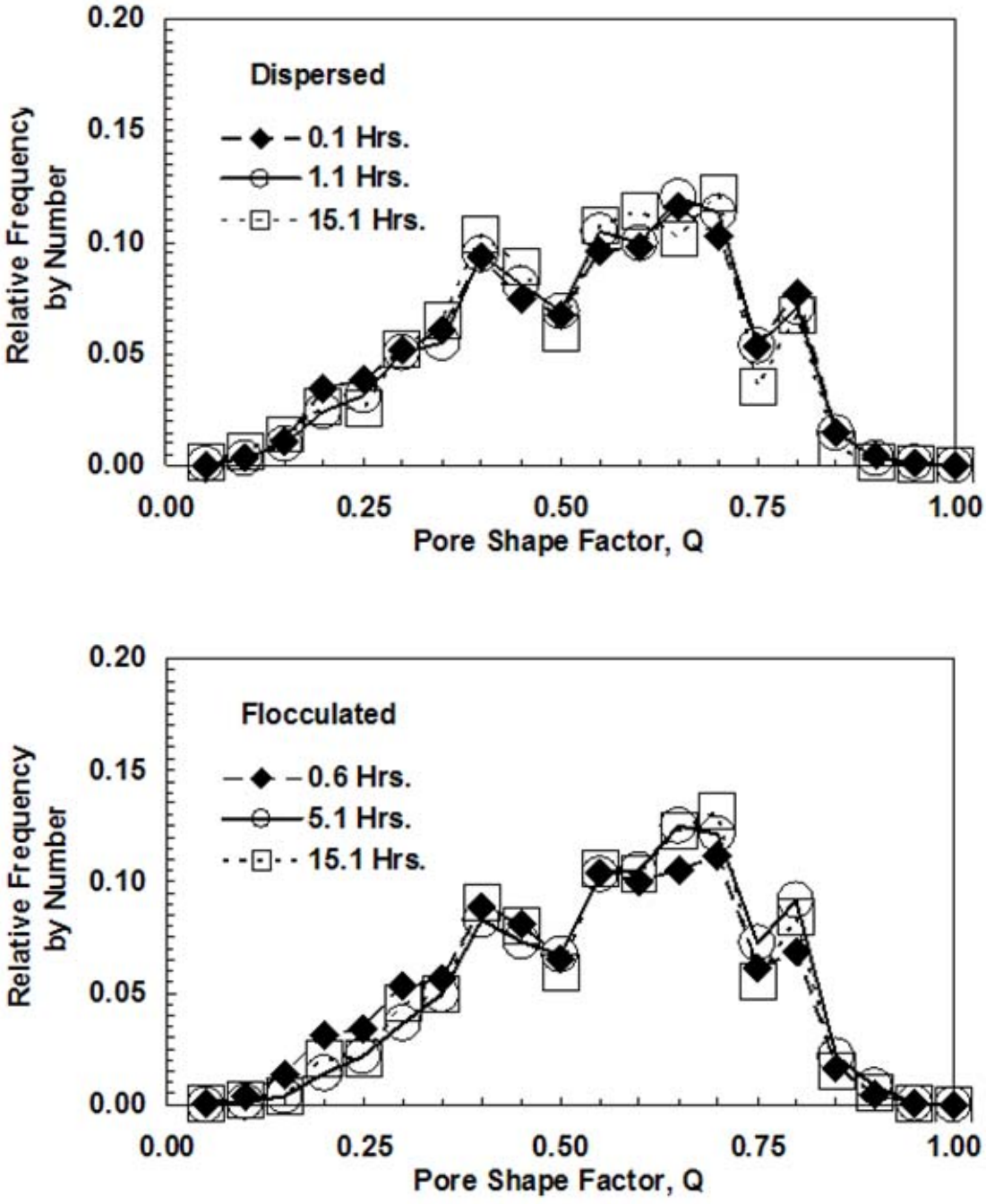

Figure 57: The shape factor distributions for pore sections for dispersed (top) and flocculated (bottom) alumina exhibit very little evolution with density. Only the distributions at low, intermediate and high solid volume fractions are shown for clarity. This may indicate that as pore sections evolve, they retain their shape.

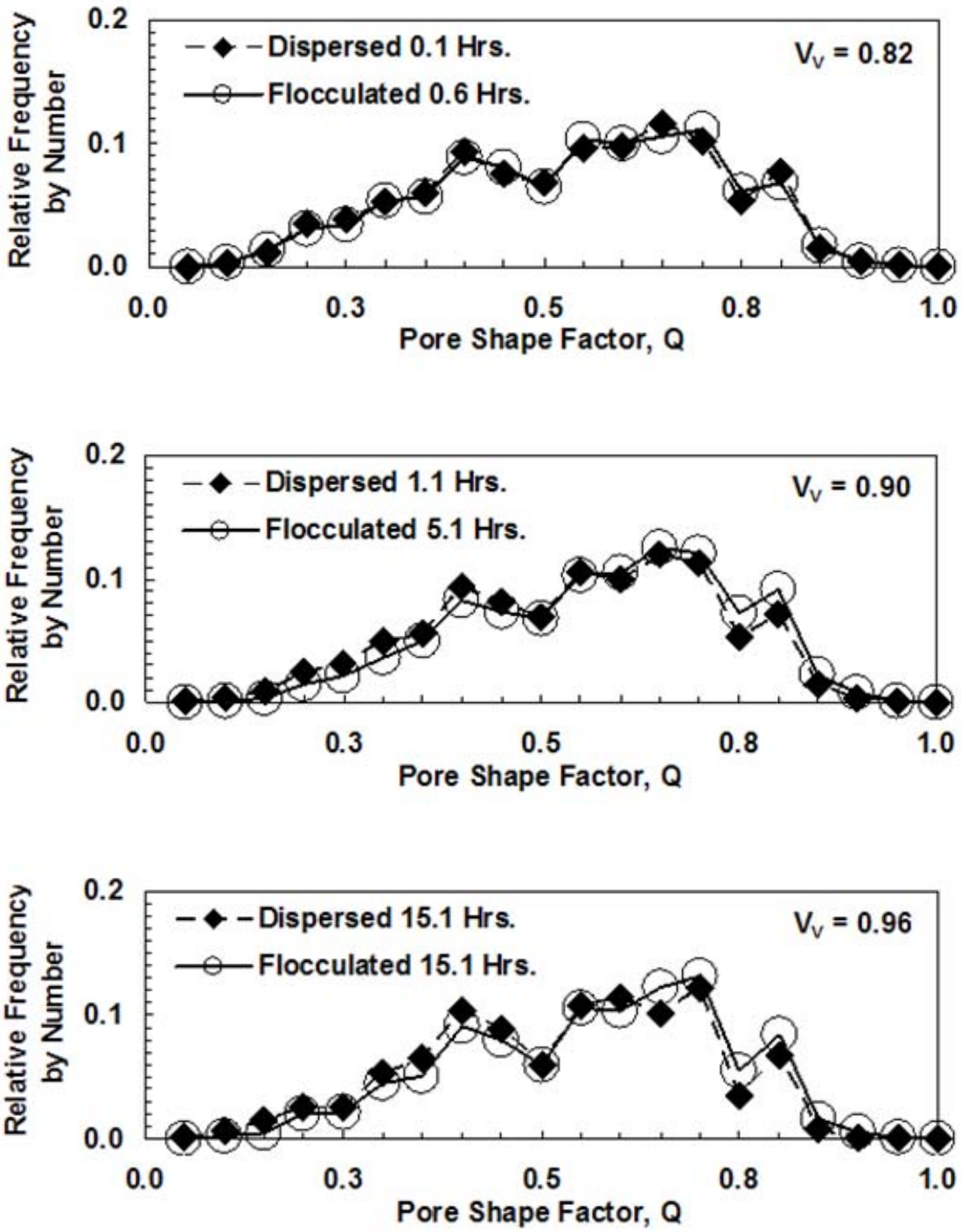

Figure 58: The distributions in pore shape factor are nearly identical for both the dispersed and flocculated conditions at all densities.

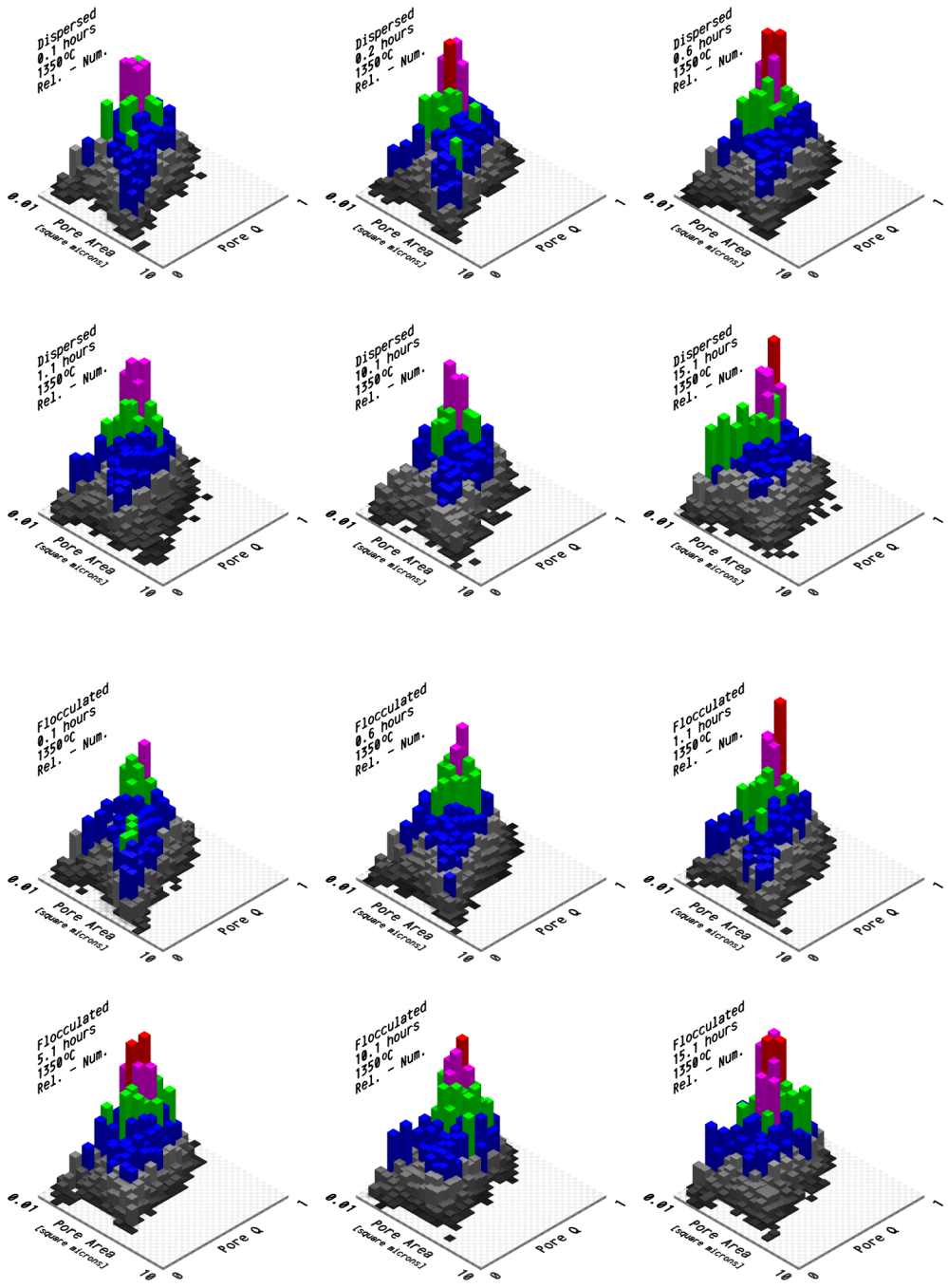

Figure 59: The relative frequency distributions by number for pore section area and pore section Q show that if the narrowing and shifting of the flocculated pore section distribution is accounted for, at times less than 15 hours the dispersed and flocculated alumina have similar distributions.

6.5 TESSELLATION AND THE IMMEDIATE ENVIRONMENT

The immediate environment is defined as the region contained within the boundaries of a tessellation cell. The cell contains one and only one pore section with its attendant solid area. The solid area generally consists of sections of more than one grain (**Figure 60**). The measures of interest include the cell solid area fraction and the other feature measurements (area, perimeter length, shape factor, etc.). Only the relationships between, cell area (CA), pore section area (PA), solid area fraction (SAF = 1 – PA/CA), and shape factor (Q) will be presented in this section. An example of a series of tessellation images with pore sections is shown in **Figure 61**. Each cell contains only one pore section. The color of each cell is related to the solid volume fraction of the cell. The color number does not relate intuitively to the SAF. Images must be converted to scaled color gradients for direct interpretation. An example of a color gradient image is given in **Figure 61** (bottom right).

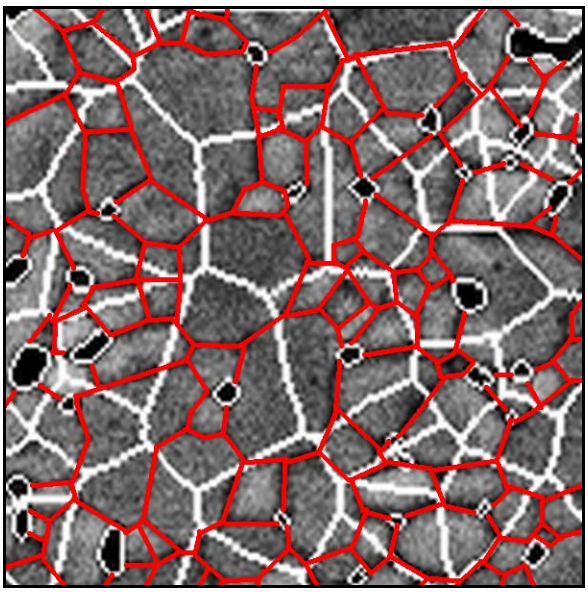

Figure 60: The image shows a portion of a micrograph with the grain boundaries indicated in red and the tessellation cell boundaries in white. Each tessellation cell contains only one pore section but includes more than one section of a grain.

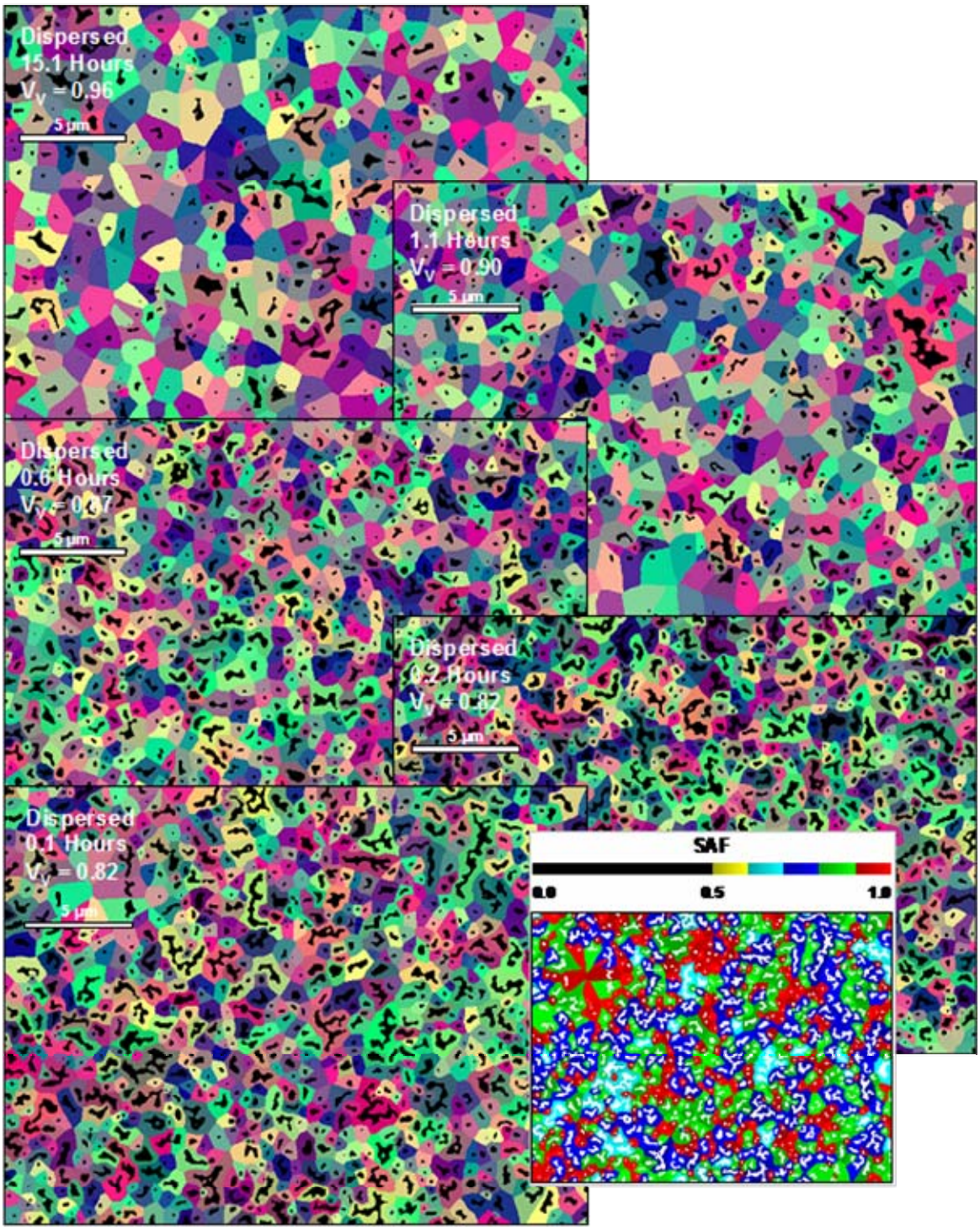

Figure 61: Series of tessellation images with pore sections for dispersed alumina. The black areas represent the pore sections. There is only one pore per tessellation cell. The bottom rightmost image has been converted to a graded color image. The scale bar above the image indicates the color corresponding to the SAF of the cell.

6.5.1 Tessellation Cell Size Distributions

The distributions in cell area for the low, intermediate and high solid volume fractions are given in Figure 62 for dispersed and flocculated alumina. Both, dispersed and flocculated alumina, show similar trends in the evolution of the cell area distributions. As expected, the number of pores per unit section area decreases as the size of the tessellation cells increases due to a net increase in pore spacing. The mean cell areas follow a similar path to that of the mean grain section areas (**Figure 63**). The mean cell area increases from approximately $0.4\mu m^2$ to $1.4\mu m^2$ from low to high solid volume fractions. However, unlike the grain section distributions, the width of the distribution, the standard deviation, does not increase until the highest solid volume fraction is attained (**Figure 63**). The standard deviation remains around $0.5\mu m^2$ until high solid volume fractions where it increases to about $0.8\mu m^2$. **Figure 64** shows the comparison of the distributions for dispersed and flocculated alumina at the low, intermediate and high solid volume fractions. The objective of using pore boundary tessellation in this work was to identify differences in the microstructure related to the spatial arrangement of pores. However, the distributions at similar densities for dispersed and flocculated alumina are similar. Even the distributions in cell area for the intermediate and high solid volume fractions are similar while at these densities the distributions in pore size are significantly different. It is apparent that the distribution in tessellation cell areas alone cannot be used to identify differences in these microstructures.

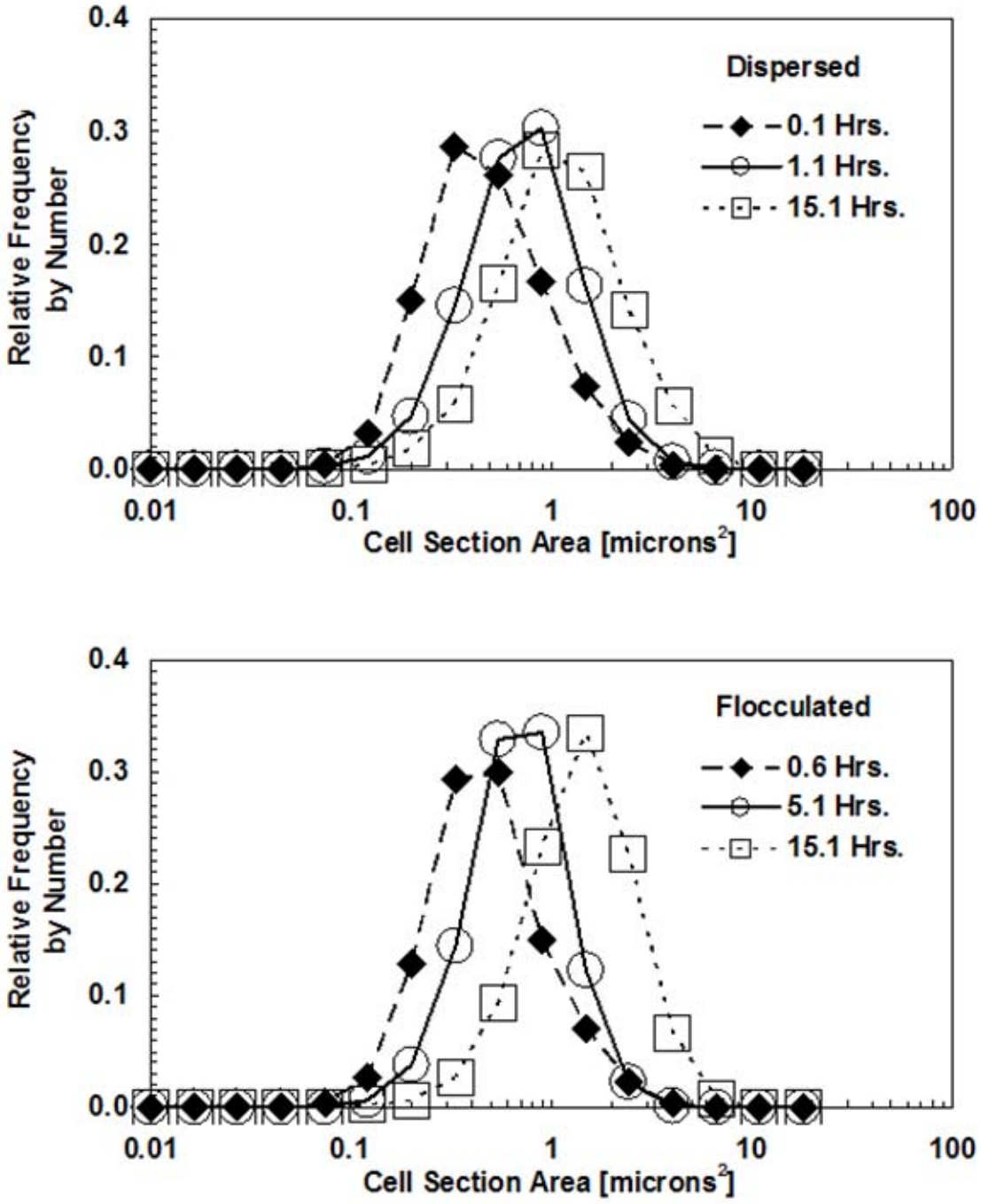

Figure 62: The distributions in cell section area show the expected trend of increasing size with increasing density due to the reduction in the number of pore sections per unit area and the increase in pore spacing.

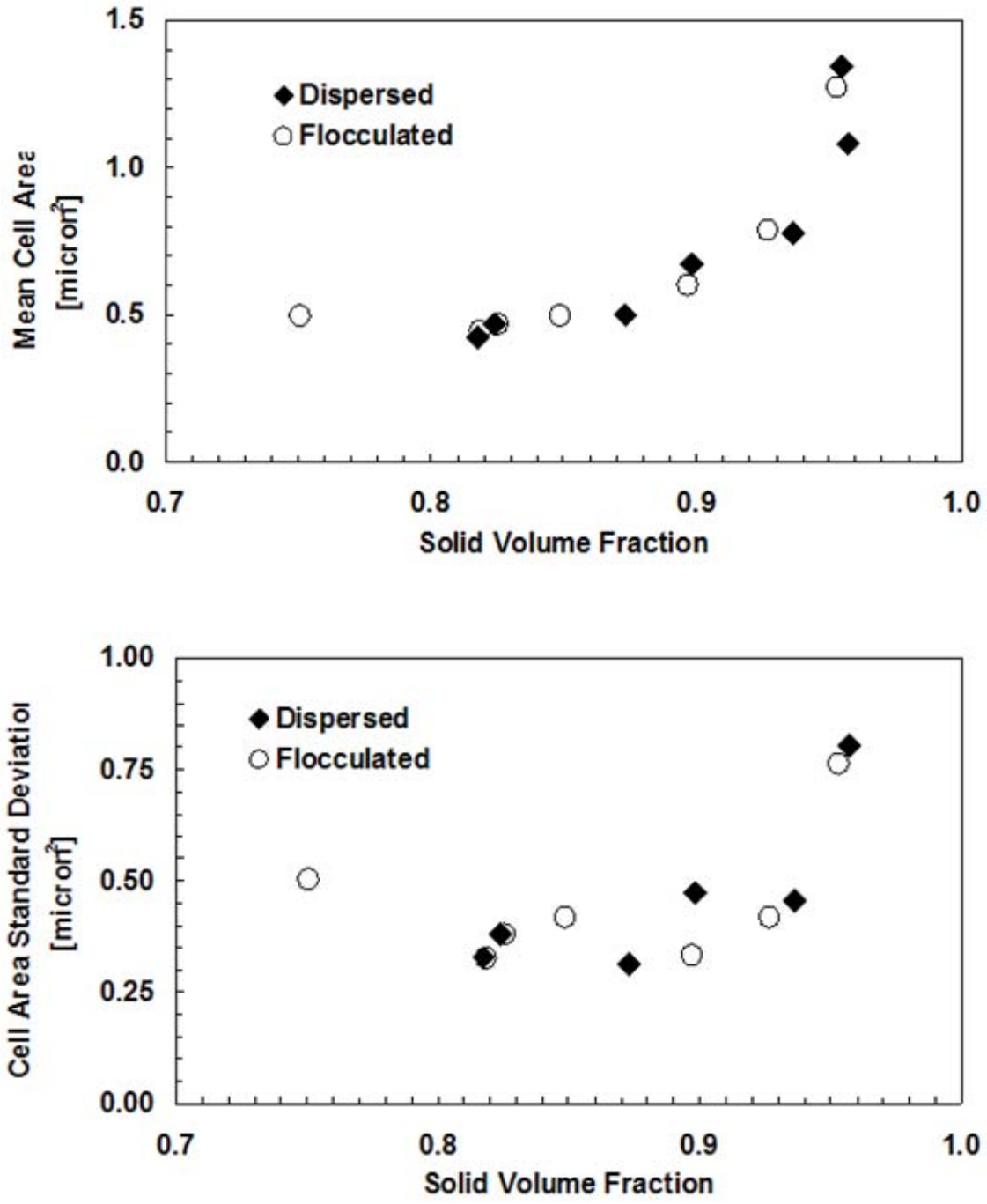

Figure 63: The cell area distributions evolve along similar paths with density for both dispersed and flocculated alumina.

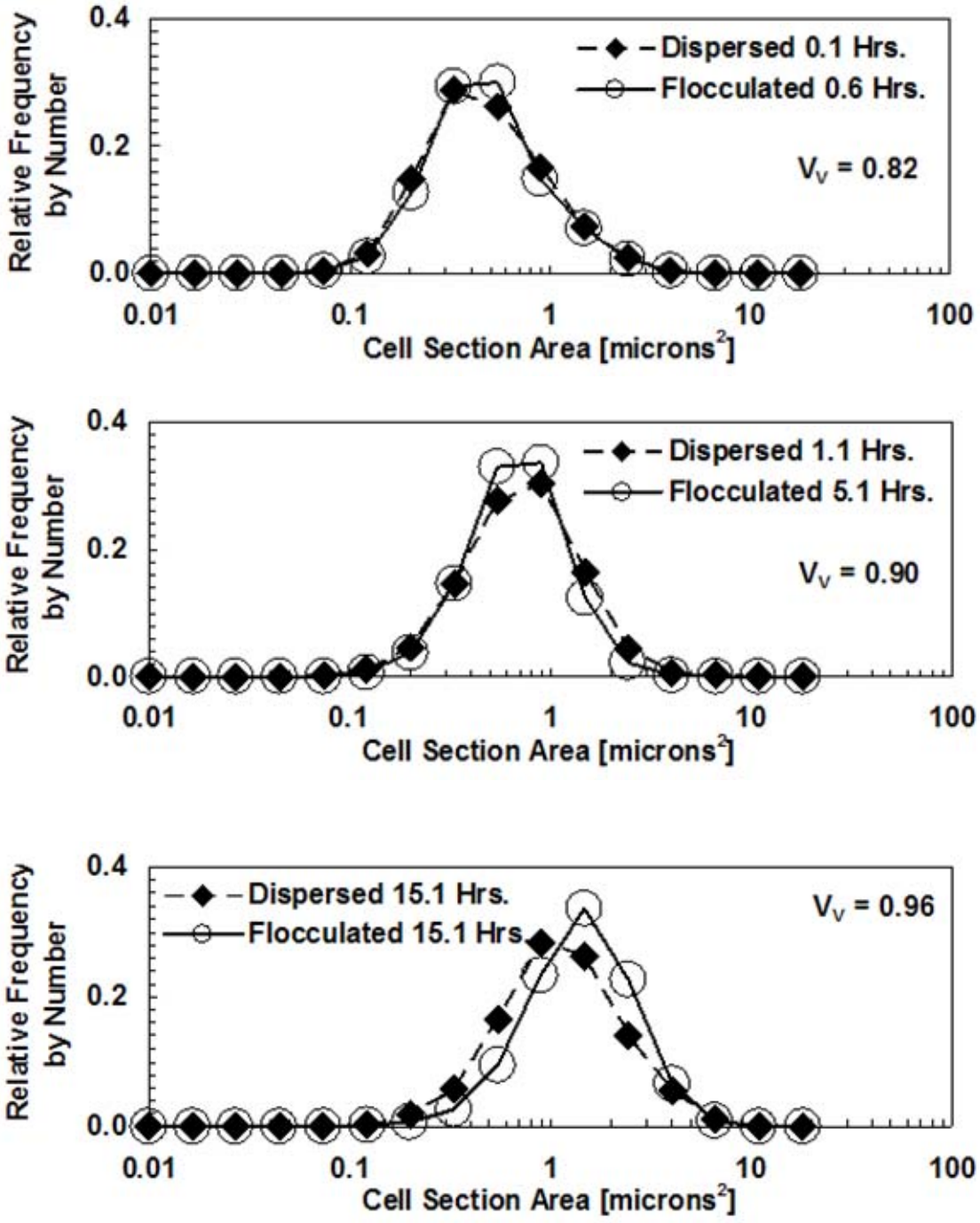

Figure 64: The cell section area distributions for dispersed and flocculated alumina evolve along the same path. The distributions are similar at similar solid volume fractions.

6.5.2 Tessellation Cell Solid Area Fraction

The cell solid area fraction distributions incorporate both the size of the pore contained within the cell and the size of the cell. All of the following distributions and cell maps related to the cell solid area fraction (SAF) of the tessellated cells will be weighted by the cell areas which presents the results in terms of the area fraction of the sample associated with cells. The area fraction distribution is presented in this way to emphasize the portion of the materialographic section associated with the particular cell properties. The distributions in **Figure 65** show the evolution of the distributions with increasing solid volume fraction. The evolutions are similar for both dispersed and flocculated alumina. Initially, at low solid volume fractions, the distributions are relatively flat for SAF greater than 0.7. At the intermediate solid volume fraction the distributions have a peak at about SAF equal to 0.97. When the higher solid volume fraction is achieved the distribution peaks are at SAF equal to 1.

The appearance of the peak at intermediate solid volume fraction may indicate that the cells with low SAF are increasing in SAF at a greater rate than the cells with higher initial SAF during the intermediate stage of sintering. Various events could be responsible for the increase in SAF of a cell: neighboring pore section elimination would result in a larger cell area; pore section spacing could increase due to coarsening resulting in a larger cell area; the spatial re-arrangement of pore sections could result in the increase in cell area for a small cell without significantly reducing the cell area of a large cell; or the pore section area could simply be decreasing,

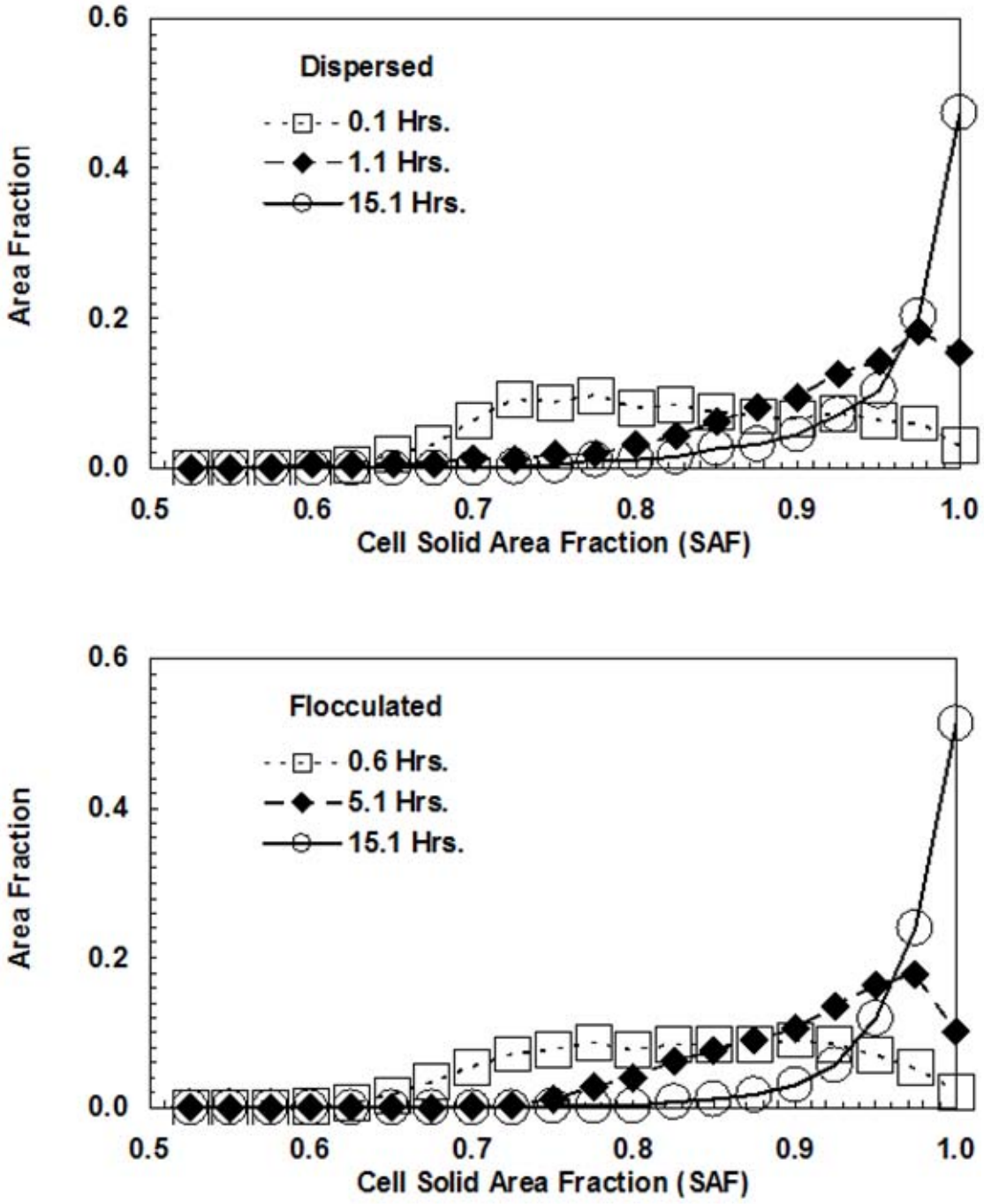

Figure 65: The distribution of cell solid area fraction by sample area fraction (cell area weighted) for dispersed and flocculated alumina show similar evolutions with density. The distributions for low, intermediate and high solid volume fractions are shown for dispersed (top) and flocculated (bottom) conditions.

A distribution comparison at the three solid volume fractions reveals that there is a difference at the low and high solid volume fractions for dispersed and flocculated alumina (**Figure 66**). The low solid volume fraction dispersed alumina SAF distribution has a peak at lower SAF values (~0.75) (**Figure 66**, top). The low solid volume fraction flocculated alumina SAF distribution has a uniform distribution from approximately SAF equals 0.75 to 0.92. Since it was shown that the distributions in pore section size and cell area are similar for the low solid volume fraction dispersed and flocculated samples, the differences in the distribution of SAF must be due to differences in the association between pores section area and cell area. This must be due to the spatial arrangement of the pore sections. That association is unclear from simply looking at the distributions in SAF.

The intermediate and high solid volume fraction distributions are about the same when comparing dispersed and flocculated (**Figure 66**, middle and bottom). Although the distributions in cell area are similar for dispersed and flocculated alumina at these solid volume fractions, the distributions in pore section area are significantly different. The pore section area distribution for flocculated alumina is shifted to smaller sizes in comparison to the dispersed alumina. Again, the correlation between pore section area and cell area is unclear.

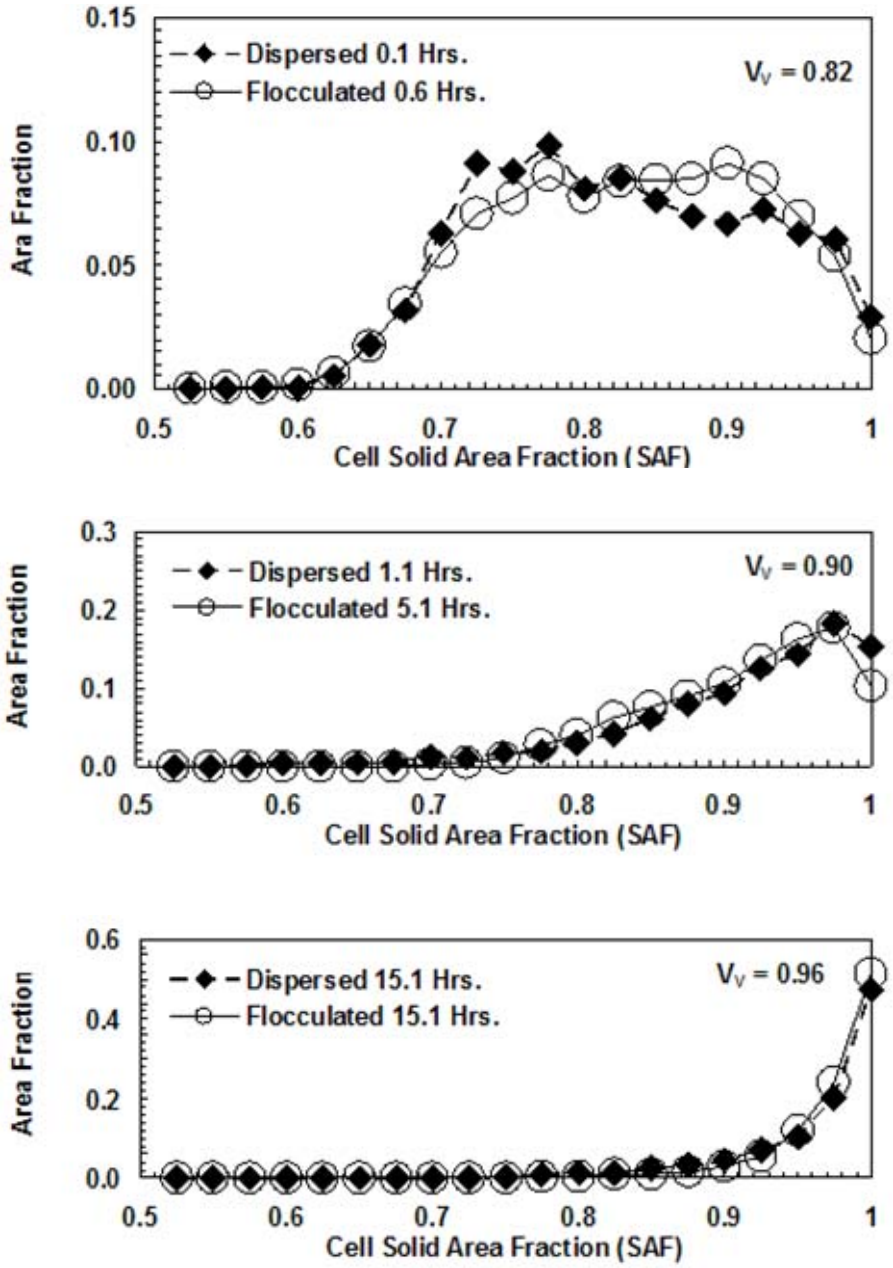

Figure 66: A comparison of the distributions at the three solid volume fractions reveals that there is a difference at the low and high solid volume fractions. The low V_V dispersed alumina distribution has a peak at lower SAF values (~0.75). The low V_V flocculated alumina distribution has a uniform distribution from approximately 0.75 to 0.92 SAF. The intermediate and high V_V distributions are about the same for dispersed and flocculated.

6.5.3 Pore Section and Tessellation Cell Area Correlation

Cell maps are employed to characterize the correlation between pore section area and cell area. **Figure 67** shows the cell maps, cell area and pore section area distributed by relative frequency by number, for dispersed and flocculated alumina at low, intermediate, and high solid volume fractions. The relative frequency by number distribution is used in this case to show a one to one correspondence between cell size and pore section size. At low solid volume fractions there is a more pronounced peak in the flocculated distribution (pore section area, PA $\approx$ 0.3 μm^2, cell area, CA $\approx$ 1 μm^2: cell solid area fraction, SAF $\approx$ 0.7) in comparison to a ridge in the dispersed distribution (PA $\approx$ 0.1 μm^2, CA $\approx$ 0.5 μm^2: SAF $\approx$ 0.8 $\rightarrow$ PA $\approx$ 0.5 μm^2, CA $\approx$ 1.5 μm^2: SAF $\approx$ 0.67). The evolution of the maps is different for dispersed and flocculated alumina due in part to the different evolutions in the pore section area distributions with increasing density. As the distribution in pore section areas for flocculated alumina shifts to smaller areas the peak may rise to absorb the additional pore sections. The distribution in pore section areas remains relatively broad in the dispersed alumina case due to the persistence of large pore sections at higher solid volume fractions. However, in addition to the changing distributions in pore section area any change in the correlation between pore section area and cell area will affect the distributions within the pore section area - cell area maps. The maps also show that large cells are associated with large pore sections throughout densification while there is an increasing distribution in the range of cell size for the smaller pore section sizes.

The diagonal lines on the maps of **Figure 67** are lines of constant SAF. The solid line running from the bottom-left to top-right corners represents SAF equal to zero. All data points must therefore lie above this line. The dotted lines are the constant SAF lines for SAF equal to the solid volume fraction for the sample. The SAF equal to the solid volume fraction line for each sample passes through the ridge or peak in the distribution for all of the samples. A large fraction of the cells have SAF $\approx V_V$.

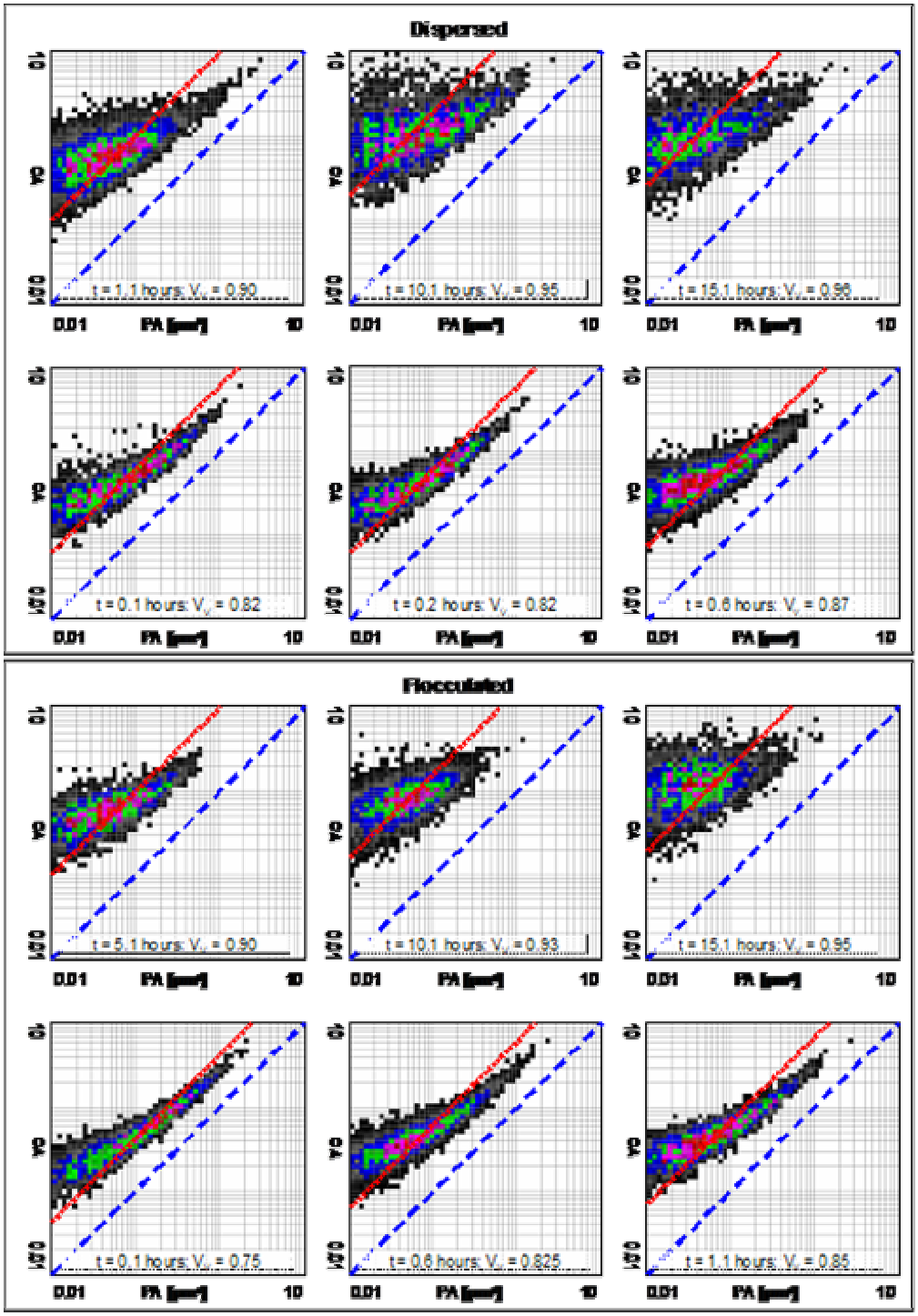

Figure 67: The above cell maps illustrate the evolution of the correlation between pore section area and cell area by number for dispersed (top) and flocculated (bottom) alumina at with time. The diagonal line from the bottom-left to top-right corners indicates cell area = pore section area. All points must be above this line. The dotted lines correspond to SAF = V_V for each sample.

6.5.4 Cell Area and Cell Solid Area Fraction Correlation

The distributions in both pore section area and cell area are best divided into logarithmic classes rather than linear classes because the distributions are either lognormal or have a similar shape. Linear classes, equal increments in area, would result in a few or one class with the majority of measurements. However, the use of the logarithmic distributions with pronounced ridges or peaks can make it difficult to interpret the cell area and pore section area maps, especially at low solid volume fractions. Therefore, cell maps using either the cell area or the pore section area and the solid area fraction will be easier to interpret. **Figure 68** and **Figure 69** show the time evolution of the cell area weighted 2-D and 3-D cell maps of the distribution of cell area with cell solid area fraction for dispersed and flocculated alumina. The dispersed and flocculated maps evolve along different paths (movement of the peak) but, become similar at high solid volume fractions (longer times). At the low solid volume fraction, the flocculated distribution has a sharp peak at intermediate cell areas and high solid area fraction (CA ≈ $0.04\mu m^2$, SAF ≈ 0.87) while the dispersed has more of low peak at larger cell area and lower solid area fraction (CA ≈ $1\mu m^2$, SAF ≈ 0.75). The flocculated alumina has a small fraction of large cells with low SAF in comparison to dispersed alumina at the low solid volume fraction. At the high solid volume fraction dispersed and flocculated alumina have large peaks at high SAF (SAF > 0.95) and large cell areas ($CA_{Dispersed} \approx 4\ \mu m^2$; $CA_{Flocculated} \approx 2\ \mu m^2$) due to large cells containing small pore sections. This may partly be due to increased pore spacing as a result of pore elimination and the observed grain growth. Additionally, in the case of dispersed alumina the larger cells with low SAF persist until high solid volume fraction while they are eliminated in the flocculated case.

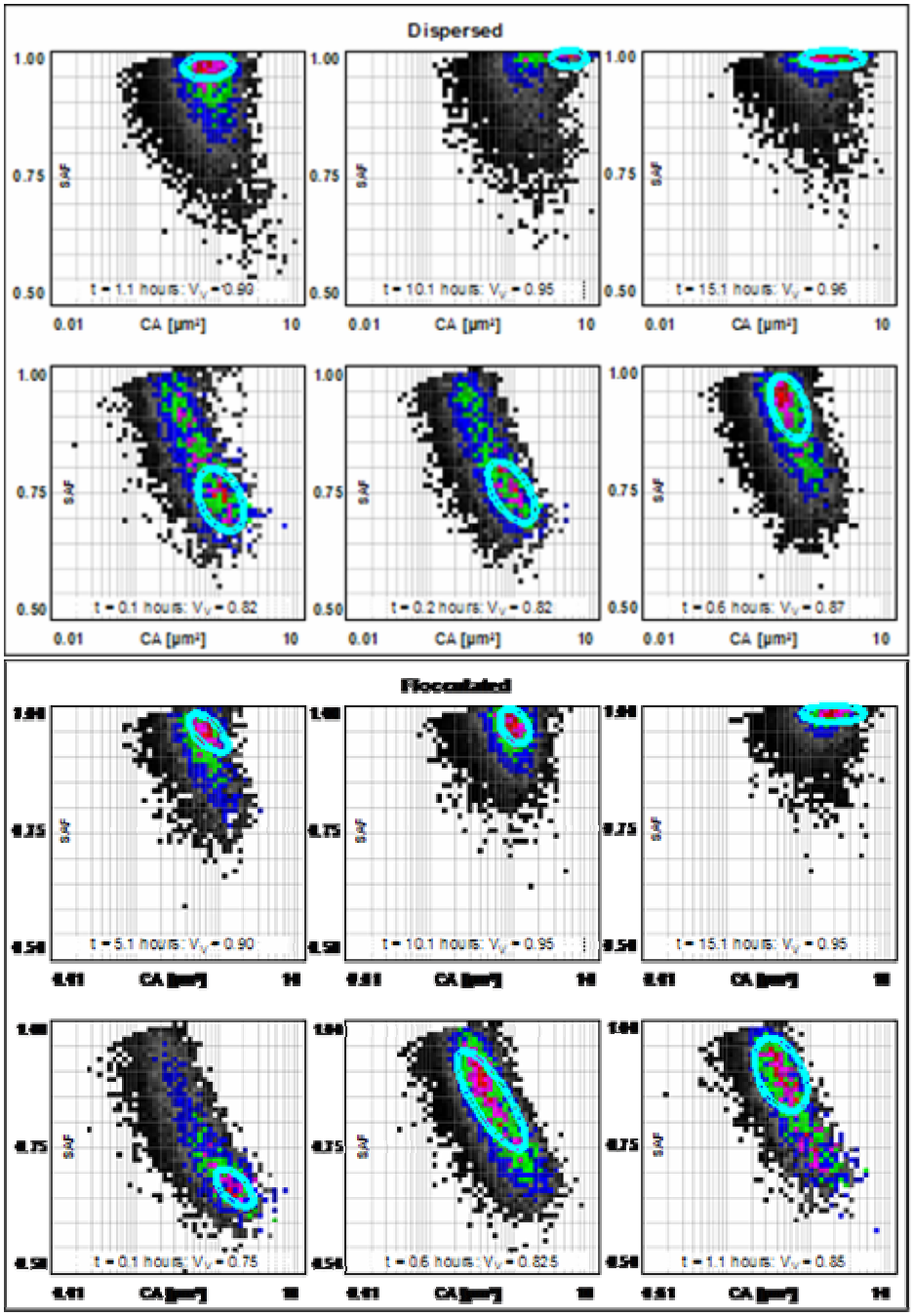

Figure 68: The ovals in the CA-SAF cell maps identify the positions of the peaks in the distributions. At the low solid volume fraction (dispersed 0.1 hours, flocculated at 0.6 hours) there is a significant difference in the location of the peaks. However, at higher solid volume fractions the maps for dispersed and flocculated alumina become similar.

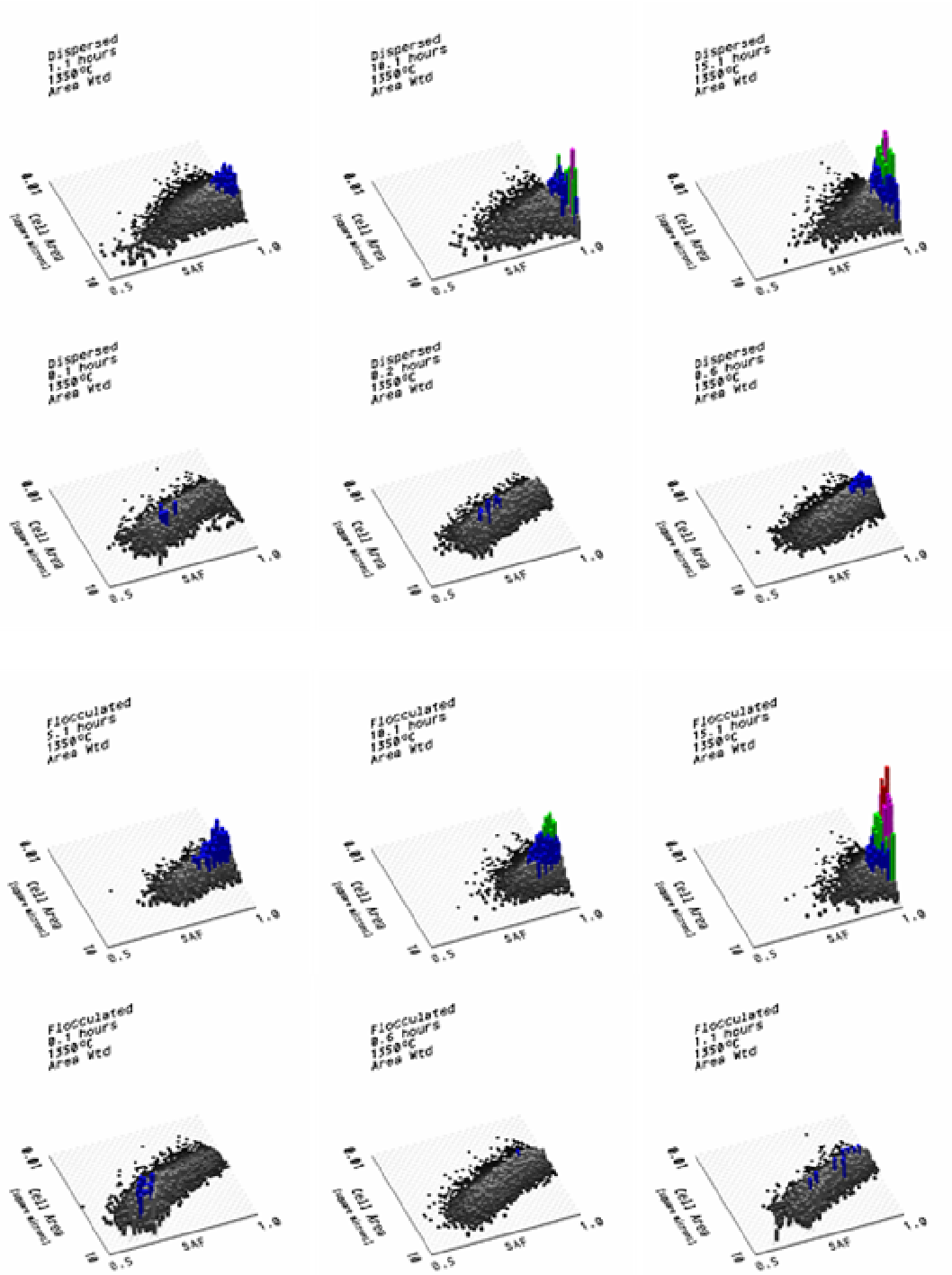

Figure 69: Three-quarter views of the CA-SAF-CAW distributions shown in Figure 68 help to visualize the evolution of the maps with time at temperature.

6.5.5 Pore Section Area and Cell Solid Area Fraction Correlation

The effects of the evolution of the pore section area distributions on the SAF maps are amplified in the cell area weighted, pore section area (PA) – cell solid area fraction (area fraction) cell maps of **Figure 70**. The distribution by area fraction is used to emphasize the portion of the materialographic section associated with the cells of the specific properties. Only the distributions for dispersed and flocculated alumina at low, intermediate and high solid volume fractions are shown to minimize confusion. The effect of the narrowing of the pore section area distribution in the flocculated samples results in a narrowing of the distribution along the 'x-axis' which increases the frequencies in the classes associated with small pores and high SAF for the high solid volume fraction. It cannot be concluded however, that the evolution of the pore section area distributions are solely responsible for the changes in cell solid area fraction distributions.

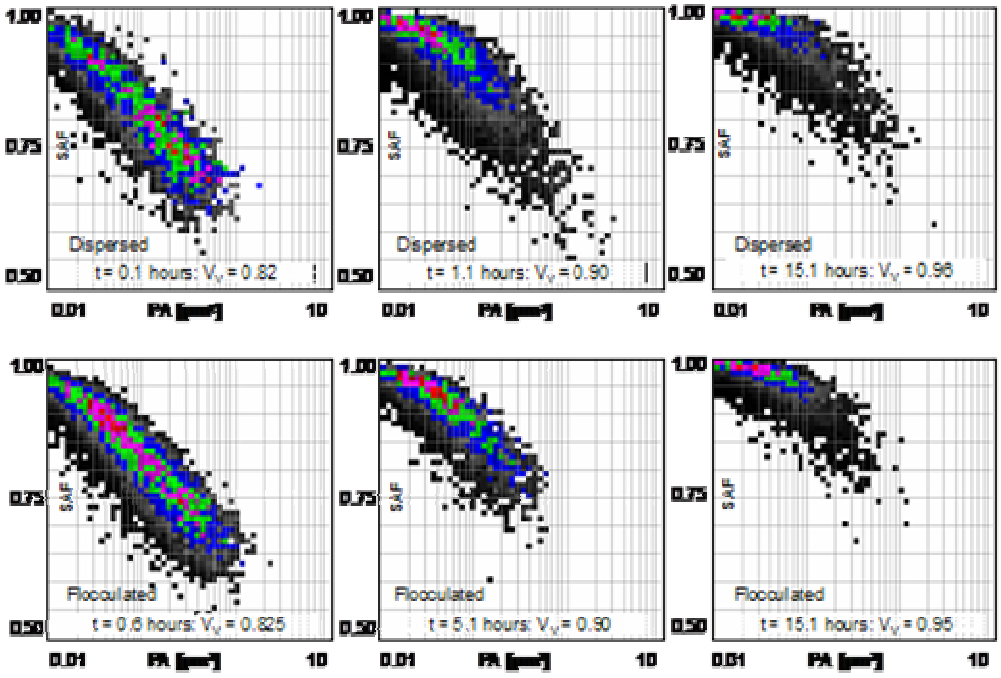

Figure 70: The pore section area and cell solid area fraction weighted by cell area (PA-SAF-CAW) cell maps for dispersed (top row) and flocculated (bottom row) alumina at low (left), intermediate (middle) and high (right) solid volume fractions are shown above. In this case effect of the narrowing of the pore section area distribution in the flocculated samples results in a narrowing of the 3-D distribution along the 'x-axis' which increases the frequencies in the bins associated with small pores and high SAF at high V_V.

6.5.6 Tessellation Cell Morphology

Similar pore section area distributions and cell area distributions for dispersed and flocculated alumina were observed at low solid volume fractions. The cell solid area fraction and the associated cell maps are sensitive to the arrangement of pore sections within the microstructure. The shape of the tessellation cells may also be sensitive to the arrangement of pore sections. However, the shape factor distributions for tessellation cells show little evolution with density (Figure 71). In all cases the section morphology is relatively equiaxed (peaks at $Q \approx 0.7$). Also, a comparison between dispersed and flocculated shape factor distributions shows that the distributions are similar at any given density (Figure 72).

The next step is to look for correlations between cell size and morphology using cell maps. **Figure 73** show the cell maps for cell area and cell Q. Unlike the previous cell maps in this section, the cell maps of cell area and cell Q weighted by cell area, are similar at each solid volume fraction. The position ($CA \approx 0.5\ \mu m^2$, $Q \approx 0.7$) and height of the peak ($A_A \approx 0.01$) for the dispersed and flocculated alumina at low solid volume fractions are very similar. As density increases the peaks shift to large cell sizes due to cell area growth ($0.5 \rightarrow 0.8 \rightarrow 1.5\ \mu m^2$) while the position of the peak in terms of Q remains at about 0.7. The height of the peaks remains relatively constant from low to intermediate to high solid volume fractions for the dispersed alumina ($0.009 \rightarrow 0.011 \rightarrow 0.009$). The height of the flocculated peaks increases from low to intermediate solid volume fractions and remains higher ($0.010 \rightarrow 0.019 \rightarrow 0.014$) relative to the dispersed peaks. Therefore, the cell area – cell Q maps may not be sensitive to spatial arrangements.

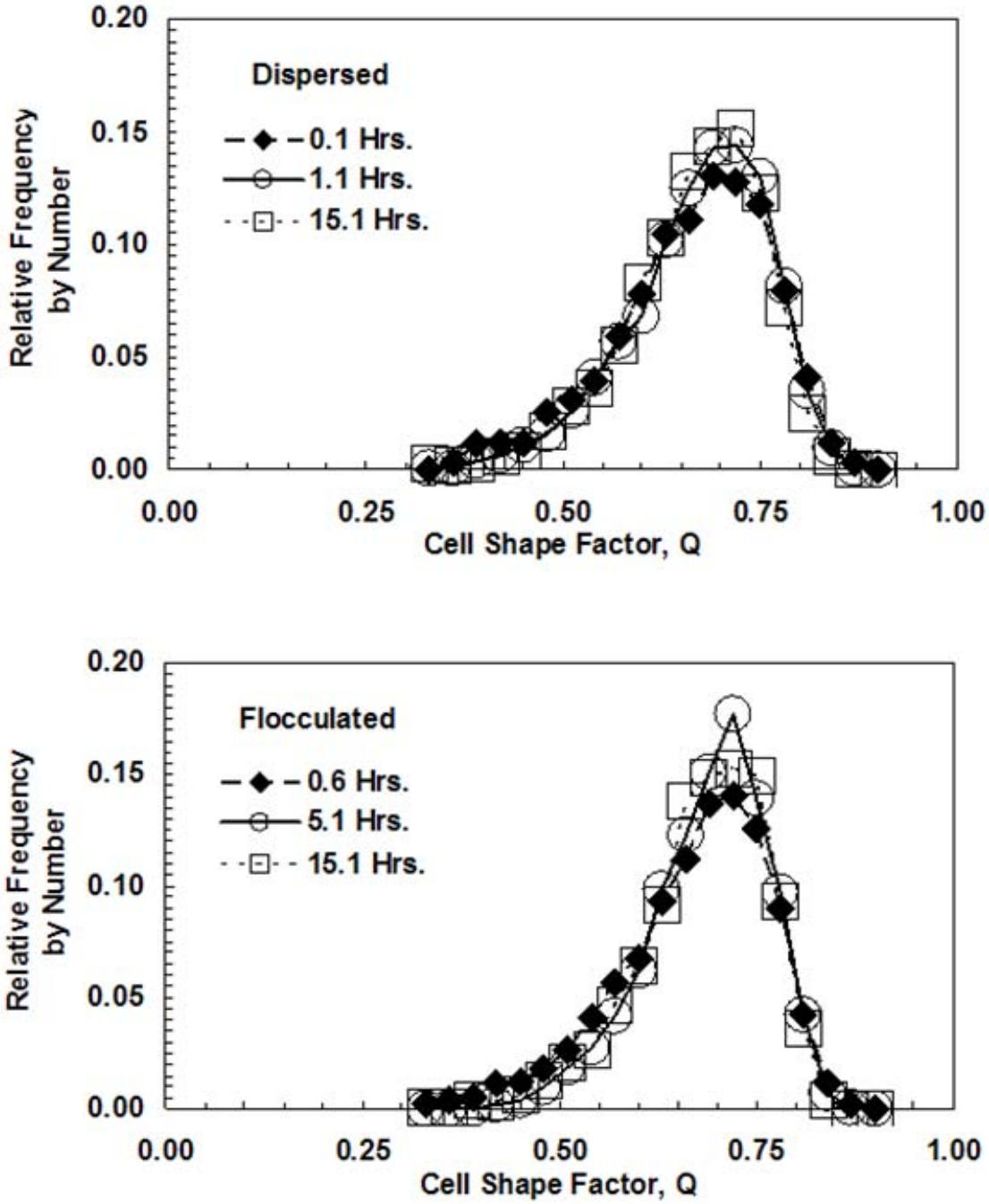

Figure 71: The distributions in cell shape factor for both dispersed and flocculated alumina show little evolution with increasing density. However, there is a slight narrowing of the distribution with density.

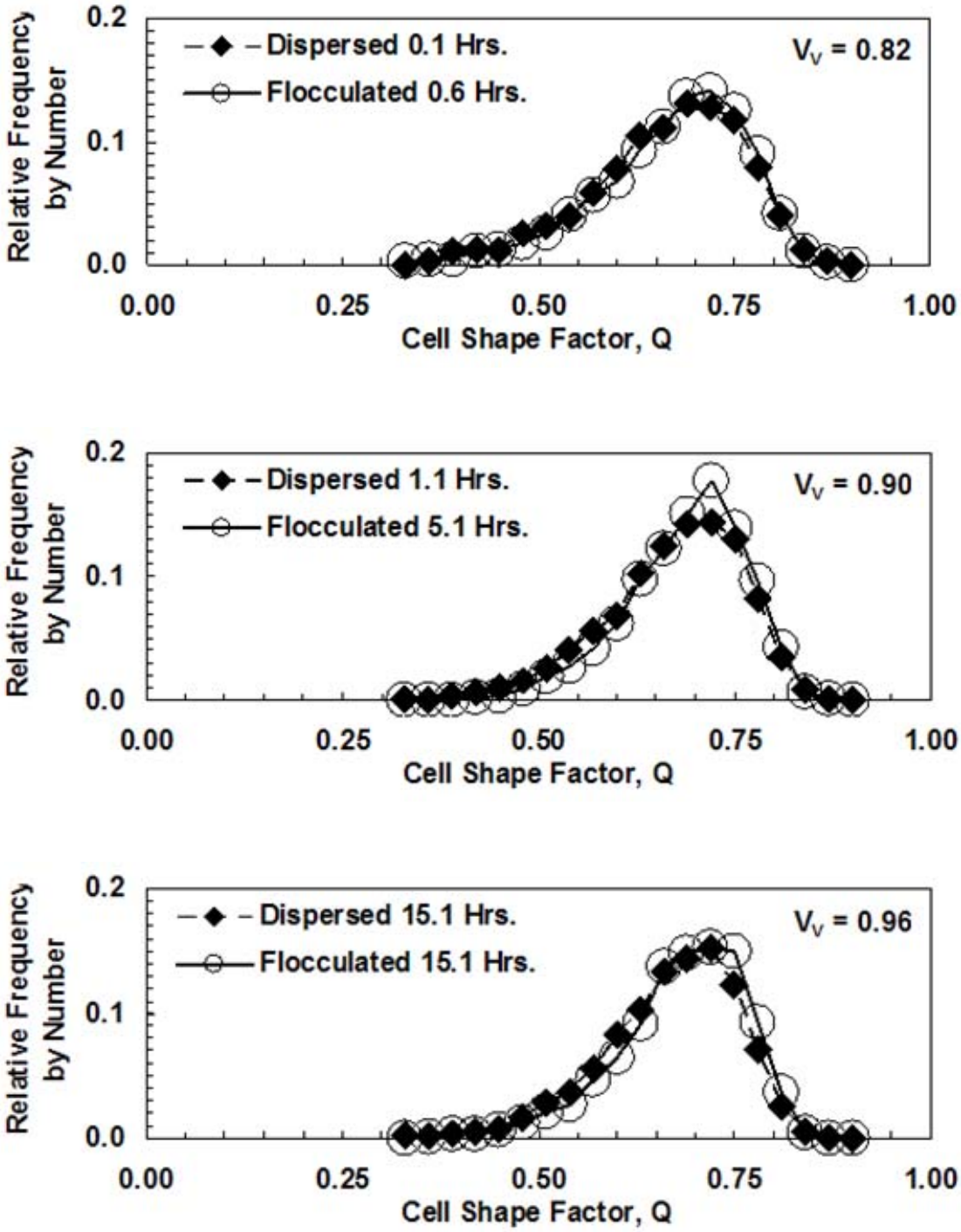

Figure 72: The distributions in cell shape factor are similar for flocculated and dispersed alumina at similar solid volume fractions.

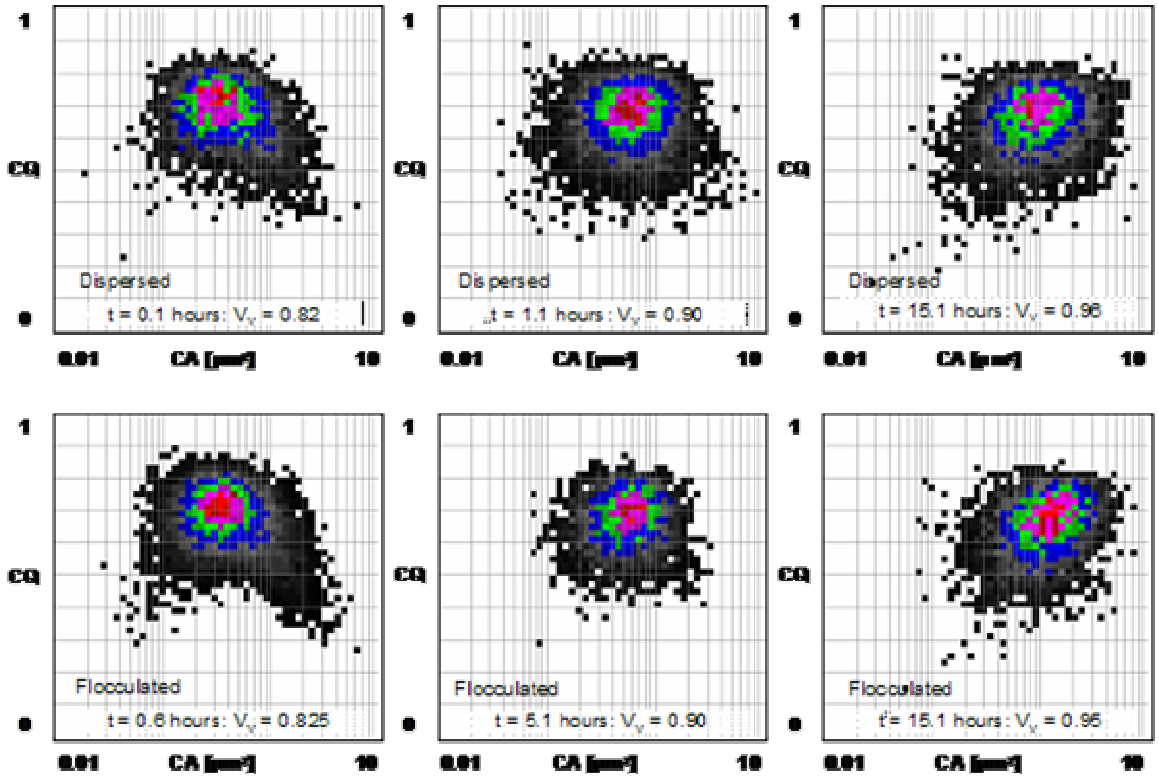

Figure 73: The cell maps for cell area and cell Q weighted by cell area are similar at each solid volume fraction for dispersed and flocculated alumina.

6.6 TESSELLATION AND THE LOCAL ENVIRONMENT

6.6.1 Cell (Pore) 2-D Coordination Number

The number of neighboring tessellation cells, the two-dimensional coordination number (CN), was determined for the dispersed and flocculated alumina samples. As expected for a two-dimensional tessellation, the mean number of neighbors is approximately six. There is little evolution in the coordination number with changes in density for the alumina samples studied in this work (Figure 74). Additionally, there is no significant difference between dispersed and

flocculated distributions. Due to the similarity and limited range of cell coordination numbers, the cell maps created using CN are very similar and inconclusive.

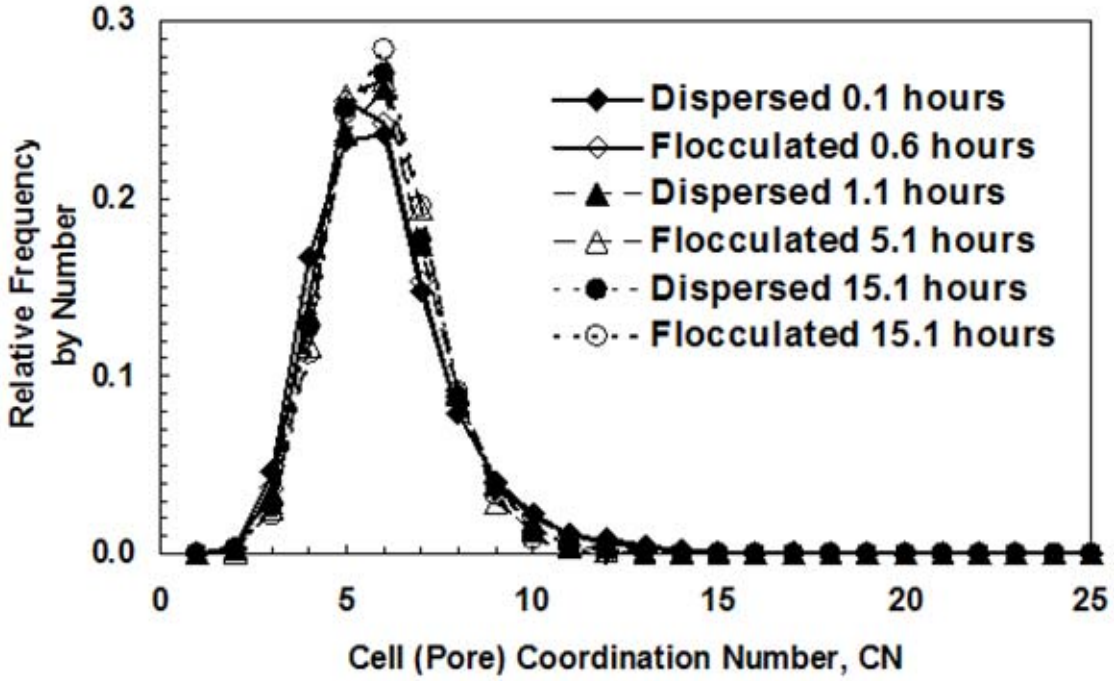

Figure 74: Distributions in cell 2-D coordination number for low, intermediate and high solid volume fractions of both dispersed and flocculated alumina. There is little change in the distributions with changing density and little difference between dispersed and flocculated samples.

6.6.2 Local Mean Pore Section Area

The local mean pore area (LPA) is the average pore section area associated with coordinated cells. It does not include the size of the pore section in the cell that the LPA is associated with. It is a measure of the local environment beyond the cell boundary of the pore section. The pore section area of each pore is involved in the calculation of LPA as many times as it has coordinated cells. However, the evolution of the distribution of LPA is not completely independent of the distribution in pore section areas. As the distribution in pore area shifts to smaller values as in the case of the flocculated alumina samples, the LPA distribution will also shift to smaller pore section areas. **Figure 75** shows the evolution of the distributions in LPA for both the dispersed and flocculated samples. It is apparent that the LPA distribution for the

dispersed samples also shifts to smaller pore section sizes. The comparison of the distributions of LPA for dispersed and flocculated at similar solid volume fractions is given in **Figure 76**. The distributions by relative frequency are similar between dispersed and flocculated alumina at each density. This is expected since there was little difference between the distributions in pore section area by relative frequency.

Analysis of the cell maps of pore section area (PA) and local mean pore section area (LPA) at low, intermediate, and high solid volume fractions (**Figure 77**) reveals differences in the correlation between the pore and local mean pore area distributions. The peak in the PA-LPA relative frequency map for dispersed alumina remains in about the same position (PA $\approx 0.02\mu m^2$, LPA $\approx 0.1\mu m^2$) until 15.1 hours when the peak begins to move to lower values of LPA. The flocculated alumina peak stays at about the same PA ($0.02\mu m^2$) throughout densification but, continuously moves to lower LPA (LPA ≈ 0.2 to $0.03\mu m^2$) values as density increases. At the low solid volume fraction, the dispersed alumina distribution has a broader peak in comparison to the flocculated alumina distribution. Since the distributions in pore section area are similar for dispersed and flocculated alumina at this density, the lower peak in the flocculated PA-LPA map suggests that there is a broader distribution in LPA for each PA. At the intermediate and high solid volume fractions, the peak in the flocculated alumina maps are higher than those of dispersed alumina. This is partly due to the narrowing and shifting of the flocculated alumina pore section area distribution while the dispersed alumina distribution peak remains at approximately the same pore section area through densification.

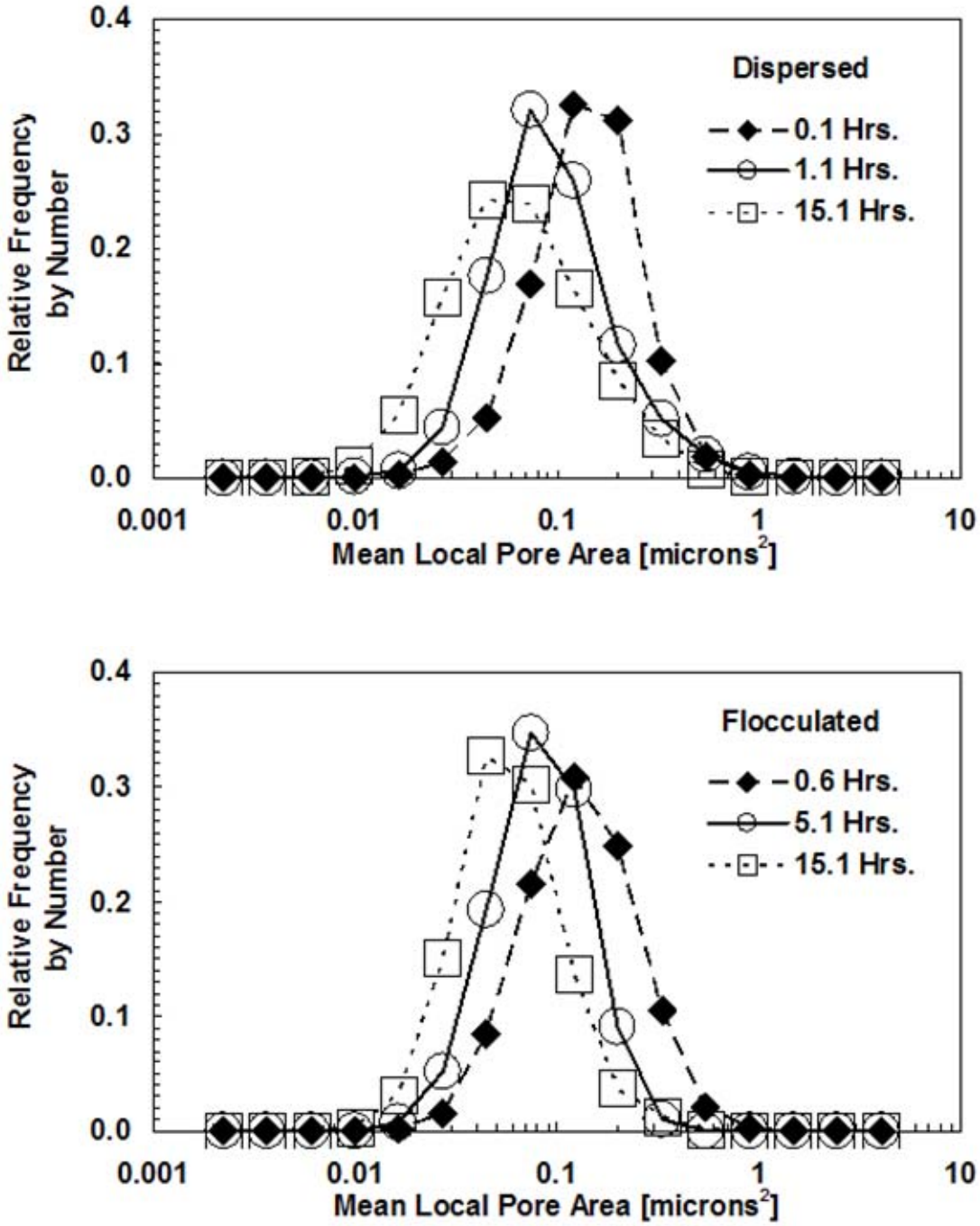

Figure 75: The distributions in mean local pore area evolve in a manner similar to that of the pore section area distribution. The evolution of the LPA distribution is not independent of the evolution of the pore section area distribution.

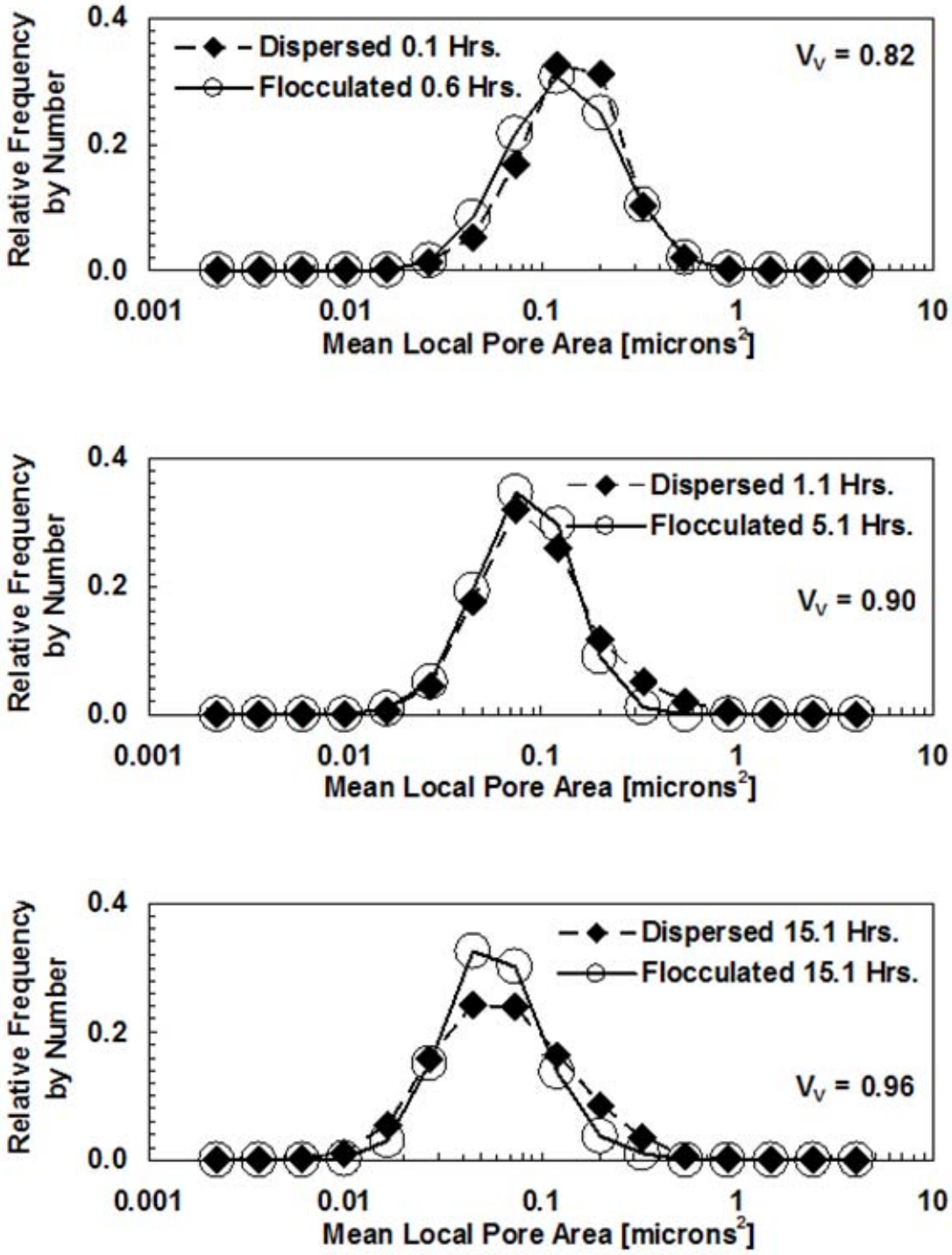

Figure 76: A comparison of the LPA distributions at similar solid volume fractions for dispersed and flocculated alumina indicate that the distributions are similar at low solid volume fraction but, evolve differently with increasing density.

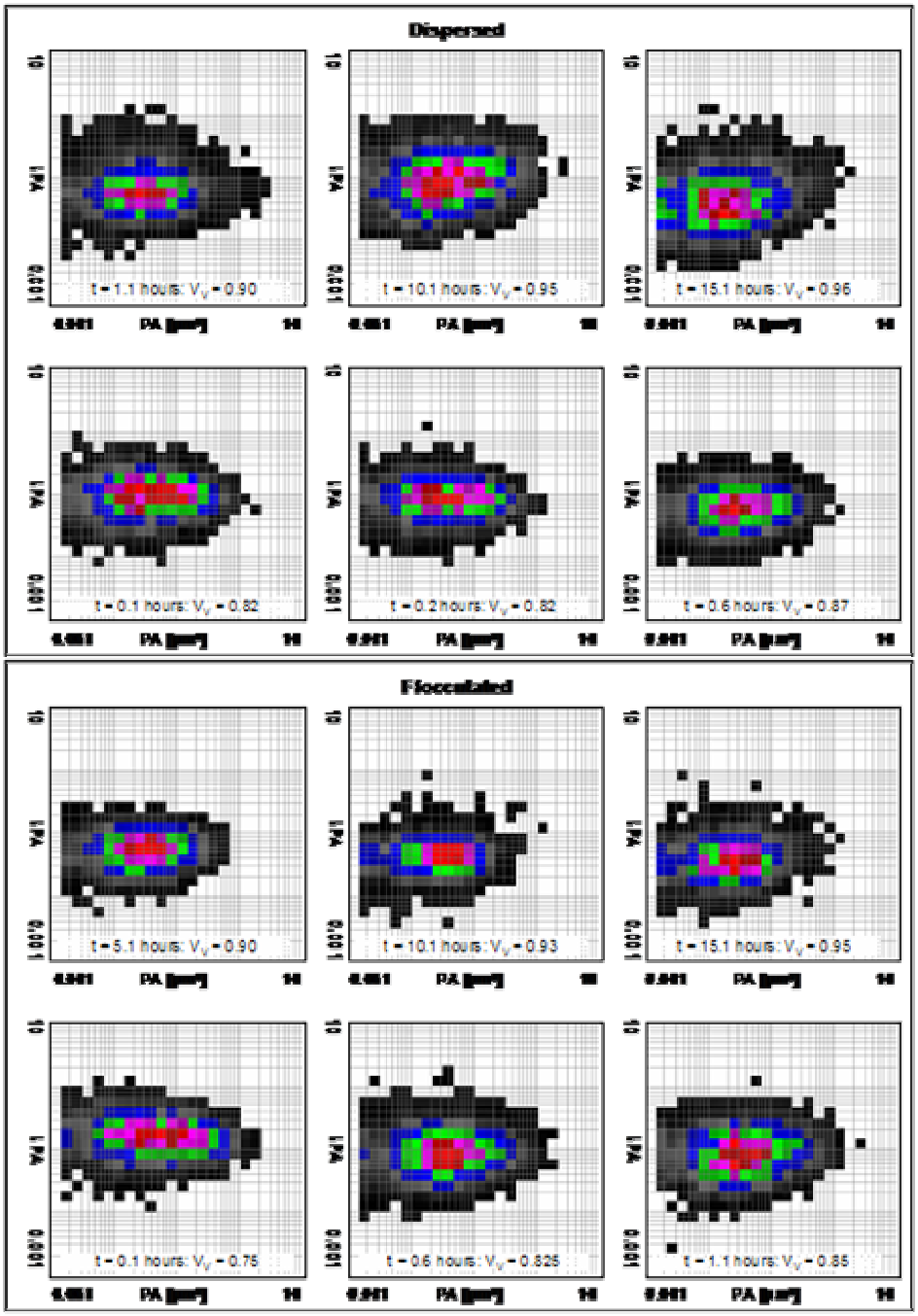

Figure 77: The peak in the PA-LPA relative frequency map for dispersed alumina remains in about the same position (PA ≈ 0.02μm^2, LPA ≈ 0.1μm^2) until 15.1 hours when the peak begins to move to lower values of LPA. The flocculated alumina peak stays at about the same PA (0.02μm^2) throughout densification but, continuously moves to lower LPA (LPA ≈ 0.2 to 0.03μm^2) values as density increases.

6.7 RESULTS SUMMARY

The following is a summary of the results of this work section by section to bring out points relevant to the discussion:

Section 6.1 : Stereological Measurements and Dimensionless Parameters

- The effect of particle packing due to flocculation, on the microstructural evolution of alumina sintered at 1350°C is apparent in the relative density versus time curve. The densification rate for times at temperature ranging from 0.1 hours to 15.1 hours the densification rate in flocculated alumina was higher than dispersed alumina. The logarithmic densification rate constant for flocculated alumina is 25% greater than for dispersed alumina although the density at times within this range are higher for dispersed alumina. However, at solid volume fractions within the range from 0.8 to 0.96, the densification rate as a function of density was higher in the dispersed alumina. These results are consistent with those of Sacks and Yeh[18]. They observed a difference in densification rates of about 15% with time for the flocculated alumina but higher densification rates for dispersed as a function of density through a similar density range.
- It was found that the solid-vapor surface area per unit volume was similar for dispersed and flocculated alumina sintered at 1350ºC as function of density. If the driving force for densification is dependent on the free energy associated with pore-solid interface (contact flattening), a comparison of microstructure parameters at similar densities should reveal the effects of microstructure on densification rate.
- Dimensionless Microstructural Pathways (DMPs), surface area ratio and intercept ratio versus solid volume fraction, for dispersed and flocculated alumina followed the same path during densification. The surface area ratio and the intercept ratio did not reveal any differences between the evolution of the flocculated and dispersed alumina microstructures as well as differences between computer simulation of spherical particles of equal size and a distribution in size as a function of density.
- The link between grain growth and mean pore spacing was examined using the ratio of the mean pore spacing to mean grain intercept length. Despite concomitant

increases in the mean pore spacing and the mean grain size, the ratio increased due to a faster increase in the spacing. This revealed that the evolution in pore spacing could not be entirely attributed to grain growth.

- Section 6.2 : Grain Size Evolution
    - The estimation of the 'true' grain size distribution by the application of a statistical unfolding method based on the methods of Saltykov and others revealed that the distributions were similar at any solid volume fraction throughout the densification range. Therefore, coarsening in the flocculated alumina does not occur as it does at higher temperatures.
    - The effect of particle/grain shape assumption on the resulting unfolded grain size distributions was examined for several polyhedra. It was found that although there was a significant effect on the magnitudes of the mean grain size, the trends in the evolution of the grain size distribution were still revealed.
- Section 6.3 : Section Size Evolutions
    - The distributions in size of grain and pore section areas were examined as well the distribution in size of the tessellation cell. Both the grain section and tessellation cell area distributions were similar when comparing the distributions for dispersed and flocculated alumina at similar solid volume fractions. However, the pore section area distributions evolved differently for dispersed and flocculated alumina. At low solid volume fractions the distributions were similar but at intermediate and high solid volume fractions the dispersed and flocculated distributions diverged. The dispersed alumina distribution broadens with little change in the position in the peak through intermediate stage while the flocculated distribution narrows and the peak shifts to smaller pore section area.
    - The differences in the pore section area distributions were not sufficient to explain the differences in densification rates between dispersed and flocculated alumina. The distributions at low solid volume fractions were similar when comparing dispersed and flocculated alumina. If the pore section area distribution was directly related to the differences in densification rates, the distributions would have been most different

at the low solid volume fractions when the differences in densifications rates were actually the highest observed.

- Section 6.4 : Feature Morphology
    - Grain and pore section morphology was investigated to determine if the variations in the arrangement of particles due to casting conditions had any effect on size – morphology relationship which may be responsible for the different densification rates. It was found that like the evolution in grain size, the distributions in the shape factor Q for both the grain and pore sections were similar when comparing the distributions for dispersed and flocculated alumina at similar solid volume fractions.
    - The correlations between grain section size and grain section shape factor were examined using cell maps. The maps of grain section area with grain shape factor were similar for dispersed and flocculated at each solid volume fraction and showed little evolution through intermediate stage sintering. The maps for pore section area with pore shape factor did show different evolutions for dispersed and flocculated alumina due primarily to the different evolutions in pore section area.
    - An important aspect of the distributions in pore shape factor is the presence of large pore sections with low Q values. These are large anisotropic pore sections. They persist in the dispersed alumina until the final stage of sintering while they are removed from the flocculated alumina with increasing solid volume fraction.
- Section 6.5 : Tessellation and the Immediate Environment
    - The immediate environment of a feature (pore section) is defined as the environment within the boundaries of the tessellation cell. This environment was characterized by the distributions of pore section and cell areas, the cell solid area fraction, cell shape factor, and the correlations between these parameters. It was found that the cell solid area fraction distributions for dispersed and flocculated alumina were only modestly different at low solid volume fractions (when the densification rates differ the most for dispersed and flocculated) but evolved into similar distributions at intermediate and high solid volume fractions. However, it is unclear how the distribution in the cell solid area fraction alone relates to the spatial distribution of pore sections and grains.

- The 2-D and 3-D maps for pore section and cell areas illustrate the one to one correspondence between cell size and pore size. Differences between the distributions for dispersed and flocculated alumina at similar solid volume fractions are seen.
- The correlations between pore section area and cell area can also be made using cell maps based on cell area or pore section area with the cell solid area fraction. The maps for cell area and cell solid area fraction weighted by cell area (section area fraction) show differences in the correlation between the pore and cell areas for dispersed and flocculated at the low solid volume fraction when the densification differ the most. The use of distributions by area fraction emphasizes the fraction of the materialographic section associated with cells having a certain cell area and cell solid area fraction (pore section area indirectly), rather than the number of cells.
- The cell maps using the pore section area and the cell solid area fraction do not provide additional information not already available from the pore section area – cell area maps and the cell area – solid area fraction maps.
- The distributions in cell shape factor alone were similar for dispersed and flocculated at all solid volume fractions. The overall distribution in shape factor remained relatively constant throughout the densification range. Cell maps for cell area and cell shape factor weighted by area fraction did not show significant differences between dispersed and flocculated at any solid volume fraction except that the peaks were higher than for the dispersed alumina.

- Section 6.6 : Tessellation and the Local Environment
  - The next level of spatial distribution is the local environment which is defined as the environment associated with nearest neighbor cells in the tessellation. The parameters used do not include properties of the cell at the 'center' of that environment. The distributions of cell (pore) two dimensional coordination numbers were analyzed and showed little difference between dispersed and flocculated alumina or at similar solid volume fractions. Also, the narrow range of coordination numbers is not well suited to cell maps and the results were not presented.
  - The local mean pore section area is the arithmetic mean of the pore section areas in nearest neighbor cells and does not include the area of the pore contained within the

‘center’ cell. At each solid volume fraction, the PA – LPA maps show differences between dispersed and flocculated alumina. The location of the peak in the flocculated alumina maps remained at a relatively constant pore section area, similar to the dispersed alumina. However, the flocculated alumina peak continuously moved to lower mean local pore section areas while the dispersed alumina remained at the same mean local pore section area. Since there is a large difference in the pore section area distributions between dispersed and flocculated at high solid volume fractions, there is also a significant difference in the local mean pore section area distributions.

7.0 DISCUSSION

7.1 DENSIFICATION

The casting condition of alumina powder can have a dramatic effect on densification behavior as previously described in the literature[17,18,35,36,55-65] and as demonstrated in this work (Figure 78). Specifically the degree of dispersion or flocculation in the slip prior to casting affects the initial (green) density and the subsequent densification rate. In the following discussion it should be recognized that the results of this study may not be representative of other flocculation states. In this study the solid volume fraction for dispersed alumina (0.82) at 0.1 hours at 1350°C was approximately 7% higher than that of flocculated alumina (0.75) held at 1350°C for 0.1 hours. Despite having a lower density at 0.1 hours the flocculated alumina achieved the same density (V_V ~0.96) as the dispersed alumina after 15.1 hours at temperature. It was shown that the densification rate at any given time during the intermediate stage of sintering (V_V below ~0.9) was higher in the alumina samples cast in the flocculated condition relative to the dispersed alumina. The surface areas per unit volume were calculated for each sample and revealed that dispersed and flocculated alumina had the same solid-vapor interfacial area per unit volume (S_V^{SV}) at any solid volume fraction within the range of intermediate stage of sintering. Also, there was a linear decrease in S_V^{SV} with increasing solid volume fraction. Therefore, since the solid volume fraction is higher for dispersed alumina in comparison to flocculated alumina at any time within the intermediate stage, the S_V^{SV} is lower for dispersed alumina at any time within the intermediate stage. If the driving force for densification is due to the reduction in surface free energy associated with the solid-vapor interface (free surface) then the densification rate for flocculated alumina should be higher than that of the dispersed alumina. This is

1consistent with the results. However, since the S_V^{SV} is the same at a given solid volume fraction within intermediate stage sintering, the densification rates should be equal for dispersed and flocculated alumina. This is not the case as the densification rate is higher for dispersed alumina in that range of densities. This suggests that at least two processes or mechanisms are responsible for the densification behavior of slip-cast alumina sintered at 1350°C.

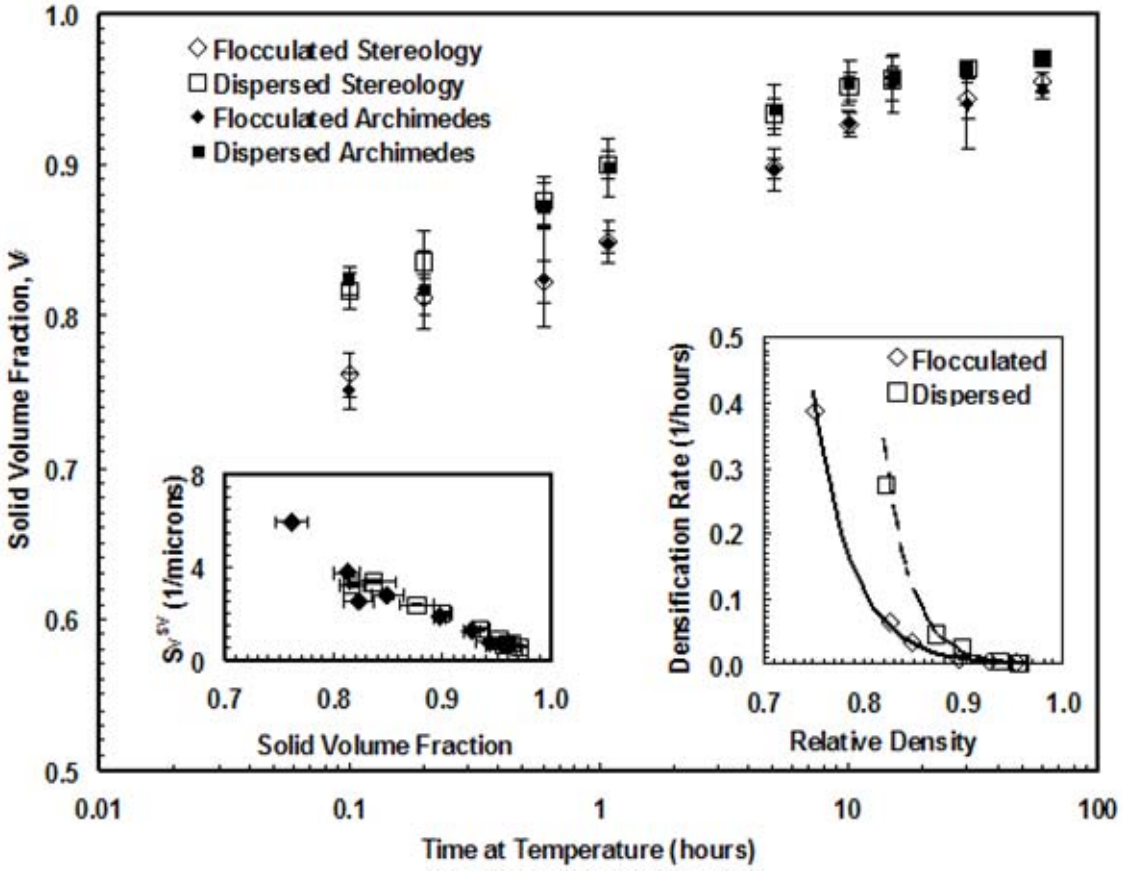

Figure 78: Solid volume fraction, densification rate, and solid-vapor surface area per unit volume for dispersed and flocculated alumina. (Previous figures repeated for convenience).

7.2 PORE SIZE AND SPACING EVOLUTION

The effect of the degree of dispersion on the packing of the powder particles in the cast should result in microstructural differences between dispersed and flocculated alumina. At the very least this should be evident during the early stages of sintering. Initial investigations into the cause of the differences in densification rates focused on the evolution of average properties of the microstructure. The average properties studied included the solid-solid (grain boundary) and solid-vapor (pore-grain) interface surface area per unit volume along with stereological and derived parameters based on the surface areas per unit volume. The stereological parameters included mean pore intercept length, mean pore spacing, and mean grain intercept length. The derived parameters included the Dimensionless Microstructural Pathways of the surface area ratio, intercept ratio, and intercept length-spacing ratio. In all cases the parameters revealed no significant difference between the dispersed and flocculated microstructures. Of interest in this discussion is the evolution of the mean pore intercept length and spacing (Figure 79). The mean pore intercept length remained approximately constant and equal for dispersed and flocculated alumina (~0.2μm) throughout the densification range observed. The pore spacing increased with increasing density due to grain growth and/or the elimination of pores. One could conclude that either these average parameters are not sensitive to the differences in microstructure due to casting condition or there are no differences.

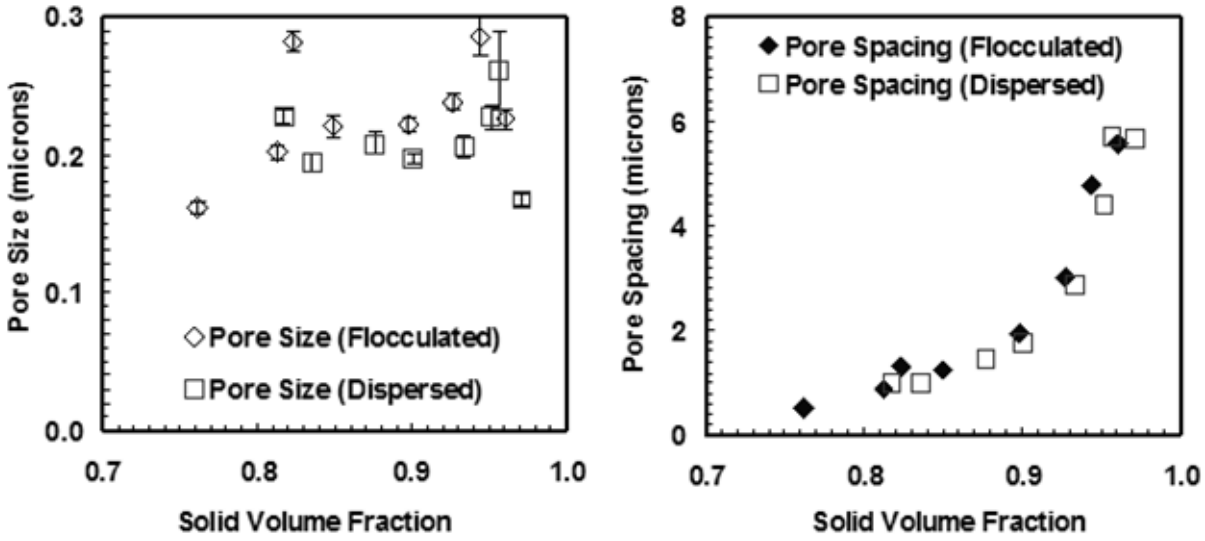

Figure 79: Mean pore intercept length and mean pore spacing for dispersed and flocculated alumina. (Previous figures repeated for convenience).

7.3 GRAIN SIZE EVOLUTION

Since average microstructural parameters did not reveal any differences in the microstructures between dispersed and flocculated alumina at similar solid volume fractions, the next step was to determine the distributions in microstructural features of the samples. The three dimensional grain size distributions were determined from the two dimensional section data obtained from the materialographic sections using the modified inverse method using information entropy based class boundaries. To improve the representation of the 3-D distributions an information entropy based method of determining class boundaries was developed. It was found that the distributions in grain size were similar at similar solid volume fractions and similar times at temperature. Grain growth was gradual and flocculation appeared to have little effect on the evolution of the distributions (Figure 80). This is significantly different to previous experiments performed on alumina at higher temperatures[17]. At higher temperatures

there is pronounced grain growth and a significant difference in the evolutions of dispersed alumina and flocculated alumina grain size.

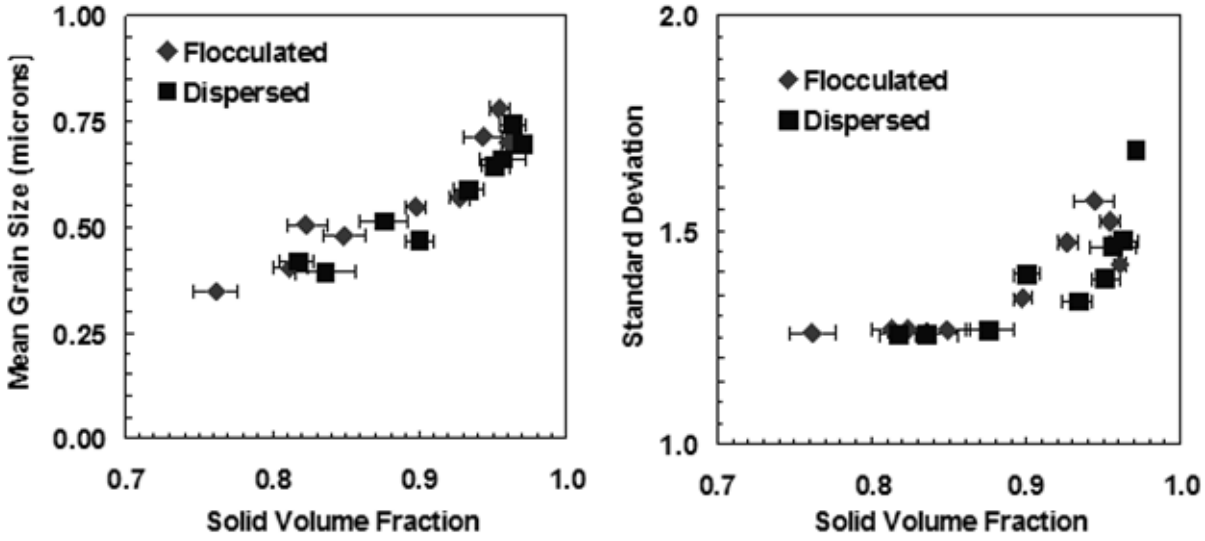

Figure 80: Three-dimensional grain size distribution parameters (lognormal distributions) for dispersed and flocculated alumina. (Previous figures repeated for convenience).

7.4 PORE SIZE DISTRIBUTION EVOLUTION

The absence of any significant effect of flocculation on grain growth in conjunction with the similarities observed for the evolution of the other microstructural parameters with solid volume fraction continue to promote the idea that there are no microstructural differences between the dispersed and flocculate alumina due to casting condition. However, differences are observed in the evolution of the pore section area distributions for dispersed and flocculated alumina (Figure 81). At the lowest common solid volume fraction, 0.82, the distributions in pore section area are very similar between the dispersed and flocculated alumina. However, as density increases differences in the distributions emerge. The dispersed alumina retains a larger population of larger pore sections (above 0.3μm^2) relative to the flocculated alumina. However,

if the differences in the densification rates at different solid volume fractions during intermediate stage sintering are due to the differences in the pore section distribution, the densification rates should be similar at a solid volume fraction of 0.82. The opposite is true, the densification rates differ the greatest at this solid volume fraction (Figure 78).

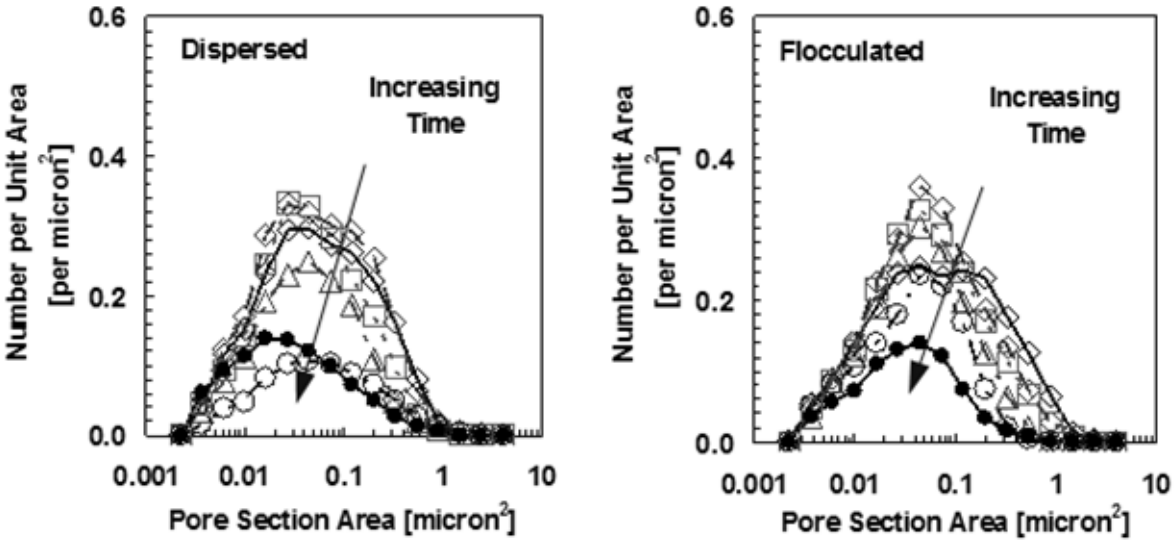

Figure 81: Pore section area distributions for dispersed and flocculated alumina. (Previous figures repeated for convenience).

7.5 FEATURE MORPHOLOGY

Another aspect of microstructural features which may contribute to differences in behavior is their morphology. The distributions in grain and pore section size at similar solid volume fractions may be similar for dispersed and flocculated alumina but, their morphologies may differ due to the initial packing arrangement of particles in the cast. However, the distributions in shape parameters for grain and pore sections did not reveal any significant differences between dispersed and flocculated alumina through the intermediate stage. The correlations between size and shape were also investigated and only revealed differences

between dispersed and flocculated which are likely due to the differences in pore section area distribution (Figure 82).

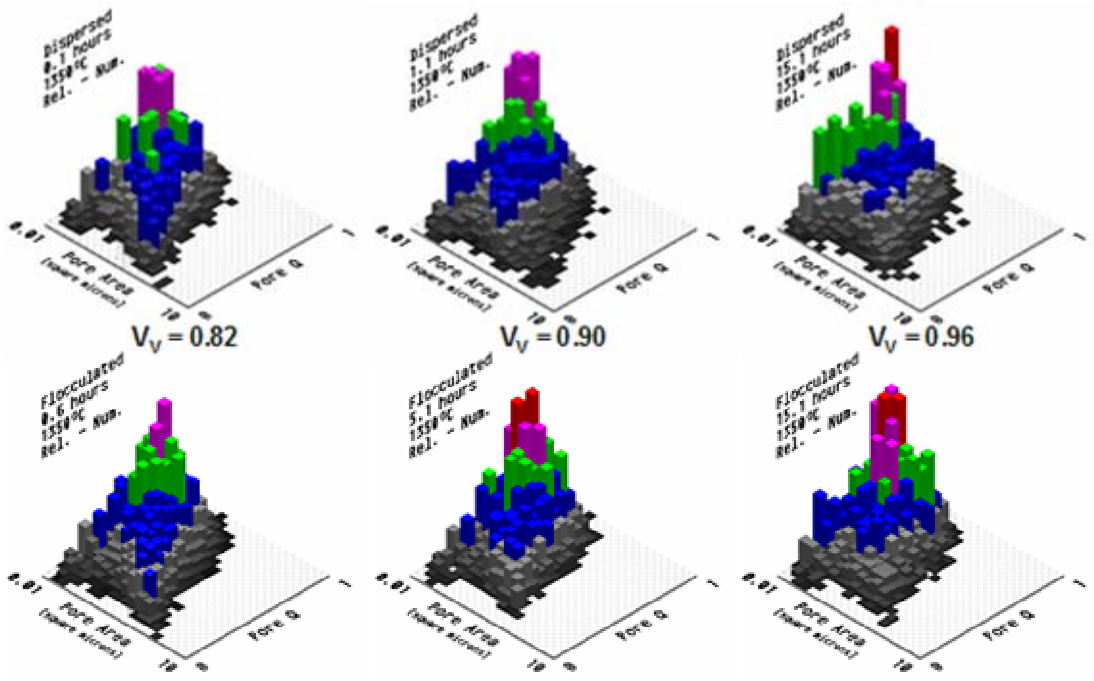

Figure 82: Evolution of the pore section area – pore shape factor maps for dispersed and flocculated alumina. The dispersed alumina maps do not show any significant change until final stage is reached. In final stage the frequency of small pore sections with low Q values increases. In the flocculated alumina the distribution in pore section areas narrows and shifts to small sizes resulting in a 'squeezing' of the peak toward smaller sizes.

7.6 MEAN PORE INTERCEPT LENGTH

There is an apparent inconsistency between the constant mean pore intercept length throughout densification while the pore section area distribution for flocculated alumina evolves to smaller section areas. The mean pore intercept length for dispersed alumina is also relatively constant throughout intermediate stage sintering but the distribution in pore section size seems to

reduce proportionally. The proportional removal of pore sections from all sizes would be consistent with a constant mean pore intercept length. The apparent inconsistency for flocculated alumina is resolved by taking into consideration the pore section morphology. Intercept lengths will depend on shape as well as size. For example, large rectangular pore sections may have similar mean intercept lengths to smaller circular pore sections (Figure 83).

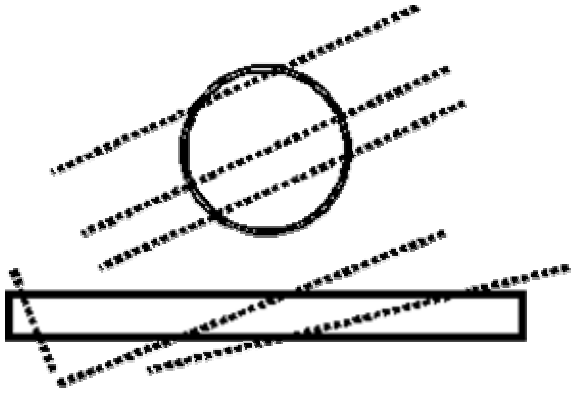

Figure 83: Illustration of 2 distinctly different shapes with the same mean intercept length. Despite the differences in the maximum intercept lengths of each shape, the mean intercept lengths will be equal.

The mean pore intercept length determined by the stereological method is the mean in three dimensions as well as within a planar section. The overall materialographic section mean pore intercept length should then be related to the mean intercept lengths of each pore section. Since the probability of intersecting a pore section with a test line is related to the size of each section in addition to the number of sections of that size, an area weighted mean of the 'mean intercept' of each section should be similar to the overall mean pore intercept length obtained from the standard stereological method. Equation 21 is the equation for, λ', the section area weighted mean of the mean intercept length of each section and is derived (appendix) from the definition of Q and the stereological equations for the mean intercept length and the surface area per unit volume. The summation is over all pore sections where n is the total number of sections, i is the section number, Q_i is the shape factor for section i, and A_i is the area of section i.

Equation 21:
$$\lambda' = \frac{\sqrt{\pi} \cdot \sum_{i=1}^{n} \left[A_i \cdot \sqrt{Q_i \cdot A_i} \right]}{2 \cdot \sum_{i=1}^{n} \sqrt{A_i}}$$

The pore section area weighted mean intercept lengths for each sample (λ') are shown in Figure 84. The value of λ' is approximately constant throughout the intermediate stage for dispersed and flocculated alumina. The mean value of λ' through the intermediate stage is about 0.24μm. All values within the intermediate stage also fall within two standard deviations of the mean (Figure 84). The values of λ' are similar to the stereological mean pore intercept length (MPIL), $\bar{\lambda}^{v}$. The mean pore intercept length through the intermediate stage was approximately 0.22μm. In the flocculated alumina during intermediate stage, the effect of the loss of large pore sections with low Q is compensated for by larger Q values of intermediate and small pore sections. It appears that only when the porosity is closed during the final stage of sintering (V_V > ~0.9) is the mean pore intercept length sensitive to changes in the pore structure.

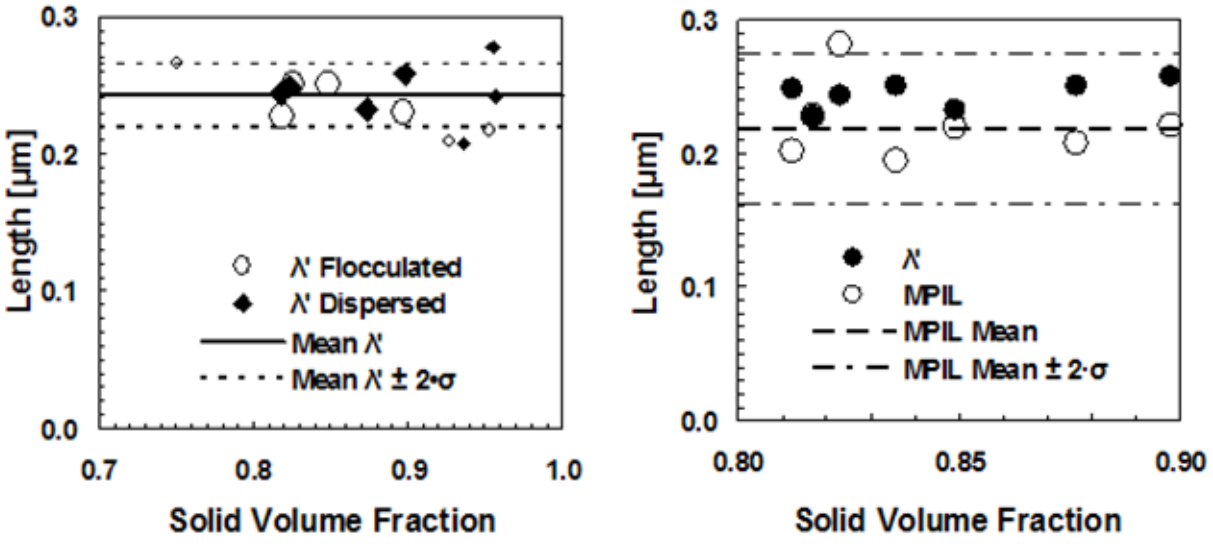

Figure 84: The pore section area weighted mean values of λ´ for both dispersed and flocculated alumina show little change with solid volume fraction during the intermediate stage of sintering (0.82 to 0.90). All values are within 2 standard deviations of the mean of the λ´ through the intermediate stage. The λ´ values agree reasonably well with the mean pore intercept length (MPIL) by the stereological method. With exception of one value all values fall within 2 standard deviations of the mean $\overline{\lambda}^{v}$.

7.7 IMMEDIATE ENVIRONMENT (CA – SAF) EVOLUTION

7.7.1 Low Solid volume Fraction Comparison

The next scale of microstructural characterization involves dividing the microstructure into regions that include both pore and solid areas. The tessellation cell maps of cell area (CA) with solid area fraction (SAF) revealed differences between dispersed and flocculated alumina at the low solid volume fraction (0.82) (Figure 85). The CA-SAF maps may be sensitive to spatial arrangement in cases where the distributions in pore section area and distributions in cell area are

similar for different samples. Differences in the spatial arrangement of pore sections will lead to differences in the correlation between pore section size and cell size.

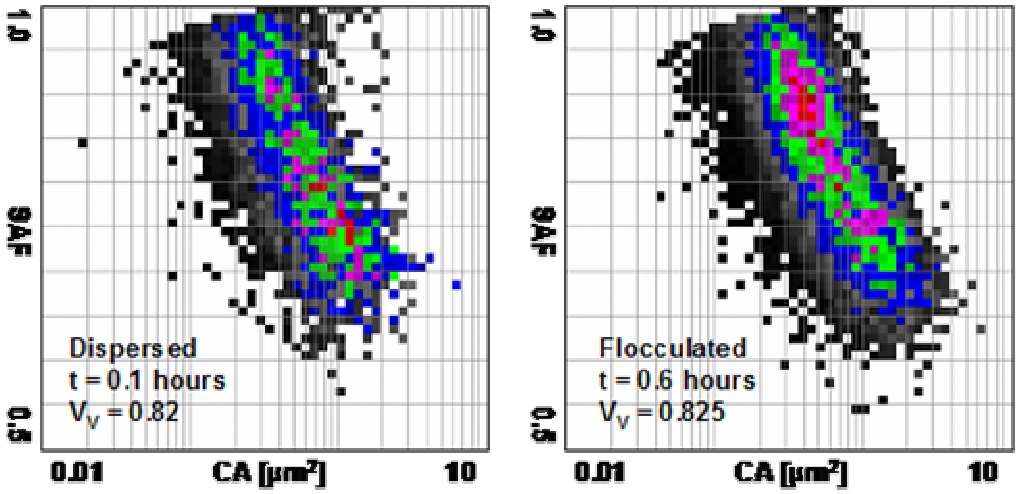

Figure 85: Low solid volume fraction CA-SAF maps for dispersed (left) and flocculated (right) alumina. The peak in the dispersed alumina is relatively low and located at large cell size and low SAF. The flocculated alumina has a pronounced peak located at intermediate cell size and high SAF.

7.7.2 Effect of the Evolution of Pore Population on CA – SAF Maps

Evolution in the CA-SAF maps can result from changes in populations and/or changes in the correlations between CA and PA (pore section area). Lines of constant pore section area superimposed on top of the CA-SAF maps help to illustrate the effect of changes in pore section area distributions on the morphology of the map (Figure 86). If the number of pore sections per unit area (N_A) is reduced without any change in the area of the remaining sections, a constant pore section area contour will be followed (**Figure 87**, top). Figure 86 illustrates the effects that various changes in pore population may have on the CA-SAF maps. In the simplest case, a reduction in pore section area without a change in the number of pore sections per unit area (N_A), will result in an upward shift on the map (Figure 86, a) (**Figure 87**, middle). The pore sections shrink but do not disappear. Some of the pore area associated with a cell is replaced with solid area resulting in an increase in the solid area fraction of that cell. The next case is the reduction in the number of pore sections per unit area while maintaining a constant SAF (Figure 86, b) (**Figure 87**, bottom). This is consistent with a coalescence of the pore sections without

shrinkage. As the number of pore sections is reduced the average cell size increases. This is due to the fact that the average cell size is equal to the inverse of N_A. The third case is break-up of the pore sections into two or more sections (Figure 86, c) (**Figure 87**, bottom). This has the opposite effect of coalescence (b). The result of pore section break up is to shift the CA-SAF distributions to smaller cell sizes due to the increase in N_A associated with the increase in the number of pore sections over the same area. If densification occurs by the axial or radial shrinkage of pore channels or isolated pores, the result would be an increase in cell size with an increase in SAF due to a reduced probability of sampling the pore and the decrease in pore section areas. (d). If densification occurs by pore section break-up with pore section shrinkage, the result would be a decrease in cell size due to an increase in N_A with an increase in SAF due to reduced pore section area (e).

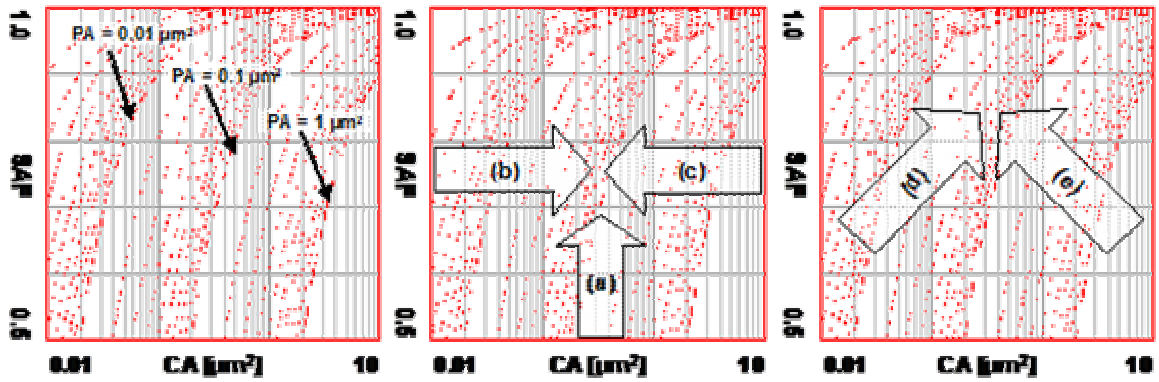

Figure 86: CA-SAF maps with lines (dashed) of constant pore section area (left). Arrows indicate effects of changes in pore size and/or N_A on the CA-SAF maps (right). (a) represents a decrease in pore size without a decrease in N_A. (b) represents a decrease in N_A or an increase in cell size. (c) represents the effect of pore break-up. (d) represents the effect of a combination of (a) and (b). (e) represents a combination of (b) and (c).

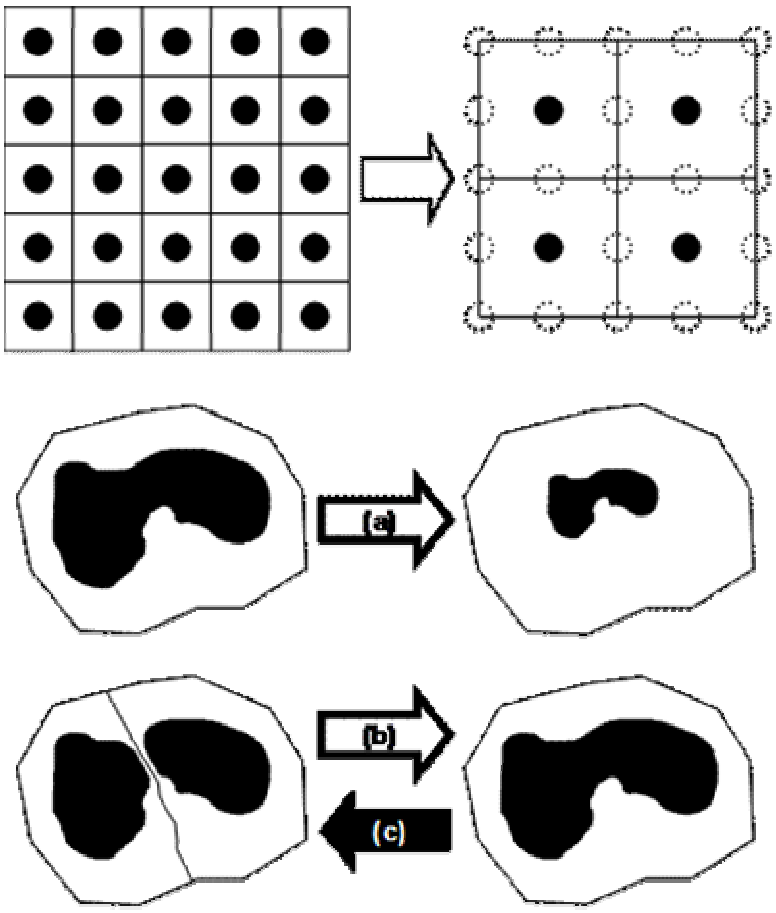

Figure 87: Illustrations of primary evolutions of CA-SAF maps for paths constant PA contour [top], (a), (b), and (c) in Figure 86.

7.8 PORE SECTIONS PER UNIT AREA

The evolution of the number of pore sections per unit area (N_A) for dispersed and flocculated alumina follow similar paths when plotted against the solid volume fraction. There is a nearly linear decrease in N_A with increasing solid volume fraction through the intermediate stage of sintering. The only deviation from this result is an increase in N_A for flocculated alumina from a solid volume fraction of 0.75 to 0.825 (Figure 88).

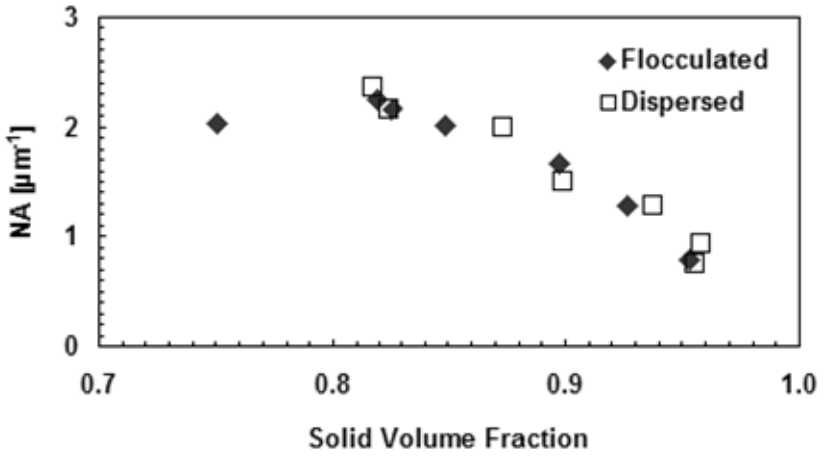

Figure 88: Evolution of the number of pore sections per unit area for dispersed and flocculated alumina. Both aluminas follow the same path. The flocculated alumina N_A increases slightly during the increase in solid volume fraction from 0.75 to 0.825.

7.9 LOCAL ENVIRONMENT (LA – LPA_{MAX})

Another tessellation cell map of interest to this discussion is the pore section area (PA) – mean local pore section area (LPA) map. As the name implies this map characterizes the local area around a pore section's cell on the order of a few grain section diameters. It does not include the characteristics of the enclosed pore section, only its surrounding nearest neighbor cells and pores. Differences between dispersed and flocculated alumina are observed for the low solid volume fraction and the evolution of the maps with time are different for dispersed and flocculated alumina. However, the use of an average value does not illustrate differences in the extremes of local pore size. A form of the PA-LPA map was developed which only identifies the largest neighboring pore section coordinated to each section. If the larger pore sections are breaking-up during sintering, filtering out every cell except for cells containing the large pore sections in the tessellated images will show how many of the large pore sections are coordinated with other large pore sections (**Figure 89**) in two dimensions. Further filtering by removal of large pore sections that are coordinated in two-dimensions with less than three neighboring large

pore sections eliminates large pore sections that form strings. This leaves large pore sections that are clustered together in two-dimensions. Since the materialographic sections do not provide information perpendicular to the plane of polish, information regarding the coordination of large pore sections in the 3rd dimension is not available. However, as in the case of determination of grain size from a materialographic section, the distribution in two dimensional sections should be related to the three dimensional characteristics of the microstructure. Also, the probability of intersecting two or more pores coordinated in three dimensions resulting in two dimensionally coordinated pore sections is lower than simply intersecting a single pore. The cluster of two dimensionally coordinated pore sections in **Figure 89** has 'holes' in it where cells containing small pore sections are not shown. The size of a cluster should include the 'holes.' Therefore, the 'true' cluster section size will likely be much larger than that identified by simply selecting the specified coordinated cells in two dimensions. The 'true' area fraction of the materialographic section associated with these cluster will be higher as well. Further image processing will be required to obtain a more accurate measure of this porosity.

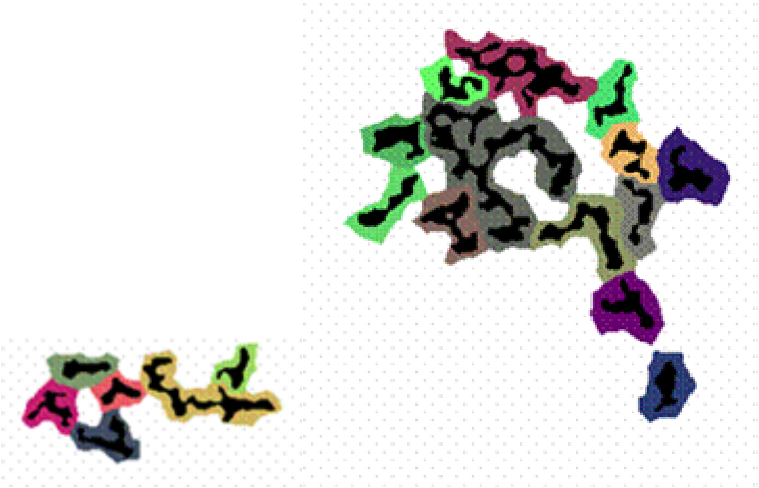

Figure 89: Examples of the strings of large pore sections coordinated with 1 or 2 other large pore sections (left). Example of a cluster of large pore sections coordinated with more than 2 other large pore sections.

7.10 PORE SECTION BREAK-UP

Break-up of the sections does not necessarily require a break-up of the three-dimensional pore structure. Other mechanisms may also be responsible for section break-up. The radial shrinkage of large pore channels or voids could also be seen as pore section break-up during densification due to the reduced probability of sampling a continuous section of the pore channel or void with a materialographic section (**Figure 90**). Another mechanism of pore section break-up would be the rearrangement of grains or particles. Rearrangement is occasionally mentioned in the literature as a possible mechanism of densification. However, evidence of rearrangement except in the case of in situ two dimensional sintering experiments has not been reported[87]. Rearrangement to a more stable arrangement can be achieved without closing off pore channels, thereby, avoiding three-dimensional pore break-up (**Figure 90**). The break-up of large pore sections may result in an increase in the intermediate sized pore section frequency. As densification proceeds and packing improves the solid-solid contact between grains or particles will increase and the number of grains or particles required to perform a single rearrangement will increase. The number and volume associated with these 'rearrangeable' regions will decrease with increasing density. This will slow down the mechanism of the rearrangement as density increases.

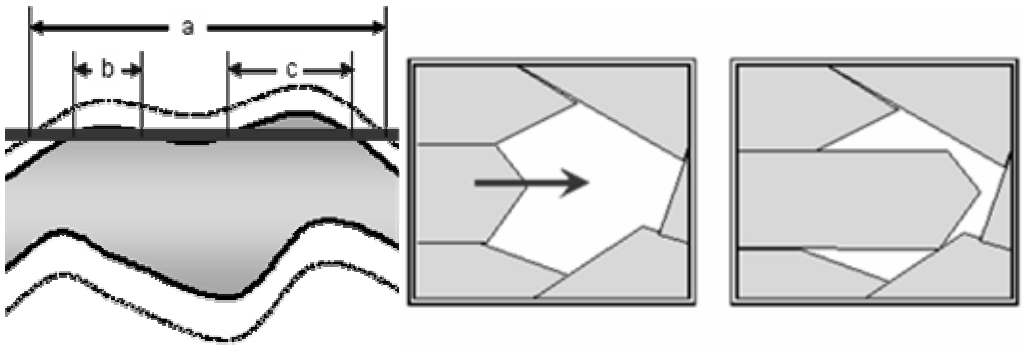

Figure 90: The illustration on the left shows the sectioning of a pore channel by a cutting plane. The dashed lines indicate the size of the channel before shrinking to the solid lines. The initial sectioning results in a single pore section indicated by (a). After the channel shrinks the sectioning results in 2 separate sections, (b) and (c). On the right is an illustration of pore rearrangement that results in 2 pore sections considerably smaller than area of the original section. Both cases would appear as pore break-up in the 2 dimensional section.

7.11 CA – SAF EVOLUTION

Only the tessellation cell maps reveal the differences in microstructure for the low solid volume fraction in the case where the difference in the densification rates of dispersed and flocculated alumina is highest with respect to density (Figure 85). As the solid volume fraction increases the CA-SAF maps for dispersed and flocculated become similar (Figure 91). At higher solid volume fractions the densification rates of dispersed and flocculated alumina are also similar. Therefore, the tessellation cell maps are sensitive to the microstructural characteristics that correlate with the densification kinetics.

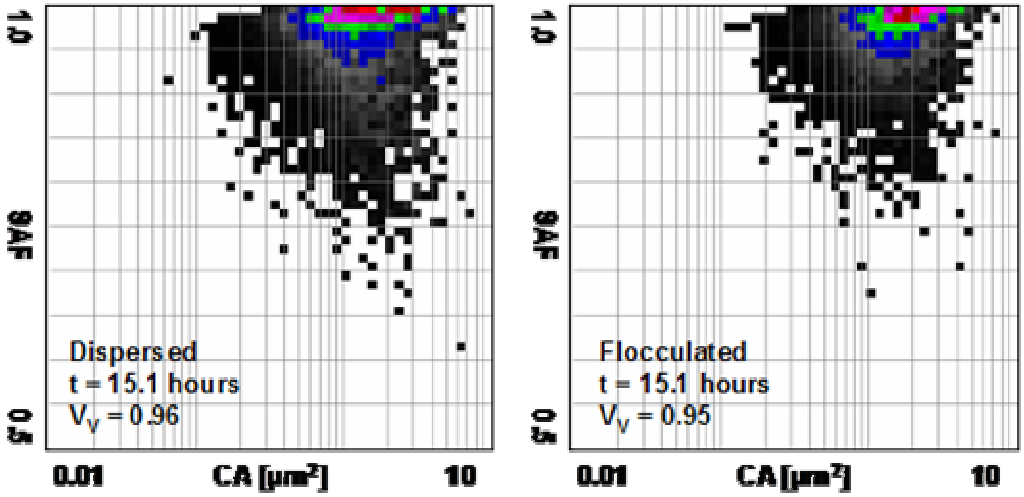

Figure 91: CA-SAF maps for dispersed and flocculated alumina after 15.1 hours at temperature with solid volume fractions of approximately 0.96. Both maps are similar at this density. The densification rates for dispersed and flocculated alumina are similar at this density as well.

The evolution of the CA-SAF maps for dispersed and flocculated alumina through the intermediate stage of sintering indicate that pore section break-up is occurring to some extent in each case. Figure 92 illustrates the motion of the CA-SAF peaks at each time at temperature. Figure 93 shows the motion of the peaks for the low, intermediate and high solid volume fractions. Although the dispersed alumina peaks move along a different path than the flocculated alumina peaks, they reach the same final state. In the case of dispersed alumina there is an abrupt shift in the peak of the CA-SAF maps to an order of magnitude smaller PA and much higher SAF from 0.1 hours to 0.6 hours (Figure 92 and Figure 93). The abrupt shift is consistent with a

combined rearrangement and reduction in N_A. The rearrangement will result in an increase in the number of cells by break-up while the elimination of pore sections due to the other active densification mechanism(s) will shift the distribution to larger cell sizes. In the flocculated alumina CA-SAF maps the shift occurs in a more gradual manner. The shift to lower PA and higher SAF continues through most of the intermediate stage of sintering. The shift in the peak of the CA-SAF map from 0.1 hours (V_V = 0.75) to 0.6 hours (V_V = 0.825) for flocculated alumina is accompanied by an increase in the number of pore sections per unit area. This is consistent with the break-up of pore sections as the dominant densification mechanism. Since the solid volume fraction is 0.82 after only 0.1 hours at temperature it is not known if rearrangement may dominate at solid volume fractions below 0.82 for dispersed alumina. It would appear that only the final stages of the pore section break-up due to rearrangement are being observed for solid volume fractions less than ~0.85 in this study.

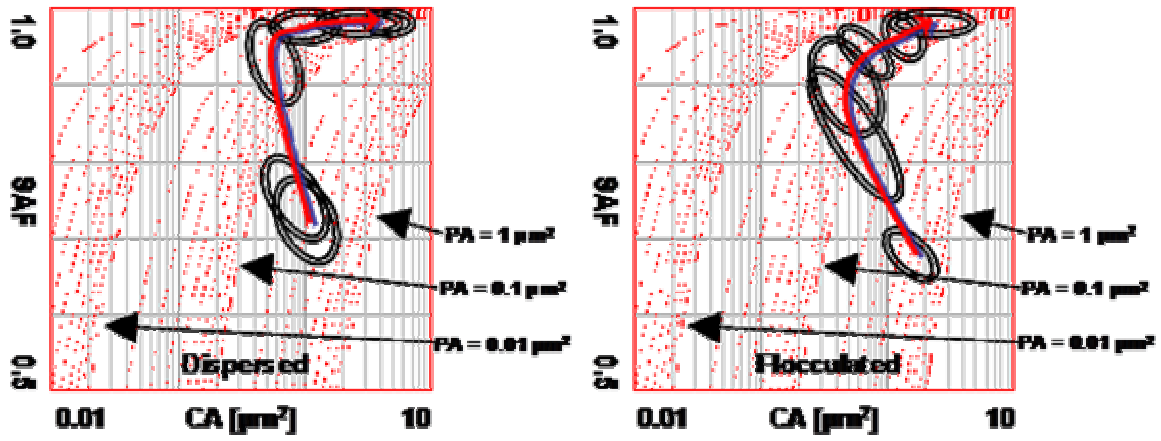

Figure 92: Peak paths for dispersed and flocculated alumina for the CA-SAF maps. Arrows through the centers of peak ovals indicate path of increasing time at temperature.

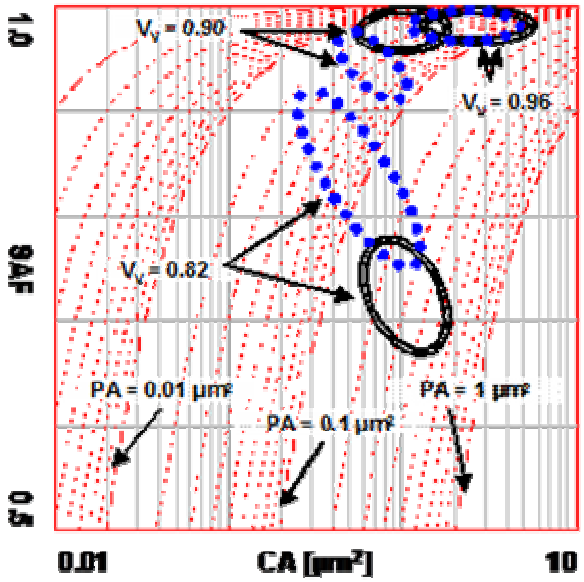

Figure 93: Peak plot of the CA-SAF maps for dispersed and flocculated alumina at the low, intermediate and high solid volume fractions. The dotted ovals are for the flocculated alumina.

7.12 PA – LPA_{MAX} AT LOW SOLID VOLUME FRACTIONS

The pore section area – maximum local pore section area map (PA-LPA Max, Figure 94) reveals more details about the spatial arrangement of pore sections. Pore sections with an area greater than or equal to $0.3\mu m^2$ are selected as the large pore sections for the following analysis because this is the size at which the area weighted pore section area distributions cross for a solid volume fraction of ~0.96 and they would be classified by Zheng and Reed as coarse micropores[36]. At the low solid volume fraction (0.82) the flocculated alumina has 22% of its pore section area associated with large pore sections coordinated with other large pore sections and 4% is associated with the large pore sections coordinated with three or more other large pore sections. The dispersed alumina at the low solid volume fraction has 18% of its pore section area associated with large pore sections coordinated with other large pore sections and only 1% coordinated with three or more other large sections. The fraction or pore section area associated

with the coordinated large pore sections is low. However, the volume of the material associated with these clusters may be much higher. If the shape of these clusters in three dimensions is known, the three dimensional size distribution could be determined using a technique similar to those used in the 'true' grain size distribution analysis. The fraction of these pore sections will decrease as density increases due to rearrangement facilitated by coordinated large pore sections. Although the number of large pore sections remains higher in the dispersed alumina as density increases, the clusters of large pore sections remains low. At a solid volume fraction of approximately 0.85, the densification rates in dispersed and flocculated alumina are approximately equal. At this solid volume fraction, the clusters of two dimensionally coordinated large pore sections have been removed. Since the densification rate is lower in flocculated alumina at the low solid volume fraction (V_V = 0.82) and the fraction of large clustered pore sections is higher, this leads to the conclusion that the mechanism of pore section break-up is the 'slower' mechanism of densification at a solid volume fraction of 0.82. The faster mechanism is likely to be the surface free energy driven densification mechanism of contact flattening typically associated with sintering. The relative rates of densification associated with the different mechanism will depend on density and the available driving force.

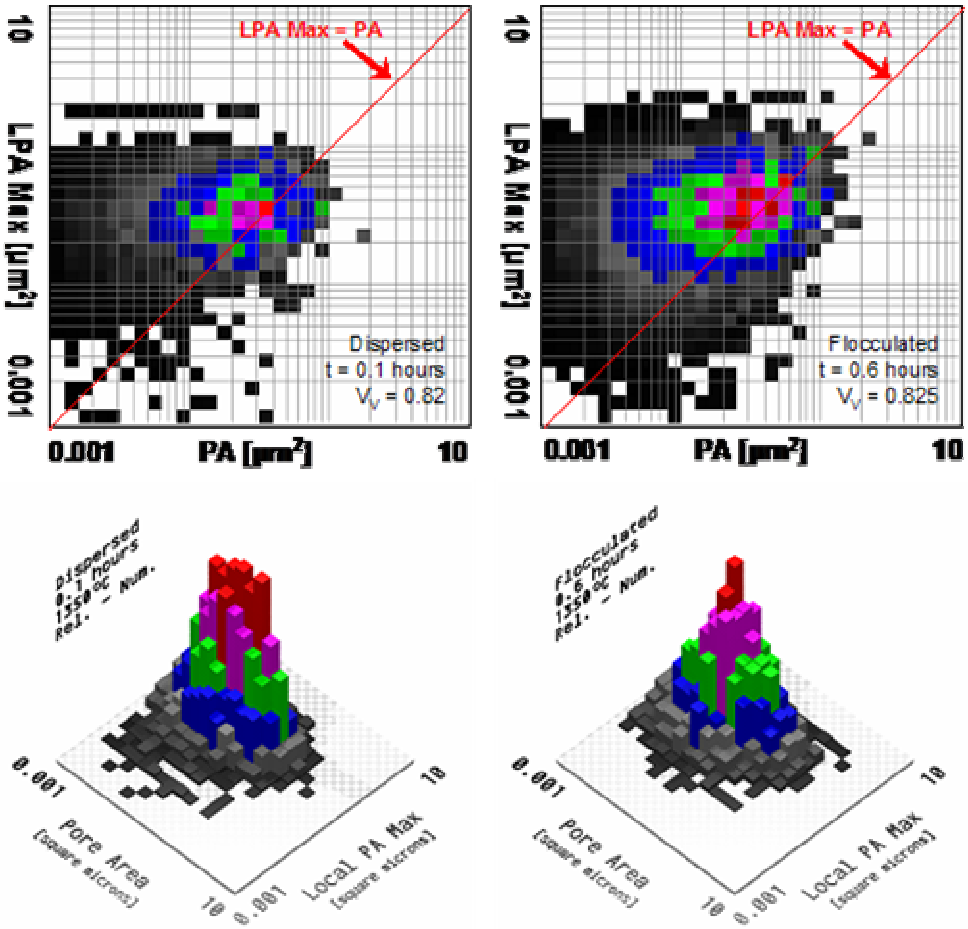

Figure 94: Pore area weighted and relative frequency pore section area – maximum local pore section area maps for the low solid volume fraction dispersed and flocculated alumina. The diagonal line indicates the positions at which the maximum LPA is equal to PA. The dotted line indicates the LPA Max = 0.06µm^2 level.

Figure 95 shows the PA-LPA$_{max}$ map for the flocculated alumina at V_V = 0.75 (0.1 hours at 1350°C). Also shown is an image with the large pore sections coordinated to other large pore sections (PA and LPA$_{max}$ ≥ 0.3µm^2) for this sample. The flocculated alumina at V_V = 0.75 has 43% of its pore section area associated with large pore sections coordinated with other large pore sections and 22% is associated with the large pore sections coordinated with three or more other large pore sections. Considering the large fraction of pore section area associated with these regions and the possible effect that a much smaller population of these pore sections had on the densification rate at V_V = 0.82 suggests that the rearrangement mechanism may dominate at a solid volume fraction of 0.75. The densification rate for flocculated alumina at V_V = 0.75 is

about 30% higher than the densification rate of dispersed alumina at $V_V = 0.82$. Therefore, the densification rate due to rearrangement must be dependent on density and/or the driving force due to solid-vapor surface free energy reduction.

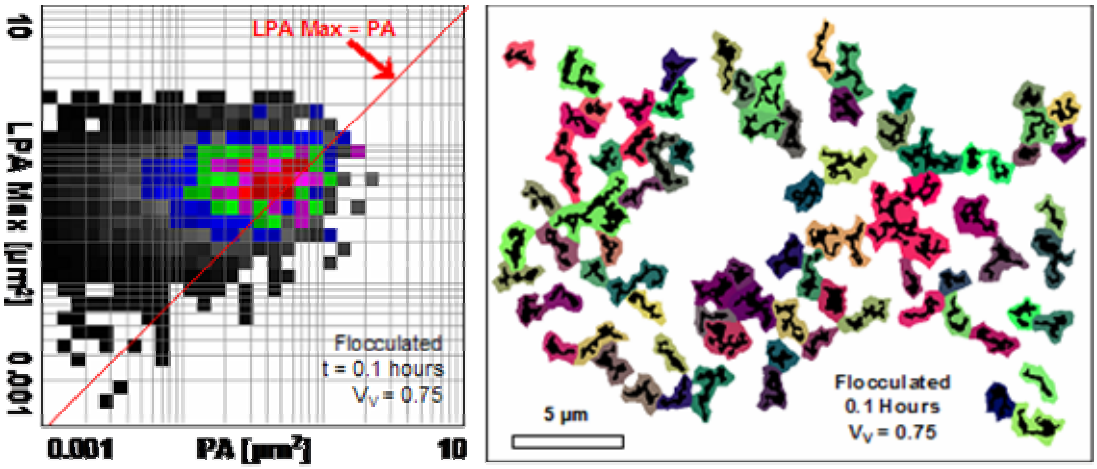

Figure 95: The pore area weighted PA-LPA Max map for flocculated alumina after 0.1 hours at temperature (left) shows that there is a large number of large pores connected to other large pores. The image on the right shows only the large pores sections coordinated to other large pore sections. The sections are in close proximity to each other in the 2-D materialographic section.

7.13 CLOSED POROSITY

During the intermediate stage of sintering at 1350°C, the dispersed alumina has an increasing fraction of closed porosity as solid volume fraction increases (Figure 96). The flocculated alumina porosity remains open until final stage sintering begins. This suggests that the rearrangement mechanism is not associated with three-dimensional pore break-up resulting in pore closure in alumina under the sintering conditions used in this work. The actual mechanism of rearrangement can not be determined from the available data. The mechanism may involve creep, grain boundary sliding, contact rupture, or some combination of mechanisms.

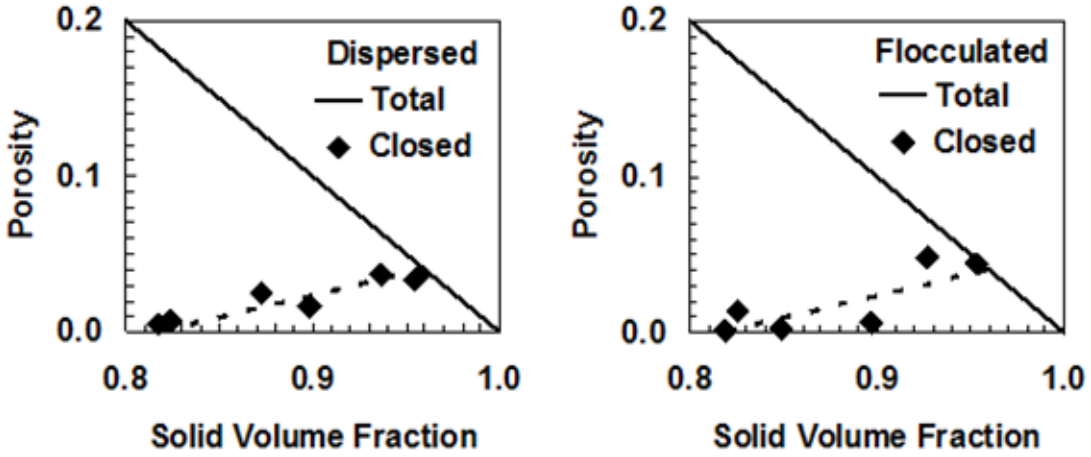

Figure 96: The total porosity at each solid volume fraction is indicated by the solid diagonal lines in the above plots. The dashed line is a linear fit to the closed porosity with solid volume fraction for dispersed alumina. The closed porosity determined by the Archimedes method is indicated by the diamonds. Pore closure does not occur in the flocculated alumina until the solid volume fraction is above ~0.9. However, in the case of the dispersed alumina some porosity appears to close throughout densification.

7.14 DISCUSSION SUMMARY

The sintering of dispersed and flocculated slip cast alumina at 1350°C with a difference in solid volume fractions of less than 0.1 at the beginning of isothermal sintering avoids significant differences in grain growth and coarsening due to flocculation. This is the first study of alumina under these conditions which provides a means of identifying the effects of flocculation on the evolution of densification behavior and microstructure without the effects of grain growth. Tessellation provides a meso-scale description of microstructure that characterizes the collective behavior of grains or particles and their associated regions of the microstructure. It was found that tessellation cell maps were necessary to suggest the existence of two or more densification mechanisms occurring concomitantly during portions of the intermediate stage of sintering (V_V < ~0.9). The cell maps were capable of identifying differences between dispersed and flocculated alumina at low solid volume fraction when all other microstructural parameters

were nearly identical. This is especially significant since this is the point at which the largest difference in densification rate was measured. The CA-SAF maps are sensitive to the characteristics of the microstructure responsible for the difference in densification rate of slip cast alumina sintered at 1350ºC. In addition to contact flattening, another densification mechanism that is believed to be responsible for densification is the rearrangement of the grains or particles in regions containing coordinated large pores. The PA-LPA maps aided in identifying the pore population associated with the rearrangement densification mechanism. The effect of the rearrangement mechanism on the densification rate will depend on the size and number of these clustered large pore sections as well as overall density. The results of this work seem to indicate that the rearrangement of grains or particles at low solid volume fraction leads to a 'better' final microstructure, a narrower distribution of smaller pore sections and similar final density. If this is the case, this mechanism should be enhanced during sintering to obtain a more refined pore structure. Although, the application of tessellation cell maps to the sintering of alumina has provided a means of characterizing the evolution of microstructure and densification behavior due to flocculation and identified the presence of a rearrangement mechanism during intermediate stage sintering, the more important result of this work is that it offers a methodology of microstructure characterization on a meso-scale that can be applied to other materials and features other than pores and grains.

8.0 CONCLUSIONS

The results of this research support the following conclusions:

1. The densification rate for dispersed alumina was significantly higher than the densification rate for flocculated alumina until a solid volume fraction of approximately 0.85 was attained. In this study the distributions in grain size and shape, distributions in pore size and shape, average properties of the microstructure, Dimensionless Microstructural Pathways, and distributions in tessellation cell properties did not correlate with the evolution of the densification rate with solid volume fraction.
2. Boundary tessellation provides a meso-scale description of microstructure by segmenting the microstructure into regions containing a single pore section along with a portion of the solid area which is composed of sections of more than one grain. The length scale of the tessellation cell for alumina sintered at 1350°C is greater than that of the pore section itself but on average only extends to approximately one half of a grain section diameter to one grain section diameter from the pore section boundary. This was classified as the immediate environment. The length scale associated with the local environment (LPA) is approximately three times that of the tessellation cell.
3. Tessellation cell maps that show the correlations between pore section size and tessellation cell parameters due to the spatial arrangement of pore sections (as a consequence of the spatial arrangement of grains) were correlated with the evolution in the densification rate with solid volume fraction. The cell area – cell solid area fraction tessellation cell maps (CA-SAF) show differences in spatial arrangement of pore sections between dispersed and flocculated alumina at low solid volume fraction (0.82) when the densification rates show the greatest measured difference. As solid volume fraction increased, the difference in the CA-SAF maps reduced as well.

4. The shift in the position of the peak in the CA-SAF maps to higher solid area fraction and smaller pore section size, characteristic of pore section break-up, occurs in the dispersed and flocculated alumina at solid volume fractions up to ~0.85 suggesting the occurrence of a rearrangement mechanism. At higher solid volume fractions the shift does not occur. Only evolutions of the map characteristic of pore elimination and shrinkage are observed for solid volume fractions above 0.9.
5. The pore section area-maximum local pore section area tessellation cell maps (PA-LPA_{max}) were used to identify the pore section population associated with the differences between dispersed and flocculated alumina densification rates at low solid volume fraction (0.82). The fraction of pore section area associated with large pore sections coordinated with other large pore sections was higher in flocculated alumina. Also, the fraction associated with large pore sections coordinated with more than two other large pore sections, defining clusters of coordinated large pore sections, was four times as high for flocculated alumina. This suggests that this population is associated with the rearrangement mechanism.
6. The densification rate for flocculated alumina was significantly lower at a solid volume fraction of 0.82. If the rearrangement mechanism is responsible for the difference in densification rates, the mechanism of rearrangement is slower than the other densification mechanism(s) (contact flattening) at this solid volume fraction. The dominance of the rearrangement mechanism should depend on the portion of the microstructure associated with the low density regions and the overall solid volume fraction of the sample. Rearrangement is not evident at solid volume fractions above 0.85.
7. The use of tessellation and the tessellation cell maps was instrumental in discerning the effect of flocculation on the evolution of the microstructure and densification rate of dispersed and flocculated alumina at 1350°C. Consideration of the results of this work should taken when analyzing the results of previous and future work that investigates the role of particle packing on the evolution of microstructure and properties during sintering. It is suspected that the use of tessellation and the interpretation of tessellation cell maps will prove invaluable in the understanding of the evolution of ‘microstructure’ and ‘properties’ for other sintered materials and other systems or processes.

9.0 SUGGESTED FUTURE WORK

- The fraction of the total porosity associated with large pore sections coordinated to other large pore sections was 43% and for large pore sections coordinated to more than two other large pore sections was 22% for flocculated alumina at a solid volume fraction of 0.75. The decrease in this population at a solid volume fraction of 0.82 and further reduction at 0.87 with a decrease in the difference between dispersed and flocculated alumina densification rates indicates that the rearrangement process was only observed during its final stages in this work. Future work should include a more detailed study of the evolution of the meso-scale characteristics of the microstructure and properties of alumina sintered at 1350°C for solid volume fractions below ~0.9.
- Interpretation of the evolution of the tessellation cell maps was difficult. The position and motion of the peaks in the CA – SAF maps was used to characterize the evolution of the microstructure on the meso-scale. However, statistical parameters (correlation coefficient, etc.) that more fully characterize the tessellation cell maps should be developed for a more straightforward and quantitative analysis.
- This study was restricted to microstructural analysis performed using materialographic sections. A direct correlation between two dimensional characteristics of individual tessellation cells could not be made with the three dimensional characteristics of the microstructure. Three dimensional microstructural analyses by x-ray tomography or FIB serial sectioning and reconstruction should be performed to relate the tessellation of two dimensional section data to three dimensional characteristics of the microstructure.
- The movement of individual grains or particles was not observed through the course of this work. In situ experiments or carefully designed interrupted experiments should be performed

to verify the occurrence and determine the nature of the rearrangement of particles or grains during the intermediate stage of sintering.

- The rearrangement of grains or particles mechanism of densification is likely to occur during the sintering of alumina in other flocculation states and other ceramic materials. The tessellation cell maps should be used to characterize the evolution of the microstructure of other ceramic materials during densification. This may be of particular interest in cases of liquid phase sintering where particle rearrangement could be enhanced by the selection of the appropriate liquid phase.
- Computer simulations of particle rearrangement in which the motion of individual and groups of particles can be tracked should be developed to further isolate the effect of rearrangement on tessellation cell maps and their evolution using a wide range of packing arrangements that can not be achieved experimentally.
- The meso-scale description of microstructure and the use of tessellation cell maps could be applied to other systems and processing conditions such as composite materials. Characterization of the spatial arrangement of particles of one or more phases dispersed within a matrix by tessellation may lead to a better understanding of the relationship between microstructure and properties such as fracture strength or toughness. The meso-scale description would be most useful for materials in which the scale of the features of interest is on the same order as the spacing of the features. If the spacing is large relative to the size of the features the boundary tessellation reduces to a point tessellation.

APPENDIX

Derivation of Mean Section Intercept Length

The following is a derivation of a mean pore intercept length for a pore section, λ', based on the equations previously described for the shape factor (Q, Equation 11), the mean pore intercept length, ($\bar{\lambda}^{V}$, Equation 3) and an equation from stereology for the surface area per unit volume (S_V) (Equations 22). In the expression for S_V used here, U_A is the perimeter length per unit area.

$$Q_i = \frac{4 \cdot \pi \cdot A_i}{U_i^2} = \frac{4 \cdot \pi}{A} \cdot \left(\frac{A_i}{U_i} \right)^2$$

Equations 22:

$$\bar{\lambda}^{V} = \frac{4 \cdot (1 - V_V)}{S_V^{SV}}$$

$$S_V = \frac{4}{\pi} \cdot U_A$$

Making the assumption that the relations hold true for individual pore sections, the mean pore intercept length reduces to a form in which the section mean intercept length, λ_i', is proportional to A_i/U_i (Equation 23). A_T is the total sample area, A_i is the pore section area and U_i is the pore section perimeter length.

Equation 23:

$$\bar{\lambda}^{V} \rightarrow \frac{4 \cdot \left(\frac{A_i}{A_T} \right)}{\frac{4}{\pi} \cdot \left(\frac{U_i}{A_T} \right)} = \pi \cdot \left(\frac{A_i}{U_i} \right) = \lambda_i'$$

To understand how shape and size may affect the mean intercept length the relation for λ_i' is substituted into the equation for Q_i. Solving for λ_i' shows that it is proportional to the square root of Q_i times A_i (Equations 24). Therefore, large pore sections with low Q may have a low 'section mean pore intercept length.' Subsequently, it may be possible that small pore sections with high Q would have a larger 'mean pore intercept length' than a large pore section. Since the probability of intersecting a pore section depends on the size of the section, the pore section area weighted mean, λ', will be used.

$$Q_i = \frac{4 \cdot \pi}{A_i} \cdot \left(\frac{\lambda_i'}{\pi} \right)^2$$

$$\lambda_i' = \frac{\sqrt{\pi}}{2} \cdot \sqrt{Q_i \cdot A_i}$$

Equations 24:

$$\lambda' = \frac{\sum_{i=1}^{n} \left[A_i \cdot \lambda_i' \right]}{\sum_{i=1}^{n} \sqrt{A_i}}$$

$$\lambda' = \frac{\sqrt{\pi} \cdot \sum_{i=1}^{n} \left[A_i \cdot \sqrt{Q_i \cdot A_i} \right]}{2 \cdot \sum_{i=1}^{n} \sqrt{A_i}}$$

BIBLIOGRAPHY

1. Exner, H. E., “Principles of Single Phase Sintering,” Reviews in Powder Metallurgy and Physical Ceramics, 1, 1-4, 1979, pp. 1-251.

2. Burke, J. E. and J. H. Rosolowski, “Sintering,” General Electric Technical Information Series, General Electric Company, Schenectady, NY, 1973.

3. Olevsky, E. A., “Theory of Sintering; From Discrete to Continuum,” Materials Science and Engineering, Vol. R23, No.2, 1998, pp. 41-100.

4. Pask, J. A., and A. G. Evans ed., University Conference on Ceramics; Ceramic Microstructures ’86: Role of Interface, “Powders, Interfaces, and Processing: Alumina as a Case Study by A. Roosen, S. Sumita and H. K. Bowen,” Plenum, NY, 1987, pp. 433-446.

5. Reed, J. S., Introduction to the Principles of Ceramic Processing New York: Wiley-Interscience, 1988, p. 87.

6. Kingery, W. D. and M. Berg, "Study of the Initial Stages of Sintering Solids by Viscous Flow, Evaporation - Condensation and Self Diffusion," Journal of Applied Physics, Vol. 26, 1955, pp. 1205-1212.

7. Coble, R. L., "Sintering Crystalline Solids I. Intermediate and Final State Diffusion Models," Journal of Applied Physics, Vol. 32, No.5 1961, pp. 787-792.

8. Ashby, M. F., “A first Report on Sintering Diagrams”, Acta Metallurgica, Vol. 22, 1974, pp. 275-289.

9. Swinkels, F. B. and M. F. Ashby, "A Second Report on Sintering Diagrams," Acta Metallurgica, Vol. ED-29, (1992), pp. 259-281.

10. Mackerle, Jaroslav, "Finite element methods and material processing technology, an addendum," Engineering Computations, Vol. 15 No. 5, 1998, pp. 616-690.

11. Shan, Z. and A. Gokhale, “Micromechanics of Complex Three-Dimensional Microstructures,” Acta Mater., Vol. 49, 2001, pp. 2001-2015.

12. Gokhale, A. and S. Yang, “Applications of Image Processing for Simulation of Mechanical Response of Multi-Length Scale Microstructures of Engineering Alloys,” Metallurgical and Materials Transactions A, Vol. 30A, 1999, pp. 2369-2381.

13. Besson, J. and M. Abouaf, “Rheology of Porous Alumina and Simulation of Hot Isostatic Pressing,” Journal of the American Ceramics Society, 1992, pp. 2165-2172.

14. Anderson, M. P. and A. D. Rollet, ed., Simulation and Theory of Evolving Microstructures, , “Prediction of Microstructural Evolution Using Finite Element Analysis and Structure Development Rules by K. J. Meltsner,” Minerals, Metals and Materials Society, 1990, pp. 179-188.

15. Messing, G. L., S. Hirano, and H. Hausner ed., Ceramic Powder Science III, “A Constitutive Model for the Finite Element Simulation of Sintering – Distortions and Stresses by H. Reidel,” Ohio: The American Ceramic Society, 1990, pp. 619-630.

16. Conway, J. J., Masters Thesis, Department of Materials Science and Engineering, University of Pittsburgh, 1990.

17. Cameron, C. P. and R. Raj, "Better Sintering through Green-State Deformation Processing," Journal of American Ceramic Society, Vol. 73, No. 7, 1990, pp. 2032-1037.

18. Yeh, T. S. and M. D. Sacks, "Low-Temperature Sintering of Alumina Oxide," Journal of the American Ceramic Society, Vol. 71, No. 10, 1988, pp. 841-844.

19. Parse, J. B. and J. A. Wert, "A geometrical description of particle distributions in materials," Modelling Simul. Mater. Sci. Eng., Vol., 1, 1993, pp. 275–296.

20. Anderson, M. P. and A. D. Rollet, ed., Simulation and Theory of Evolving Microstructures, , “The Characterization of Microstructures Using Tessellations and Their Application to Deformation Processes,” Minerals, Metals and Materials Society, 1990, pp. 199-209.

21. Boselli, J., P. D. Pitcher, P. J. Gregson and I. Sinclair, "Secondary phase distribution analysis via finite body tessellation," Journal of Microscopy, Vol. 195, Pt 2, August 1999, pp. 104–112.

22. Ghosh, S., Z. Nowak and K. Lee, "Quantitative characterization and modeling of composite microstructures by voronoi cells," Acta Mater., Vol. 45, No. 6, 1997, pp. 2215-2234.

23. Wray, P. J., O. Richmond, and H. L. Morrison, “Use of the Dirichlet Tessellation for Characterizing and Modeling Nonregular Dispersions of Second-Phase Particles,” Metallography, Vol. 16, 1983, pp 39-58.

24. Yan, M. F., R. M. Cannon and U. Chowdry, “Effect of Grain Size Distribution on Sintered Density,” Materials Science and Engineering, Vol. 60, 1983, pp. 275-281.

25. Chappell, J. S., T. A. Ring and J. D. Birchall, "Particle Size Distribution Effects on Sintering," Journal of Applied Physics, Vol. 60, 1986, pp. 383-391.

26. Ting, J. M. and R. Y. Lin, "Effect of Particle Size Distribution on Sintering," Journal of Materials Science, Vol. 30, 1995, pp. 2382-2389.

27. Shiau, F. S., T. T. Fang and T. H. Leu, “Effect of Particle Size Distribution on the Microstructural Evolution in the Intermediate Stage of Sintering," Journal of the American Ceramic Society, Vol. 80, No. 2, 1997, pp. 286-290.

28. German, R. M., “Sintering Densification for Powder Mixtures of Varying Distribution Widths,” Acta Metall. Mater., Vol. 40, No. 9, 1992, pp. 2085-2089.

29. Smith, J. P. and G. L. Messing, "Sintering of Bimodally Distributed Alumina Powders," Journal of the American Ceramic Society, Vol. 67, No. 4, 1984, pp. 238-242.

30. Handwerker, C. A., J. E. Blendell and W. A. Kaysser ed., Ceramic Transactions 7, Sintering of Advanced Ceramics, "Influence of Surface Area and Particle Size Distribution on Sintering and Microstructure Development, by M. A. Occhionero, S. L. Marallo, A. E. Karas, and B. E. Novich" Ohio: The American Ceramic Society, 1990, pp. 357-370.

31. Rahaman, M. N., DeJonghe, L. C. and Chu, M. Y., "Effect of Green Density on Densification and Creep During Sintering," Journal of the American Ceramic Society, Vol. 74, No. 3, 1991, pp. 514-519.

32. Cameron, C. P. and R. Raj, "Grain Growth Transition During Sintering of Colloidally Prepared Alumina Powder Compacts," Journal of American Ceramic Society, Vol. 71, No.12, 1988, pp. 1031-1035.

33. Venkataraman, K. S. and R. A. DiMilia “Predicting the Grain Size Distributions in High Density, High Purity Alumina Ceramics," Journal of the American Ceramic Society, Vol. 72, No. 1, 1989, pp. 33-39.

34. Kovar, D. and M. J. Readey, “Grain Size Distributions and Strength Variability of High Purity Alumina," Journal of the American Ceramic Society, Vol. 79, No. 2, 1996, pp. 305-312.

35. Messing, G. L., S. Hirano, and H. Hausner ed., Ceramic Powder Science III, "Principles of Slip Casting / Pressure Filtration by K. Bridger and M. Massuda," Ohio: The American Ceramic Society, 1990, pp. 507-519.

36. Zheng, J. and J. S. Reed, "The Different Roles of Forming and Sintering on Densification of Powder Compacts," American Ceramic Society Bulletin, Vol. 71, No. 9, 1992, pp. 1410-1416.

37. Kuczynski, G. C., "Self-diffusion in Sintering of Metallic Particles," Transactions of the AIME, Vol. 185, 1949, pp. 169-178.

38. German, R. M. and Z. A. Munir, " Surface Area Reduction During Isothermal Sintering ", Journal of American Ceramic Society, Vol. 59, 1976, pp. 379.

39. Handwerker, C. A., J. E. Blendell and W. A. Kaysser ed., Ceramic Transactions 7, Sintering of Advanced Ceramics, "Surface Area, Average Mean Curvature and Chemical Potential in Porous Bodies by S. Prochazka," Ohio: The American Ceramic Society, 1990, pp. 164-184.

40. Lange, F. F. and B. J. Kellett, "Thermodynamics of Densification: I, Sintering of Simple Particle Arrays, Equilibrium Configurations, Pore Stability, and Shrinkage," Journal of the American Ceramic Society, Vol. 72, No. 5, 1989, pp. 729-734.

41. Pan, J., H. Le, S. Kucherenko and J. A. Yeomans, "A Model for the Sintering of Spherical Particles of Different Sizes by Solid State Diffusion." Acta Mater., Vol. 46, No. 13, 1998, pp. 4671-4690.

42. Tomsia, A. P. and A. M. Glaeser ed., Ceramic Microstructures: Control at the Atomic Level, "Effect of Packing Structure of Powder Particles in a Ceramic Green Body on Microstructure Development During Densification by K. Uematsu and N. Uchida," Plenum, New York, 1998, pp 239-246.

43. Handwerker, C. A., J. E. Blendelland, W. A. Kaysser ed., Ceramic Transactions 7, Sintering of Advanced Ceramics, "Effect of Green Microstructure on Sintering of Alumina by T. S. Yeh and M. D. Sacks" Ohio: The American Ceramic Society, 1990, pp. 309-331.

44. Pask, J. A., and A. G. Evans ed., University Conference on Ceramics; Ceramic Microstructures '86: Role of Interface, "The Role of Powder Packing in Sintering by L. C. De Jonghe, M. N. Rahaman and M. Lin," Plenum, NY, 1987, pp. 447-454.

45. Gupta, T. K., "Possible Correlation between Density and Grain Size during sintering", Journal of the American Ceramics Society, Vol. 55, No. 5, 1972, pp. 276-277.

46. Pask, J. A., and A. G. Evans ed., University Conference on Ceramics; Ceramic Microstructures '86: Role of Interface, "Effect of Pores on Microstructural Development by M. P. Harmer and J. Zhao," Plenum, NY, 1987, pp. 455-464.

47. Liu, Y. and Patterson, B. R., "Grain Growth Inhibition by porosity", Acta Metallurgica, Vol. ED-41, No. 9, (1993), pp. 2651-56.

48. Wörner, C. H. and P. M. Hazzledine, "Grain Growth Stagnation by Inclusions or Pores," JOM, September, 1992, pp.16-19.

49. Bockstiegel, G., "Relations Between Pore Structure and Densification Mechanism in the Compacting of Iron Powder," International Journal of Powder Metallurgy, Vol. 2, No. 4, 1966, pp. 13-26.

50. Liu, Y. and B. R. Patterson, "A Stereological Model of the Degree of Grain Boundary-Pore Contact During Sintering," Metallurgical Transactions A, Vol. 24A, 1993, pp. 1497-1505.

51. Patterson, B. R. and Y. Liu, "Relationship between Grain Boundary Curvature and Grain Size," Metallurgical Transactions A, Vol. 23A, 1992, pp. 2481-2482.

52. Patterson, B. R., Liu, Y. and Griffin, J. A., "Degree of Pore-Grain Boundary Contact During Sintering," Metallurgical Transactions A, Vol. 21A, No.8, 1990, pp. 2137-2139.

53. Liu, Y. and B. R. Patterson, "Determination of Pore Mobility during Sintering," Metallurgical Transactions A, Vol. 25A, 1994, pp. 81-87.

54. Knepper, W., ed., Agglomeration, "Rate of Densification in the Sintering of Uncompacted Metal Powders, by F. N. Rhines, R. T. DeHoff and R. A. Rummel," New York: Interscience, Wiley and Son, 1962, p. 351-378.

55. Yeh, T. S. and M. D. Sacks, "Effect of Particle Size Distribution on the Sintering of Alumina," Journal of the American Ceramic Society, Vol. 71, No. 12, 1988, pp. C484-C487.

56. Hirano, S. , G. L. Messing, and H. Hausner ed., Ceramic Powder Science IV, "Surface Chemistry of Ceramic Powders in Aqueous Solutions by S. Takeda, M. Kurose and I. Tari," Ohio: The American Ceramic Society, 1991, pp. 203-208.

57. Horn, R. G., "Surface Forces and Action in Ceramic Materials," Journal of the American Ceramic Society, Vol. 73, No. 5 1990, pp. 1117-1135.

58. Messing, G. L., S. Hirano, and H. Hausner ed., Ceramic Powder Science III, "Controlling the Rheology of Colloidal Dispersions Through the Interparticle Potential by W. B. Russel," Ohio: The American Ceramic Society, 1990, pp. 361-373.

59. Hirano, S. , G. L. Messing, and H. Hausner ed., Ceramic Powder Science IV, "New Interparticle Potential Paradigm for Advanced Powder Processing by F. F. Lange," Ohio: The American Ceramic Society, 1991, pp. 185-201.

60. Messing G. L., E. R. Fuller, Jr., H. Hausner ed., Ceramic Powder Science II, "The Effect of Ultrasonic Treatments on the Particle Size Distribution and Microstructure of a Slipcast Al_2O_3 by C. R. Blanchard-Ardid and R. A. Page," Ohio: The American Ceramic Society, 1987, pp. 724-732.

61. Cesarano, J., I. A. Aksay and A. Bleier, "Stability of Aqueous α-Al_2O_3 Suspensions with Poly(methacrylic acid) Polyelectrolyte," Journal of the American Ceramic Society, Vol. 71, No.4, 1988, pp. 250-255.

62. Cesarano, J. and I. A. Aksay, "Processing of Highly Concentrated Aqueous α-Alumina Suspensions Stabilized with Polyelectrolytes," Journal of the American Ceramic Society, Vol. 71, No.12, 1988, pp. 1062-1067.

63. Smith, P. A. and R. A. Haber, "Reformulation of an Aqueous Alumina Slip Based on Modification of Particle Size Distribution and Particle Packing," Journal of the American Ceramic Society, Vol. 75, No. 2, 1992, pp. 290-294.

64. Agrawal, D. C., R. Raj and C. Cohen, "Nucleation of Flocs in Dilute Colloidal Suspensions," Journal of the American Ceramic Society, Vol. 72, No. 11, 1989, pp. 2148-2153.

65. Hirano, S. , G. L. Messing, and H. Hausner ed., Ceramic Powder Science IV, "Dispersion Behavior of Aqueous Suspensions of Aluminum Oxide Powders by F. C. Jang and H. U. Anderson," Ohio: The American Ceramic Society, 1991, pp. 209-216.

66. Nettleship, I. and R. Sampathkumar, "Coarsening of Mesoporous α-Al_2O_3, Ceramics," Journal of Porous Materials, Vol. 4, 1997, pp. 1-7.

67. Chu, M. Y., L. C. De Jonghe, M. Lin and F J. T. Lin, "Precoarsening to Improve Microstructure and Sintering of Powder Compacts," Journal of the American Ceramic Society, 74, No. 11, 1991, pp. 2902-2911.

68. Fang, Z., B. R. Patterson and M. E. Turner, "Influence of Particle Size Distribution on Coarsening," Acta Metall. Mater., Vol. 40, No. 4, 1992, pp. 713-722.

69. Anderson, M. P. and A. D. Rollet, ed., Simulation and Theory of Evolving Microstructures, , "Simulation and Experimental Investigation of particle Size Distribution During Coarsening by Z. Fang and B. R. Patterson," Minerals, Metals and Materials Society, 1990, pp. 151-159.

70. Uskokovic, D., H. Palmour and R. M. Spriggs ed., Science of Sintering, “Grain Boundaries in Sintering by J. A. Pask,” Plenum, NY, 1989, pp. 381-393.

71. Shaw, N. J. and R. J. Brook, "Structure and Grain Coarsening During the Sintering of Alumina," Journal of the American Ceramic Society, Vol. 69, No. 2, 1986, pp. 107-110.

72. Wagh, A. S., R. B. Poeppel and J. P. Singh, “Open pore description of mechanical properties of ceramics,” Journal of Materials Science, Vol. 26, 1991, pp. 3862-3868.

73. Prasad, P. B. and J. P. Jernot, "Topological description of the densification of a granular medium," Journal of Microscopy, Vol. 163, No. 2, 1990, pp. 211-220.

74. Chen, P. L., and I. W. Chen, “Sintering of Fine Oxide Powders: I, Microstructural Evolution," Journal of the American Ceramic Society, 79, No. 12, 1996, pp. 3129-3141.

75. Chen, P. L., and I. W. Chen, “Sintering of Fine Oxide Powders: II, Sintering Mechanisms," Journal of the American Ceramic Society, Vol. Vol. 80, No. 3, 1997, pp. 637-645.

76. Arzt, E., "The Influence of an Increasing Particle Coordination on the Densification of Spherical Powders," Acta Metallurgica, Vol. 30, , 1982, pp. 1883-1890.

77. Akash, A. and M. J. Mayo, “Pore Growth during Initial Stage Sintering," Journal of the American Ceramic Society, Vol. 82, No. 11, 1999, pp. 2948-2952.

78. Kuczynski, G. C., A. E. Miller and G. A. Sargent, ed., Materials Science Research Volume 16, Sintering and Heterogeneous Catalysis, "Channel Network Decay in Sintering by F. N. Rhines and R. T. DeHoff" New York: Plenum Press, 1984, pp. 49-61.

79. Kuczynski, G. C ed., Proceedings of the Sixth International Conference on Sintering and Related Phenomenon Including Catalysis, "A Cell Model for Microstructural Evolution in Sintering by R. T. DeHoff" New York: Plenum Press, 1984, pp. 97.

80. Uskokovic, D., H. Palmour and R. M. Spriggs ed., Science of Sintering, “Stereological Theory of Sintering by R. T. DeHoff,” Plenum, NY, 1989, pp. 55-70.

81. Svoboda, J., H. Riedel and H. Zipse, “Equilibrium Pore Surfaces, Sintering Stresses and Constitutive Equations for the Intermediate and Late Stages of Sintering – I. Computation of Equilibrium Surfaces,” Acta Metall. Mater., Vol. 42, No. 2, 1995, pp. 435-443.

82. Riedel, H., J. Svoboda, and H. Zipse, “Equilibrium Pore Surfaces, Sintering Stresses and Constitutive Equations for the Intermediate and Late Stages of Sintering – II. Diffusional Densification and Creep,” Acta Metall. Mater., Vol. 42, No. 2, 1995, pp. 445-452.

83. Svoboda, J. and H. Riedel, “Quasi-equilibrium Sintering for Coupled Grain Boundary and Surface Diffusion,” Acta Metall. Mater., Vol. 43, No. 2, 1995, pp. 499-506.

84. Chuang, T. J. and J. W. Rudnicki eds., Multiscale Deformation and Fracture in Materials and Structures, “A Comprehensive Model for Solid State Sintering and Its Application to Silicon Carbide by H. Riedel and B. Blug,” Kluwer, 2001, pp. 49-70.

85. Liu, Y. and B. R. Patterson, “Frequency of Pore Location in Sintered Al_2O_3," Journal of the American Ceramic Society, Vol. 75, No. 9, 1992, pp. 2599-2600.

86. Sacks, M. D., and T. Y. Tseng, “Preparation of SiO_2 Glass from Model Powder Compacts: II, Sintering," Journal of the American Ceramic Society, Vol. 67, No. 8, 1984, pp. 532-537.

87. Weiser, M. W., and L. C. De Jonghe, “Rearrangement During Sintering in Two-Dimensional Arrays," Journal of the American Ceramic Society, Vol. 69, No. 11, 1986, pp. 822-826.

88. Rice, R. W., "Evaluating Porosity Parameters for Porosity-Property Relations," Journal of the American Ceramics Society, Vol. 76, No.7, 1993, pp. 1801-1808.

89. Rice, R. W., “Relation of Tensile Strength-Porosity Effects in Ceramics to Porosity Dependence of Young’s Modulus and Fracture Enery, Porosity Character and Grain Size,” Materials Science and Engineering A, Vol. A112, 1989, pp. 215-224.

90. Sudduth, R. D., “A generalized model to predict the effect of voids on modulus in ceramics,” Journal of Materials Science, Vol. 30, 1995, pp. 4451-4462.

91. Boccaccini, A. R., G. Ondracek and E. Mombello, “Determination of Stress concentration factors in porous materials,” Journal of Materials Science Letters, Vol. 14, 1995, pp. 534-536.

92. Powell, M. J., “Computer Simulated Random Packing of Spheres,” Powder Technology, Vol. 25, 1980, pp. 45-52.

93. Stroeven, P. and Martijn Stroeven, “Assessment of packing characteristics by computer simulation,” Cement and Concrete Research, Vol. 29, 1999, pp. 1201-1206.

94. Lin, X. and T. T. Ng, “A three-dimensional discrete element model using arrays of ellipsoids,” Geotechnique, Vol. 47, No. 2, 1997, pp. 319-329.

95. Yang, A., C. T. Miller and L. D. Turcoliver, “Simulation of correlated and uncorrelated packing of random size spheres,” Physical Review E, Vol. 53, No. 2, 1996, pp. 1516-1524.

96. Kim, J. C., K. H. Auh and D. M. Martin, “Multi-level particle packing model of ceramic agglomerates," Modelling Simul. Mater. Sci. Eng., Vol. 8, 2000, pp. 159–168.

97. Yang, G. and P. Biswas, "Computer Simulation of the Aggregation and Sintering Restructuring of Fractal-like Clusters Containing Limited Numbers of Primary Particles," Journal of Colloid and Interface Science, Vol. 211, 1999, pp. 142–150.

98. Favier, J.F., M.H. Abbaspour-Fard, M. Kremmer and A.O. Raji, "Axi-symmetrical, Shape representation of axisymmetrical, non-spherical particles in discrete element simulation using multi-element model particles," Engineering Computations, Vol. 16, No. 4, 1999, pp. 467-480.

99. Kremmer, M. and J. F. Favier, "Calculating rotational motion in discrete element modelling of arbitrary shaped model objects," Engineering Computations, Vol. 17, No. 6, 2000, pp. 703-714.

100. Kim, Jong Cheol , Keun Ho Auh and David M Martin, "Multi-level particle packing model of ceramic agglomerates," Modelling Simul. Mater. Sci. Eng., Vol., 8, 2000, pp. 159–168.

101. Russ, J. C., “The Image Processing Handbook; Third Edition,” CRC Press, 1998.

102. Serra, J., “Image Analysis and Mathematical Morphology,” Academic Press, NY, 1982.

103. Vander Voort, G., ed., MiCon 90: Advances in Video Technology for Microstructural Control, ASTM STP 1094, "Grain Boundary Reconstruction for Grain Sizing by J. J. Friel, E. B. Prestridge and F. Glazer" Philadelphia: American Society for Testing and Materials, 1990, pp. 170-184.

104. Kurzydlowski, K. J. and B. Ralph, “The Quantitative Description of the Microstructure of Materials,” CRC, NY, 1995.

105. Underwood, E. E., Quantitative Stereology, Massachusetts: Addison-Wesley, 1970, pp. 27.

106. Weibel, E. R., Stereological Methods Volume 1, Practical Methods in Biological Morphometry New York: Academic Press, 1979.

107. Vander Voort, G., ed., Applied Metallography, "Problem Solving Using Quantitative Stereology, by R. T. DeHoff" New York: Van Nustrand-Reinhold Company, 1986, pp. 89-99.

108. Exner, H. E. and H. P. Hougardy, Quantitative Image Analysis of Microstructures: A Practical Guide to Techniques, Instrumentation, and Assessment of Materials, Stuttgart: Verlag, 1988, p. 10.

109. Dehoff, R. T. and F. N. Rhines, “Quantitative Microscopy,” McGraw-Hill, NY, 1968.

110. Cahn, R. W. and P. Haasen ed., Physical Metallurgy: 4th Revised and Enhanced Edition, “Qualitative and Quantitative Surface Microscopy by H. E. Exner,” Elsevier, 1996 pp. 996-1032.

111. "Standard Test Method for Water Absorption, Bulk Density, Apparent Specific Gravity of Fired Whiteware Products: ASTM C 373-372." American Society for Testing and Materials, Philadelphia.

112. Tressler, R. E., G. L. Messing, C. G. Pantano and R. E. Newnham ed., Materials Science Research Volume 20, Tailoring Multiphase and Composite Ceramics, "Quantitative Microstructural Characterization and Description of Multiphase Ceramics by R. T. DeHoff" New York: Plenum Press, 1986, pp. 207-222.

113. Dullien, F. A. L. and P. N. Mehta, “Particle Size and Pore (Void) Size Distribution Determination by Photomicrographic Methods,” Powder Technology, Vol. 5, 1971-72, pp. 179-193.

114. Kronsbein, J., L. J. Buteau and R. T. DeHoff, "Measurement of Topological Parameters for Description of Two-Phase Structures with Special Reference to Sintering," Transactions of the AIME, Vol. 233 1965, pp. 1961-1969.

115. Wurst, J. C. and J. A. Nelson, "Lineal Intercept Technique for Measuring Grain Size in Two-Phase Polycrystalline Ceramics," Journal of the American Ceramics Society, Vol. 55, No. 2, 1972, p. 109.

116. Aigeltinger, E. H. and Exner, H. E., "Stereological Characterization of the Interaction Between Interfaces and its Application to the Sintering Process," Metallurgical Transactions A, Vol. 8A, No.3, 1977, pp. 421-424.

117. Patterson, B. R. and Y. Liu, "Quantification of Grain Boundary-Pore Contact During Sintering," Journal of the American Ceramic Society, Vol. 73. No. 12, 1990, pp. 3703-3705.

118. Missiaen, J. M. and S. Rourke, "Automatic image analysis methods for the determination of stereological parameters – application to the analysis of densification during solid state sintering of WC-Co compacts," Journal of Microscopy, Vol. 1999, No. 2, 2000, pp. 141-148.

119. Nettleship, I., M. D. Lehigh and R. Sampathkumar, “Microstructural Pathways for the Sintering of Alumina Ceramics,” Scripta Materialia, Vol. 37, No. 4, 1997, pp. 419-424.

120. Slaughter, W. S., I. Nettleship, M. D. Lehigh and P. O. Tong, " A Quantitative Analysis of the Effect Geometric Assumptions in Sintering Models", Acta Mater., Vol. 45, No. 12, 1997, pp. 5077-5086.

121. Nettleship, I. and W. S. Slaughter, "Dimensionless Parameters for Microstructural Pathways in Sintering," Journal of the American Ceramic Society, Vol. 81, No. 3, 1998, pp. 700-704.

122. DeHoff, R. T., "Quantitative Serial Sectioning Analysis: Preview," Journal of Microscopy, Vol. 131, No.9, 1983, pp. 258-263.

123. Li, M., S. Ghosh, T. N. Rouns, H. Weiland, O. Richmond and W. Hunt, "Serial Sectioning Method in Construction of 3-D Microstructures for particle-Reinforced MMCs," Materials Characterization, 41, 1998, pp. 81-95.

124. Wofsdorf, T. L., W. H. Bender and P. W. Voorhees, "The Morphology o High Volume Fraction Solid-Liquid Mixtures: An Application of Microstructural Tomography", Acta Metallurgica, Vol. 45, 1997, pp. 2279-2295.

125. S. A. Saltykov, "Stereometric Metallurgy," English Translation by Technical Documents Liaison Office, MCLTD, Wright-Patterson Air Force Base, Ohio (1961).

126. Exner, H. E., "Analysis of Grain and Particle Size Distributions in Metallic Materials," International Metallurgical Review, Vol. 17, 1972, pp. 25-42.

127. Delie, F. and D. Bouvard, "Investigation of the consolidation of powder composite by image analysis," Materials Science and Engineering A, Vol. A184, 1994, pp. 65-71.

128. Benes, V., M. Jiruse and M. Slamova, "Stereological Unfolding of the Trivariate Size-Shape-Orientation Distribution of Spheroidal Particles with Application" Acta Mater., Vol. 46, No. 3, 1997, pp. 1105-1113.

129. Zhao, X. B., "Measurement and Calculation of Three-Dimensional Grain Sizes and Size Distribution Functions," Microscopy and Microanalysis, Vol. 4, 1998, pp. 420-427.

130. Coleman, R., "Inverse Problems," Journal of Microscopy, Vol. 153, No. 3, 1989, pp. 233-248.

131. Fang, Z., B. R. Patterson and M. E. Turner, "Modeling Particle Size Distributions by the Weibull Distribution Function," Materials Characterization, Vol. 31, 1993, pp. 177-182.

132. Rhines, F. N. and B. R. Patterson, "Effect of the Degree of Prior Cold Work on the Grain Volume Distribution and the Rate of Grain Growth of Recrystallized Aluminum," Metallurgical Transactions A, Vol. 13A, 1982, pp. 985-993.

133. Vaz, M. F. and M. A. Fortes, "Grain Size Distribution: The Lognormal and the Gamma Distribution Functions," Scripta Metallurgica, Vol. 22, 1988, pp. 35-40.

134. Limpert, E., W. A. Stahel and M. Abbt, " Lognormal Distributions across the Sciences: Keys and Clues," Bioscience, Vol. 51, No. 5, 2001, pp. 341-352.

135. Schwartz, D. M., "A general method of calculating particle size distributions," Journal of Microscopy, Vol. 96, No. 1, 1972, pp. 25-35.

136. Paul, J. L., " Distribution curves of sectional areas through some families of convex particles," Journal of Microscopy, Vol. 122, No. 2, 1980, pp. 165-172.

137. Wasén, J. and R. Warren, "Quantitative Metallographic Characterization of Cubo-Spherical Particles," Metallography, Vol. 20, 1987, pp. 431-449.

138. Wasén, J. and R. Warren, "True grain size distribution of WC-Co alloy," Materials Science and Technology, Vol. 5, 1989, pp. 222-226.

139. Björklund, H., J. Wasén and R. Warren, "Quantitative Microscopy of β-Si_3N_4 Ceramics," Journal of the American Ceramics Society, Vol. 80, No. 12, 1997, pp. 3061-3069.

140. Serii, R. and R. Tomu ed., The Stereological Methods in Materials Science, "Stereological Criteria and Measures of Grain Size Homogeneity by M. Malinski, J. Cwajna and A. Maciejny," Zaklad Narodowy im. Ossolinskich, Poland, 1988, pp. 43-56.

141. Han, J. H. and D. Y. Kim, "Determination of Three-Dimensional Grain Size Distribution by Linear Intercept Measurement," Acta Mater., Vol. 46, No. 6, 1998, pp. 2021-2028.

142. Thorvaldsen, A., "The Intercept Method – 1. Evaluation of Grain Shape," Acta Mater., Vol. 45, No. 2, 1997, pp. 587-594.

143. Thorvaldsen, A., "The Intercept Method – 2. Determination of Spatial Grain Size," Acta Mater., Vol. 45, No. 2, 1997, pp. 595-600.

144. Liu, Y., R. M. German and R. G. Iacocca, "Microstructure Quantification Procedures in Liquid-Phase Sintered Materials," Acta Mater., Vol. 47, No. 3, 1999, pp. 915-926.

145. Blank, L., "Statistical Procedures for Engineering, Management, and Science," McGraw-Hill, NY, 1980.

146. Rustagi, J. S., Introduction to Statistical Methods," Rowman and Allanheld, New Jersey, 1984.

147. Kendall, M. G. and P. A. P. Moran, “Geometrical Probability,” Hafner Publishing, NY, 1963.

148. Santalo, L. A., “Integral Geometry and Geometric Probability,” Addison-Wesley, 1976.

149. Wasén, J. and R. Warren, “A Catalogue of Stereological Characteristics of Selected Solid Bodies: Volume 1 - Polyhedrons,” Chalmers Press, Göteburg, Sweden, 1992.

150. DeHoff, R. T., "The Estimation of particle Size Distributions from Simple Counting Measurements Made on Random Plane Sections," Transactions of the AIME, Vol. 233, 1965, pp. 25-29.

151. Gundersen, H. J. G. and E. B. Jenson, “Stereological estimation of the volume-weighted mean volume of arbitrary particles observed on random sections,” Journal of Microscopy, Vol. 138, No. 2, 1985, pp. 127-142.

152. Bucki, J. J. and K. J. Kurzydlowski, “Measurements of Grain Volume Distribution Parameters in Polycrystals Characterized by a Lognormal Distribution Function,” Scripta Metallurgica et Materialia, Vol. 28, 1993, pp. 689-692.

153. McGibbon, A. J., S. J. Pennycook and D. E. Jesson, "Crystal structure retrieval by maximum entropy analysis of atomic resolution incoherent images," Journal of Microscopy, Vol. 195, Pt 1, July 1999, pp. 44–57.

154. Allen, T., “Particle Size Measurement,” 4th Edition, Chapman, NY, 1990.

155. Shannon, C. E. and W. Weaver, “The Mathematical Theory of Communication,” University of Illinois Press, Urbana, 1964.

156. Beddow, J. K. ed., Particle Characterization in Technology, Volume II, Morphological Analysis, “Optimal Definition of Class Intervals of Histograms or Frequency Plots by W. E. Full, R. Ehrlich and S. Kennedy,” CRC Press, 1984, pp. 135-145.

157. Woolfe, K. J. and K. Michibayashi, “Basic Entropy Grouping of Laser-Derived Grain Size Data: An Example for the Great Barrier Reef,” Computers & Geosciences, Vol. 21, No. 4, 1995, pp. 447-462.

158. Barba, J., H. Jeanty, P. Fenster and J. Gil, “The use of local entropy measures in edge detection for cytological image analysis,” Journal of Microscopy, Vol. 156, No. 1, 1989, pp. 125-134.

159. Bevensee, R. M., Maximum Entropy Solutions to Scientific Problems,” Prentice-Hall, 1993.

160. Hanisch, K. H. and D. Stoyan, “Stereological estimation of the radial distribution function of centres of spheres,” Journal of Microscopy, Vol. 122, No. 2, 1981, pp. 131-141.

161. Tanemura, M. “On the Stereology of Spatial Structure of Interacting Particle Systems,” Acta Stereologica, Vol. 6, No. 3, 1987, pp. 129-134.

162. Robine, H. J. P. Jernot and J. L. Chermant, “Stereological Determination of the Radial Distribution of Spheres,” Acta Stereologica, Vol. 6, No. 3, 1987, pp. 159-164.

163. Tewari, A. M. Dighe and Arun Gokhale, "Quantitative Characterization of Spatial Arrangement of Micropores in Cast Microstructures," Materials Characterization, Vol. 40, 1998, pp. 119-132.

164. Okabe, A, B. Boots, K. Sugihara and S. N. Chiu, “Spatial Tessellations: Concepts and Applications of Voronoi Diagrams,” 2nd Edition, Wiley, 2000.

165. Marthinsen, K., "Comparative Analysis of the Size Distributions of Linear, Planar, and Spatial Poisson Voronoi Cells," Materials Characterization, Vol. 36, 1996, pp. 53-63.

166. Anderson, M. P. and A. D. Rollet, ed., Simulation and Theory of Evolving Microstructures, , “The Characterization of Microstructures Using Tessellations and Their Application to Deformation Processes,” Minerals, Metals and Materials Society, 1990, pp. 199-209.

167. Lee, T. C. M., "A stochastic tessellation for modelling and simulating colour aluminium grain images," Journal of Microscopy, Vol. 193, Pt 2, 1999, pp. 109–126.

168. Kumar, S. and S. Kurtz, "Monte-carlo study of angular and edge length distributions in a three-dimensional Poisson-voronoi tessellation," Materials Characterization, Vol. 54, 1995, pp. 15-27.

169. Myles, J. P., E. C. Flenley, N. R. J. Fieller, H. V. Atkinson and H. Jones, “Statistical tests for clustering of second phases in composite materials,” Philosophical Magazine A, Vol. 72, 1995, pp. 515-528.

170. Schmidt, S., Masters Thesis, Department of Materials Science and Engineering, University of Pittsburgh, 1998.

171. Lehigh, M., Masters Thesis, Department of Materials Science and Engineering, University of Pittsburgh, 1995.

172. Krishnan, K., Masters Thesis, Department of Mechanical Engineering, University of Pittsburgh, 2000.